Quantum-critical properties of the one-dimensional long-range transverse-field Ising model extracted by quantum Monte Carlo simulations

Masters's Thesis in Physics

Presented by

Anja Langheld

30.09.2021

Institute for Theoretical Physics I
Friedrich-Alexander-Universität Erlangen-Nürnberg

Supervisors: Prof. Dr. Kai Philipp Schmidt
Dr. Sebastian C. Kapfer

Abstract

The zero-temperature criticality of the long-range transverse-field Ising model with algebraically decaying ferromagnetic and antiferromagnetic Ising coupling is investigated for the one-dimensional linear chain by simulating finite chains at finite temperature with stochastic series expansion quantum Monte Carlo integration. The convergence to effective zero-temperature properties is ensured by an empirical scheme reminiscent of simulated annealing. The critical fields h_c as well as the critical exponents β and ν are extracted using finite-size scaling methods such as the method of data collapse. For the ferromagnetic model the exponent γ is aditionally obtained by means of the same methods, rendering the set of independent critical exponents of the quantum critical point complete. While for the ferromagnetic model systems of up to $L = 1024$ spins for short-range interactions and of up to $L = 8192$ spin for long-range interactions are simulated, an increase in autocorrelation time for the antiferromagnetic model with decreasing decay exponent restricts the amount of spins to up to $L = 1024$ for short-range and up to $L = 64$ for long-range interactions. The three expected criticality regimes of the ferromagnetic model, namely the short-range criticality for large decay exponents $\alpha \geq 3$, the long-range Gaussian regime for small decay exponents $\alpha < 5/3$ with mean-field criticality, and an intermediate regime with a continuum of universality classes are confirmed consistent with former numerical findings. For the antiferromagnetic model the results suggest that the criticality remains of short-range type for all decay exponents $\alpha \geq 2$ investigated.

Inspired by a study on classical spin systems, a coherent picture of finite-size scaling above the upper critical dimension is derived for quantum systems. In this context, the characteristic length scale of a finite system is argued to violate the commonly claimed scaling with the linear system size leading to a natural reconciliation of the finite-size scaling predicted from renormalisation group with the predictions from mean-field theory. In the long-range Gaussian regime this anomalous scaling of the characteristic length scale is numerically validated utilising the same quantum Monte Carlo algorithm. The link between quantum and classical finite-size scaling above the upper critical dimension is made by additionally investigating the four-dimensional transverse-field Ising model on the hypercubic lattice which has a well-studied classical analogue.

Contents

1 Introduction and outline

As a source of novel applications, quantum systems, the phases they display and their associated critical properties became increasingly important over the last decades due to their intriguing features. Major advances have been made regarding the understanding as well as implementation of such systems, pushing forward innovative quantum technologies such as quantum simulators [1, 2]. The transverse-field Ising model (TFIM), being the paradigmatic quantum counterpart to the classical Ising model [3, 4], provides a minimal yet comprehensive model for studying zero-temperature phase transitions driven by quantum fluctuations. In its simplest version it was introduced in the 1960s in order to model interacting protons in a ferroelectric crystal exhibiting an order-disorder transition [5, 6] and was soon solved for the one-dimensional chain [7, 8]. Despite being the simplest non-trivial model, the TFIM can be easily extended to study emergent effects due to frustration [9–12], disorder [13, 14] or dynamics [15] induced by quantum quenches [16–18].

In this context, long-range interacting systems, in particular the long-range TFIM (LRTFIM), have received a lot of attention lately [12, 19–30] exhibiting remarkable collective behaviour in comparison to their short-range counterparts. For instance, the Lieb-Robinson bound restricting the propagation of correlations to an effective light cone might be violated for long-range systems [29–31] possibly giving rise to sub- or superballistic propagation of information through the system and thereby enabling unusual dynamics, e. g. in terms of relaxation times. While screening effects in condensed matter have limited the discussion to short-range systems for a long time, there are many exceptions which are inherently long-ranged, hence demanding a thorough discussion of this subject. Paradigmatic examples are the dipolar ferromagnet $LiHoF_4$ [19, 20] or spin-ice materials for which the magnetic dipolar interactions were found to fractionalise into emergent magnetic monopoles [23, 24]. Such systems can further be studied by means of quantum simulators using for example trapped ions [25–30] where the Ising interaction

$$J_{ij} \sim |\boldsymbol{r}_j - \boldsymbol{r}_i|^{-\alpha} \tag{1.1}$$

can be tuned via the decay exponent α with recent progress making it possible to simulate hundreds of qubits [25, 26]. On the theoretical side, there are limiting cases of the LRTFIM which are exactly solvable. Aside from the one-dimensional TFIM with nearest-neighbour interactions [7, 8], field-theoretical approaches can predict different criticality regimes for the unfrustrated ferromagnetic model [32] for varying decay

exponent α. For small decay exponents the ferromagnetic LRTFIM is predicted to have a continuum of universality classes differing from the short-range criticality. For even smaller decay exponents the criticality can be described by a Gaussian field theory [32] and mean-field behaviour is expected [32, 33].

Long-range interactions can therefore lower the upper critical dimension of a model to dimensions accessible in experiment. This provides access for studying scaling including finite-size scaling (FSS) above the upper critical dimension where dangerous irrelevant variables spoil the conventional scaling. While this effect of dangerous irrelevant variables on scaling has been thoroughly investigated for classical systems [34–38], it has not been addressed for quantum systems yet and within this thesis we provide an extension of a classical approach, termed Q-FSS [36–38], to quantum systems.

The intermediate regime between exactly solvable nearest-neighbour criticality and mean-field criticality is of particular interest as it yields a family of universality classes. The respective field theory is not analytically solvable and is subject to perturbative or numerical calculations. However, due to the notoriously complicated nature of these long-range systems including the potentially violated Lieb-Robinson bound, the model is numerically challenging. This bound gives rise to the so-called area law of the entanglement entropy which is crucial for the efficiency of methods based on density-matrix renormalisation group (DMRG). However, for the LRTFIM this area law was indicated to break down for antiferromagnetic long-range interactions [39–41] making other methods such as high-order series expansion [42, 43] and quantum Monte Carlo simulations [44] competitive even in one-dimensional systems where DMRG methods are often the method of choice. Within this thesis, we aim to complement existing studies of the LRTFIM and are the first to offer a full view of quantum criticality for the ferromagnetic LRTFIM in all three criticality regimes.

This thesis is structured as follows. We start by giving a brief description of quantum phase transitions in Ch. 2 while focusing on continuous phase transitions. In Ch. 3 we introduce the LRTFIM by reviewing the field-theoretical description of the ferromagnetic model and summarising the numerical results where no exact results exist. We devote Ch. 4 to the scaling at continuous phase transitions where we steer a middle course by assembling the phenomenological scaling description with some ideas from renormalisation group (RG). Within this chapter, we also extend Q-FSS to quantum systems. Thereafter we focus on the numerical study of the ferro- and antiferromagnetic LRTFIM, starting with an introduction to Monte Carlo integration in Ch. 5 and the description of stochastic series expansion in Ch. 6. In Ch. 7 we start with the results from the ferromagnetic LRTFIM with a particular focus on the intermediate regime of varying critical exponents and the mean-field regime. To further substantiate quantum Q-FSS, we decided to study the nearest-neighbour TFIM above its upper critical dimension in Ch. 8 as it provides a direct link to classical Q-FSS. Finally, the results for the antiferromagnetic LRTFIM are presented in Ch. 9 before we conclude in Ch. 10. An outlook for possible further studies is given in Ch. 11.

2 Quantum phase transitions

This section serves as an introduction to quantum phase transitions (QPT). It focuses on continuous phase transitions, also called second-order phase transitions, as the QPTs investigated in this thesis are of this type. We start by a description of what a QPT is and then continue with analyzing when such a transition takes place by following the description of Subir Sachdev in his book "Quantum Phase Transitions" [45]. Further following Ref. [45], we briefly skim over finite-temperature implications due to the existence of a quantum critical point in the phase diagram. In Sec. 2.1 we will then turn to the description of continuous phase transitions by critical exponents and stress the importance of scale invariance at the critical point in terms of universality. As there is a strong connection between classical and quantum phase transitions and some of the QPTs studied in this thesis have a well-studied classical analogue, we devoted Sec. 2.2 to elaborate upon this correspondence.

QPTs are transitions between different quantum phases at zero temperature. At the point in parameter space where such a transition occurs, the system's properties qualitatively change resulting in different phases on both sides. This change in behaviour is usually associated with spontaneous symmetry-breaking and quantified by an order parameter. The phase with higher symmetry is the disordered phase in which the order parameter vanishes. In the ordered phase, the symmetry of the Hamiltonian is spontaneously broken leading to a state with lower symmetry and a non-zero order parameter. For instance, the ferromagnetic transverse-field Ising model has an underlying $\mathbb{Z}_2$ symmetry under which the paramagnetic state with vanishing magnetisation is invariant whilst in the ferromagnetic phase the system spontaneously chooses a magnetisation direction such that the state is no longer invariant under this symmetry [46].

While classical continuous phase transitions are triggered by strong thermal fluctuations which lead to a non-analyticity of the free energy, at zero temperature there are no thermal fluctuations and equilibrated systems are in their ground state. At a quantum phase transition, this ground-state energy is non-analytic with respect to a non-thermal control parameter like pressure or an external field. For a better understanding of this non-analyticity, consider a Hamiltonian $\mathcal{H}(g) = \mathcal{H}_0 + g\mathcal{H}_1$ as a function of a dimensionless coupling g which will serve as our control parameter [45]. For a finite system the ground-state energy is usually analytic with the main exception for the case when $[\mathcal{H}_0, \mathcal{H}_1] = 0$ in which case one can diagonalise $\mathcal{H}_0$ and $\mathcal{H}_1$ simultaneously and

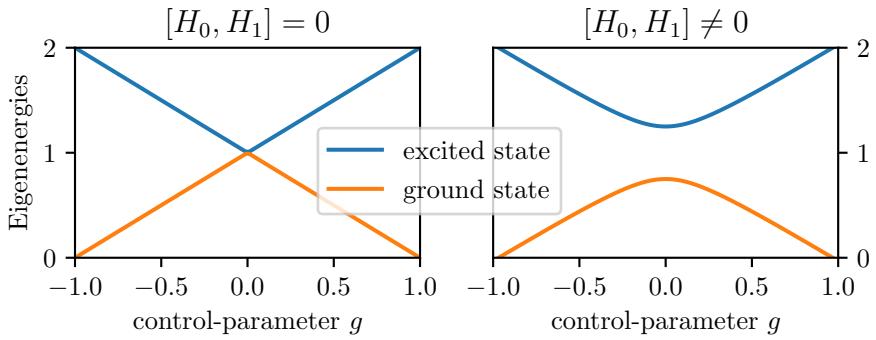

Figure 2.1: *Left: Level crossing in a two-level system due to commuting $\mathcal{H}_0$ and $\mathcal{H}_1$. Right: Avoided level crossing due to the introduction of the operator $\frac{1}{4}\sigma^x$ into $\mathcal{H}_0$ with $[\sigma^x, \mathcal{H}_1] \neq 0$.*

find a common eigenbasis. Hence, the eigenvectors are independent of the parameter g [45]. As an example, consider a simple two-level system $\mathcal{H} = \mathbb{1} + g\sigma^z$ with the Pauli matrix σ^z. When expressed in the σ^z-eigenbasis, this leads to the matrix representation

$$\mathcal{H} = \begin{pmatrix} 1+g & 0 \\ 0 & 1-g \end{pmatrix} \tag{2.1}$$

and there is a level-crossing at $g = 0$ with an abrupt change in the ground state of the system as depicted in the left part of Fig. 2.1. However, if we add $a\sigma^x$ to $\mathcal{H}_0$ with $a \neq 0$

$$\mathcal{H} = \begin{pmatrix} 1+g & a \\ a & 1-g \end{pmatrix}, \tag{2.2}$$

$\mathcal{H}_0$ and $\mathcal{H}_1$ will no longer commute and there is an avoided level crossing (see Fig. 2.1 right). Such an avoided level crossing can become progressively sharper the bigger the system gets and the finite energy gap between the ground state and excited state might close for an infinite system leading to a non-analyticity. This limit of an avoided level crossing is the case we are mainly interested in as a level-crossing in finite systems corresponds to a first-order phase transition [47]. A main difference between first-order and continuous phase transition is that the former yields phase coexistence at the transition point while in the latter case the system exhibits correlations on large scales and the distinct phases become identical at the point of the phase transtion leading to a single critical phase covering the whole system. In the following we will concentrate on continuous phase transitions. The point in parameter space where such a continuous phase transition occurs is called critical point.

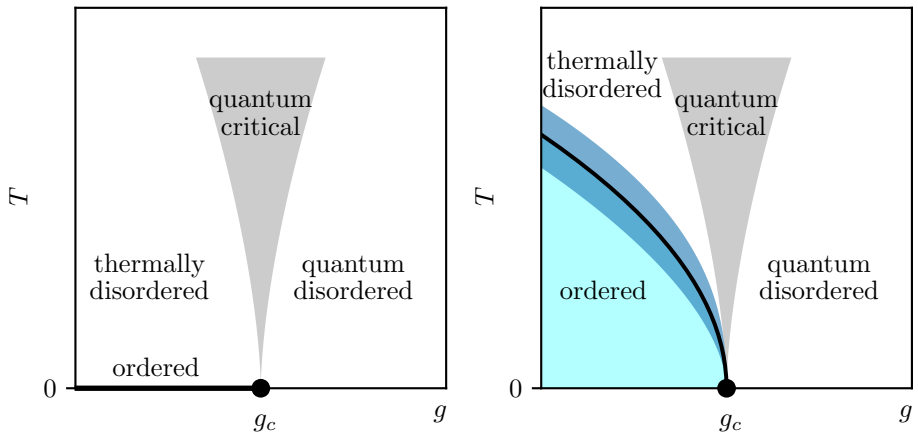

Figure 2.2: *Possible phase diagrams close to a quantum critical point with a non-thermal control parameter g triggering the quantum phase transition. The grey-shaded area is the quantum critical regime where quantum as well as thermal fluctuations are important. Left: No long-range order at finite temperature. Right: A line of thermal phase transitions at $T > 0$ is shown with a blue shaded area indicating a regime where thermal fluctuations dominate the macroscopic scales and a theory of classical phase transitions is applicable.*

Even though quantum phase transitions can only occur at zero temperature, which is a region not accessible in experiment, understanding this point of singularity is not out of pure academic interest as a quantum critical point also affects a system's behaviour at non-zero temperature [45]. In Fig. 2.2, two possible phase diagrams are depicted with their main difference being a line of classical phase transitions entering the quantum critical point g_c at $T = 0$ in the phase diagram on the right hand side. In both cases there is one thermally disordered regime and one quantum disordered regime where the order is destroyed mainly due to thermal or quantum fluctuations respectively. In between lies the quantum critical region (grey shaded area in Fig. 2.2), where both types of fluctuations determine the physics [45, 47]. The quantum critical region extends to relatively high temperatures [47] while displaying unusual finite-temperature properties [47]. At non-zero temperature, quantum as well as thermal fluctuations are relevant and a central task of the theory of quantum phase transitions is the description of physical properties at non-zero temperature emerging from the quantum critical point [45].

2.1 Critical exponents

We will now turn to the description of QPTs by critical exponents, which characterise the behaviour of observables in the vicinity of a critical point. For convenience, we define the reduced control parameter $r = \frac{g-g_c}{g_c}$ as the deviation from the critical point $g = g_c$, where the ground-state energy becomes non-analytic and a phase transition occurs. We further assume, without loss of generality, that for $r < 0$ the system is in the ordered phase with finite order parameter while for $r > 0$ it is in the symmetric phase.

Close to a critical point, systems exhibit a characteristic length scale ξ diverging as

$$\xi \sim |r|^{-\nu}\,, \tag{2.3}$$

defining the critical exponent ν. This characteristic length scale could be a correlation length governing an exponential decay at long distances or the length at which a characteristic crossover to the long-distance behaviour of the correlations occurs [45]. There is also a characteristic energy scale Δ[1] which vanishes as one approaches a quantum critical point [45]

$$\Delta \sim |r|^{z\nu}\,, \tag{2.4}$$

additionally introducing the critical exponent z. This characteristic energy scale gives rise to a characteristic time scale $\xi_\tau \sim \Delta^{-1}$ with which the correlations decay in time. It hence diverges as

$$\xi_\tau \sim |r|^{-z\nu} \tag{2.5}$$

such that $\xi_\tau \sim \xi^z$ and therefore the critical exponent z characterises the anisotropy of correlations in space-time. Other physical quantities such as the order parameter or response functions also exhibit singular behaviour in terms of power laws near the critical point. Those singularities define further critical exponents $(\alpha, \beta, \gamma, \delta, \eta)$ which are listed in Tab. 2.1 for the example of a ferromagnetic system. One may also define critical exponents characterising the divergence coming from finite temperature $T \to 0$ at $r = 0$ [48].

2.1.1 Universality

Albeit distinct physical systems can behave very differently on microscopic scales, they might exhibit the same criticality, meaning their critical exponents coincide,[2] as detailed fluctuations on the microscopic scale become unimportant in comparison to the

[1] An energy gap between the lowest excitation and the ground state would be such a characteristic energy scale, while for gapless spectra the definition is less obvious [45].

[2] In fact not only the critical exponents are universal, but also exponents describing corrections to scaling as well as so-called scaling functions [49].

Table 2.1: *Definitions of critical exponents by means of the singularities of thermodynamic quantities for a magnetic phase transition. The free energy density is denoted by f. Note that the control parameter susceptibility associated with the critical exponent α coincides with the heat capacity only for thermal phase transitions, where $r = \frac{T-T_c}{T_c}$, while for quantum phase transitions the meaning depends on the control parameter triggering the phase transition [48].*

Observable	Definition	Crit. Exp.	Singularity
Characteristic length ξ	via $G(\boldsymbol{r})$	ν	$\xi(r \to 0, H = 0) \sim \lvert r\rvert^{-\nu}$
Energy gap Δ	via $G(\boldsymbol{r}, \omega)$	$z\nu$	$\Delta(r \to 0) \sim \lvert r\rvert^{z\nu}$
Charact. time scale ξ_τ	$\xi_\tau \sim \Delta^{-1}$		$\xi_\tau(r \to 0) \sim \xi^z \sim \lvert r\rvert^{-z\nu}$
Order parameter m	$m = \frac{\partial f}{\partial H}$	β	$m(r \to 0^-, H = 0) \sim \lvert r\rvert^{\beta}$
		δ	$m(r = 0, H \to 0) \sim H^{1/\delta}$
Order-parameter susceptibility χ	$\chi = \frac{\partial m}{\partial H}$	γ	$\chi(r \to 0, H = 0) \sim \lvert r\rvert^{-\gamma}$
Control-parameter susceptibility χ_r	$\chi_r = \frac{\partial^2 f}{\partial r^2}$	α	$\chi_r(r \to 0, H = 0) \sim \lvert r\rvert^{-\alpha}$
Correlation function $G(\boldsymbol{r})$	$\frac{\partial \langle m(\boldsymbol{r})\rangle}{\partial H_{\boldsymbol{r}=0}}\Big\rvert_{H_0=0}$	η	$G(\boldsymbol{r} \to \infty, r = 0, H = 0) \sim \frac{1}{\lvert \boldsymbol{r}\rvert^{d-2+\eta}}$

large-distance fluctuations close to a critical point. When two systems experience the same critical behaviour, they are said to lie in the same universality class. Systems in one universality class share common global properties such as dimensionality, symmetry or the range of interactions.

The origin of this outstanding phenomenon of universality was elucidated by the notion of the renormalisation (semi-)group formalism mainly going back to Wilson in the 1970s [50, 51]. As a system approaches a critical point, the characteristic length scale ξ diverges, rendering the system scale-free [49]. This lack of scale is incorporated in the renormalisation group (RG) formalism. Loosely speaking, an RG transformation is a spatial rescaling of a system which decimates short-distance (or high-energy) degrees of freedom. It therefore singles out the long-distance and low-energy behaviour of the system, which are the relevant scales at a continuous phase transition [47]. A Hamiltonian $\mathcal{H}[s]$ with the degrees of freedom s is mapped to a Hamiltonian $\mathcal{H}'[s']$ via the renormalisation transformation $\mathcal{R}$ [49]

$$\mathcal{H}'[s'] = \mathcal{R}_b\{\mathcal{H}[s]\} \tag{2.6}$$

whereby s' denotes the renormalised degrees of freedom and b is the rescaling factor. The Hamiltonian $\mathcal{H}$ is modified to $\mathcal{H}'$ such that the partition function is left invariant and the physics is preserved under the whole transformation [47]. Note that $\mathcal{H}'$

by no means has to have the same form as $\mathcal{H}$ [49]. The Hamiltonian is successively renormalised by $\mathcal{R}$ to extract the long-distance behaviour of the system. This procedure can be visualised as a flow through a larger space of Hamiltonians [49]. Often this flow asymptotically converges to a Hamiltonian $\mathcal{H}^*$ which is a fixed point of the renormalisation transformation [49], meaning

$$\mathcal{R}_b\{\mathcal{H}^*\} = \mathcal{H}^* \,. \tag{2.7}$$

Not all fixed points are particularly interesting. Trivial fixed points describe stable phases, e. g. a fully aligned or fully disordered state of the transverse-field Ising model with both states being invariant under a spatial scaling transformation. However, there can be non-trivial fixed points which are associated with critical points and are the points of interest. In the context of RG, a universality class is a set of models flowing to the same non-trivial fixed point $\mathcal{H}^*$ under the action of renormalisation [49].

2.1.2 Scaling relations

The critical exponents introduced are not independent from each other, but related by a number of scaling relations [48], namely

$$2 - \alpha = (d + z)\nu \,, \tag{2.8}$$
$$2 - \alpha = 2\beta + \gamma \,, \tag{2.9}$$
$$\gamma = \beta(\delta - 1) \,, \tag{2.10}$$
$$\gamma = (2 - \eta)\nu \,. \tag{2.11}$$

The first relation Eq. (2.8) is the so-called hyperscaling relation whose classical analogon (without z) was developed by Widom [49, 52, 53]. It is the only one containing the dimension of the system and therefore breaks down above the upper critical dimension where one expects the same mean-field critical exponents independent of the dimension d [49]. The Essam-Fisher relation Eq. (2.9) [54,55] is reminiscent of a similar inequality proven rigorously by Rushbrooke by thermodynamic stability arguments. Eq. (2.10) is called Widom relation. The last relation Eq. (2.11) is the Fisher scaling relation which can be derived using the fluctuation-dissipation theorem [48, 49, 55]. Those relations were originally obtained from scaling assumptions of observables close to the critical point which were only later derived rigorously when the RG formalism was introduced to critical phenomena and shed light on the scaling behaviour of observables [48, 49].

2.2 Quantum-classical mapping

There is a strong correspondence between classical and zero-temperature quantum models, which we will take advantage of in the field-theoretical description of the quantum criticality in Sec. 3.2. A d-dimensional quantum-mechanical system can, at least formally, be mapped onto $(d+1)$-dimensional classical system. This is done by rewriting the partition function of the quantum system

$$Z = \mathrm{tr}\left(e^{-\beta\mathcal{H}}\right) \tag{2.12}$$

using Euclidean path integrals.[1] In this process, $\exp(-\beta\mathcal{H})$ represents an evolution in imaginary time over a time $L_\tau = \hbar\beta$ which constitutes the additional dimension in the $(d+1)$-dimensional classical model [45]. Hence, the temperature of the quantum model maps to an additional continuous, finite dimension in the classical model. The imaginary-time dimension is a circle S^1 with circumference L_τ as the trace in Eq. (2.12) induces periodic boundary conditions. For a zero-temperature quantum model this additional classical dimension becomes infinite.

Even though this formalism is quite powerful as it is very general, some remarks have to be made:

- This formal mapping is only quantitatively precise for continuous imaginary time and $\beta \to \infty$ [45]. It is therefore only exact in the vicinity of a continuous quantum phase transition where the microscopic details become irrelevant and the temperature vanishes. Its utility mainly lies in field-theoretical descriptions close to quantum critical points where the continuum limit is taken. One could rather say that it maps the quantum field theory of a quantum critical point onto an analogue classical field theory for a continuous phase transition at finite temperature.
- The temperature of the classical model is not related to the temperature of the quantum model [45]. The temperature of the quantum model will map onto the system's length in imaginary time while the control parameter tuning the quantum fluctuations will determine the temperature of the classical model [45].
- The classical problem might be rather artificial and the additional imaginary-time dimension by no means has to behave similar to the spatial dimensions leading to an anisotropic system ($z \neq 1$) [45]. When we later study the ferromagnetic transverse-field Ising model with long-range interactions, we will encounter such a spacetime anisotropy.
- The resulting "Boltzmann"-weights of the classical problem might very well be negative or even complex valued [45].

[1] This method is not only used in field-theoretical descriptions of critical points but is also the basis for path integral quantum Monte Carlo simulations.

- From the imaginary-time dimension one can extract correlation functions in imaginary time which in principle contain information about the real-time dynamics [45]. Exact results in imaginary time can be translated to real time by a Wick rotation. However, it is an ill-posed problem as any kind of approximation before performing the Wick rotation will lead to unreliable results [45].

The following chapter is devoted to the long-range transverse-field Ising model (LRTFIM) as it is the model studied in this thesis. For the short-range limit of this model there exists a mapping to a well-studied classical analogue; namely, the short-range transverse-field Ising model in d dimensions exhibits the same criticality as the classical Ising model in $(d+1)$ dimensions. Initially, this correspondence was found numerically by means of a series expansion [56]. Later, Suzuki [57] analytically confirmed that the criticality of a d-dimensional quantum spin model at $T = 0$ coincides with the criticality of a $(d + 1)$-dimensional classical model at finite temperature. The ferromagnetic LRTFIM can also be mapped to a classical system. However, the long-range interaction will induce a spacetime anisotropy leading to an anisotropic classical analogue.

3 The long-range transverse-field Ising model

This chapter describes the model investigated in this thesis, which is the long-range transverse-field Ising model (LRTFIM). The focus will lie on the short-range limit on the hypercubic lattice in arbitrary dimensions as well as on the one-dimensional linear chain with long-range interactions. We start by writing down the Hamiltonian

$$\mathcal{H} = \sum_{i,j} J_{ij}\sigma_i^z\sigma_j^z - h\sum_i \sigma_i^x \tag{3.1}$$

with the Pauli matrices $\sigma_i^{x,z}$ describing spins 1/2 located on lattice sites $\boldsymbol{r}_i$. The Ising bonds

$$J_{ij} = \frac{J}{2}\frac{1}{|\boldsymbol{r}_j - \boldsymbol{r}_i|^\alpha} \tag{3.2}$$

couple pairs of spins along the z-axis while the transverse field with strength h is oriented along the x-axis. For $J > 0$ the Ising coupling is antiferromagnetic and for $J < 0$ the spins are coupled ferromagnetically. The Ising coupling is further tuned by the decay exponent α. The model reduces to the nearest-neighbour model for $\alpha \to \infty$, while in the limit $\alpha = 0$, all spins are coupled equally. As $[\sigma_i^z, \sigma_i^x] = i\sigma_i^y$, the Ising interaction does not commute with the transverse-field term resulting in quantum fluctuations which in some cases, e. g. on hypercubic lattices or for the ferromagnetic model, can trigger a phase transition between an ordered state for small h/J and a disordered state for large h/J. Without loss of generality, we keep $|J| = 1$ and only vary h. The critical field, where the phase transition occurs, is denoted by h_c. In the nearest-neighbour limit, the d-dimensional transverse-field Ising model maps onto the $(d+1)$-dimensional classical Ising model via the quantum-classical mapping [56, 57] (see Sec. 2.2).

3.1 Limiting cases for low and high transverse fields

In this section we will consider the two limiting cases $h \gg J$ and $h \ll J$. We denote the eigenvectors of σ_i^z with $|\uparrow\rangle_i$, $|\downarrow\rangle_i$ with eigenvalues $+1$, -1 respectively. At $h = 0$ the Hamiltonian is diagonal in the basis of the σ_i^z eigenstates and therefore reduces to

the classical Ising model [45]. However, for a finite transverse field, the operators σ_i^x induce transitions between the two eigenstates of σ_i^z.

High-field limit: The limit of a large field h is easier than the limit for small h as it does not depend on the sign or geometry of the Ising coupling. For $h/J \to \infty$ the ground state is given by an x-polarised state [45]

$$|0\rangle = \prod_i |{\rightarrow}\rangle_i \tag{3.3}$$

with $\sigma_i^x |{\rightarrow}\rangle_i = +1 |{\rightarrow}\rangle_i$. In this state the magnetisation in z-direction is uncorrelated and $\langle 0| \sigma_i^z \sigma_j^z |0\rangle = \delta_{ij}$ [45]. The lowest excitations are single spin flips

$$|i\rangle = |{\leftarrow}\rangle_i \prod_{j \neq i} |{\rightarrow}\rangle_j \tag{3.4}$$

corresponding to a single quasi-particle sitting at site i [45]. In general, one can define N-particle states

$$|i_1, \ldots, i_N\rangle = \prod_{i \in \{i_1,\ldots,i_N\}} |{\leftarrow}\rangle_i \prod_{j \notin \{i_1,\ldots,i_N\}} |{\rightarrow}\rangle_j \tag{3.5}$$

with quasi-particles at sites $i_1, \ldots, i_N$. The Ising coupling $J_{ij}\sigma_i^z\sigma_j^z$ induces pairwise spin flips at sites i and j. It therefore either generates or destroys a pair of quasi-particles or induces a hopping of one quasi-particle at site i to j (or j to i). For finite but large h this will introduce correlations in σ^z leading to non-zero $\langle 0| \sigma_i^z \sigma_j^z |0\rangle$. However, in the limit of large distances

$$\lim_{|\boldsymbol{r}_j - \boldsymbol{r}_i| \to \infty} \langle 0| \sigma_i^z \sigma_j^z |0\rangle = 0 \tag{3.6}$$

the correlations still vanish [45]. The system is in a paramagnetic state.

Low-field limit: The low-field limit differs for ferromagnetic and antiferromagnetic Ising coupling and we will only consider ferromagnetic coupling here as the antiferromagnetic case is more difficult for non-bipartite lattices. For a ferromagnetic coupling the ground state at $h = 0$ is two-fold degenerate

$$|{\Uparrow}\rangle = \prod_i |{\uparrow}\rangle_i \qquad |{\Downarrow}\rangle = \prod_i |{\downarrow}\rangle_i \tag{3.7}$$

with all spins aligned either upwards or downwards. This degeneracy remains in the whole ordered phase for an infinite lattice as it is protected by the broken $\mathbb{Z}_2$ symmetry. In contrast, the degeneracy on a finite lattice is lifted for any $h > 0$. A small but finite

h will add some spins of the opposite orientation to the ground state of the system, but the spins are correlated in a qualitatively different manner

$$\lim_{|\boldsymbol{r}_j - \boldsymbol{r}_i| \to \infty} \langle 0 | \, \sigma_i^z \sigma_j^z \, | 0 \rangle = m_0^2 \tag{3.8}$$

in comparison to the large-h limit in Eq. (3.6). There is a non-zero spontaneous magnetisation m_0 of the ground state [45]

$$\langle 0 | \, \sigma_i^z \, | 0 \rangle = \pm m_0 \tag{3.9}$$

breaking the $\mathbb{Z}_2$ symmetry of the model. The system is in a ferromagnetically ordered state.

Connecting those limits: The two limits behave qualitatively different and it is impossible for those states with Eq. (3.6) and Eq. (3.8) to transform into each other in an analytic fashion [45]. There has to be at least one point $h = h_\mathrm{c}$ of non-analyticity at which a quantum phase transition occurs. The description of this critical point will be the focus of the next subsections and the numerical study of its criticality for the one-dimensional chain is a main result of this thesis.

3.2 Field-theoretical description with ϕ^4-theory

We will briefly discuss a field-theoretical description of the ferromagnetic quantum phase transitions studied in this thesis. Even though we only consider ferromagnetic couplings $J < 0$, the discussion of the short-range case nevertheless includes the antiferromagnetic model on bipartite lattices as it is equivalent to its ferromagnetic counterpart by the virtue of a sublattice rotation.

The utility of a field-theoretical description of a phase transition is based on universality and the premise that the structure on the lattice scale becomes unimportant in the vicinity of the critical point [45]. The respective field theory disregards those microscopic structures of a model and only incorporates the essential attributes that models of one universality class have in common, such as dimension and symmetry. The continuum theory is derived by coarse-graining the microscopic degrees of freedom. In the case of the Ising model the coarse-grained field is defined as [45]

$$\phi(\boldsymbol{x}, \tau) \sim \sum_{i \in \mathcal{N}(\boldsymbol{x})} \sigma_i^z(\tau) \tag{3.10}$$

where $\mathcal{N}(\boldsymbol{x})$ denotes the vicinity of $\boldsymbol{x}$ and τ is the coordinate in imaginary time.

The section starts with the field theory of the transverse-field Ising model with nearest-neighbour interaction in arbitrary dimensions and, for the antiferromagnetic model, on

bipartite lattices in order to motivate the study of its four-dimensional member on the hypercubic lattice. It will introduce a very basic formalism of scaling transformations that will grant us with the Gaussian scaling behaviour in the mean-field regime. In Sec. 3.2.2 we will supplement the short-range field theory with the long-range interactions of the LRTFIM and derive mean-field critical exponents in the long-range limit.

3.2.1 The short-range Ising ϕ^4-theory

The Hamiltonian for the nearest-neighbour transverse-field Ising model is given by

$$\mathcal{H} = J \sum_{\langle i,j \rangle} \sigma_i^z \sigma_j^z - h \sum_i \sigma_i^x \tag{3.11}$$

where the sum is now restricted to pairs $\langle i, j \rangle$ of nearest-neighbour sites. The partition function of the field theory is given as an Euclidean path integral which sums over all possible field values $\phi(\boldsymbol{x}, \tau)$ [45]

$$Z = \int \mathcal{D}\phi(\boldsymbol{x}, \tau) \exp(-S_{\mathrm{SR}}) \,, \tag{3.12}$$

$$S_{\mathrm{SR}} = \int \mathrm{d}^d \boldsymbol{x} \int_0^\beta \mathrm{d}\tau \left\{ \left[\tilde{g} (\partial_\tau \phi)^2 + b \left(\nabla \phi \right)^2 + r_0 \phi^2 \right] + u_0 \phi^4 \right\} \,, \tag{3.13}$$

where the field $\phi(\boldsymbol{x}, \tau)$ has to obey the periodic boundary condition $\phi(\boldsymbol{x}, \tau) = \phi(\boldsymbol{x}, \tau + \beta)$ in imaginary time coming from the trace in the partition function. The terms $\sim \phi^2$ and $\sim \phi^4$ come from the expansion of an effective potential $V(\phi^2)$ that prevents the field from becoming too large as its microscopic constituents σ_i^z are bounded [45]. It only considers even powers of ϕ incorporating the $\mathbb{Z}_2$ symmetry of the microscopic model[1] and disregards higher orders than ϕ^4 in a Taylor expansion as it will turn out to be sufficient [45]. Further, $r_0 = m_0^2$ denotes the bare mass term of the field and $u_0 \phi^4$ leads to self-interaction of the field. If one neglects the self interaction, the field theory is a Gaussian theory describing a free field. The spacetime derivatives arise from the energy cost of spatial variations in the magnetic order and the imaginary-time variations due to spin flips induced by $h\sigma_i^x$ [45].

From Eq. (3.13) one observes that the imaginary-time direction τ is equivalent to the spatial directions for $\beta \to \infty$ and the action then becomes equivalent to the corresponding action of the $(d+1)$-dimensional classical Ising model. One therefore expects the d-dimensional TFIM to exhibit the same criticality, i. e. the same critical exponents, as the $(d+1)$-dimensional classical Ising model. For example, the one-dimensional TFIM obeys the predictions from Onsager for the two-dimensional classical model [58].

[1] The $\mathbb{Z}_2$ symmetry is also the reason why the field ϕ is a real scalar field.

At the critical point the action has to be invariant under a spacetime rescaling

$$\boldsymbol{x} \to \boldsymbol{x}' = \frac{\boldsymbol{x}}{b} \qquad \text{and} \qquad \tau \to \tau' = \frac{\tau}{b^z} \tag{3.14}$$

by a rescaling factor b. Consequently, the coupling constants in the action as well as the field itself have to be rescaled as well. One commonly denotes the power of the rescaling factor b of a variable a as its scaling power $[a]$ with $a \to a' = b^{[a]}a$, e.g. $[\boldsymbol{x}] = -1$ and $[\tau] = -z$. By counting the scaling powers of the different terms in the action and demanding them to cancel, one obtains a set of linear equations

$$-d - z + [\tilde{g}] + 2z + 2\,[\phi] = 0\,, \tag{3.15}$$
$$-d - z + [b] + 2 + 2\,[\phi] = 0\,, \tag{3.16}$$
$$-d - z + [r_0] + 2\,[\phi] = 0\,, \tag{3.17}$$
$$-d - z + [u_0] + 4\,[\phi] = 0\,, \tag{3.18}$$

where it was used that $\left[\mathrm{d}^d\boldsymbol{x}\right] = -d$, $[\mathrm{d}\tau] = -z$, $[\nabla] = 1$ and $[\partial_\tau] = z$. At mean-field level, one demands $[\tilde{g}] = [b] = 0$ [1] [33,59] and one can solve for the remaining exponents z, $[\phi]$, $[r_0]$ and $[u_0]$ which yields

$$z = 1\,, \tag{3.19}$$
$$[\phi] = \frac{1}{2}\,(d-1)\,, \tag{3.20}$$
$$[r_0] = 2\,, \tag{3.21}$$
$$[u_0] = 3 - d\,. \tag{3.22}$$

Under successive scaling transformations, the coupling constants are modified according to their scaling powers Eq. (3.21) and Eq. (3.22) and approach fixed points at which another transformation would yield the same value $a \to a' = a$. Considering the rescaling of $r_0 \to r_0' = b^2 r_0$, there are three fixed points, namely the trivial fixed points at $r_0 = \pm\infty$ as well as the non-trivial fixed point $r_0^* = 0$ [45]. As a small perturbation in r_0 around r_0^* will drive r_0 to $\pm\infty$ and away from r_0^*, the fixed point is unstable and the variable r_0 is called *relevant* [45,49]. For the coupling constant u_0 one always finds the fixed point $u_0^* = 0$ and the pair $(r_0^*, u_0^*) = (0,0)$ is termed Gaussian fixed point. This Gaussian fixed point is stable for $d > 3$ and unstable for $d < 3$ and u_0 is called *irrelevant* or *relevant* respectively [45,49]. In case of u_0 being *irrelevant*, the Gaussian fixed point is the only physical fixed point of this field theory and describes the physics of the critical point [45,60]. However, for $d < 3$ another fixed point (r_0^*, u_0^*), called the Wilson-Fisher fixed point, with $r_0^* \neq 0$ and $u_0^* \neq 0$ arises to which the Hamiltonian at the critical point will flow under successive renormalisation [45]. Therefore, the

[1] This effectively neglects fluctuations due to the self interaction and enforces $\eta = 0$.

Wilson-Fisher fixed point is the relevant fixed point for $d < 3$. This fixed point is subject to a proper RG calculation and can not be derived from the naive scaling transformation we considered [45]. The dimension at which the scaling dimension of u_0 vanishes and the character of the phase transition changes is called the upper critical dimension d_{uc}. For the short-range theory, $d_{\mathrm{uc}} = 3$. Above d_{uc} the critical exponents attain their mean-field values. In contrast, if the scaling dimension of the field ϕ becomes negative, no phase transition occurs. This leads to the definition of a lower critical dimension d_{lc} below which there is no phase transition. From Eq. (3.20) one readily identifies $d_{\mathrm{lc}} = 1$.

As *irrelevant* variables flow to zero, one might feel the urge to neglect them from the very beginning. That was the reason why we only considered terms up to order ϕ^4 in the Taylor expansion of $V(\phi^2)$ as the associated couplings of higher orders are *irrelevant* [49]. However, in case of the coupling u_0, it will turn out that neglecting this coupling for $d > 3$, when u_0 becomes *irrelevant*, and only considering the Gaussian theory leads to inconsistencies in the predictions of critical exponents [53]. The reason is that the free energy is singular in the limit $u_0 \to 0$, terming u_0 a *dangerous irrelevant variable*. This problem will be addressed in detail in Sec. 4.1.3 and is the motive for studying the four-dimensional TFIM as the lowest-dimensional TFIM with $d > 3$.

This rescaling procedure performed here was merely a dimensional analysis and only yields the scaling corresponding to the Gaussian field-theory valid in the mean-field regime. In proper RG transformations one performs infinitesimal scaling transformations by integrating out short-distance degrees of freedom and describes the flow of the couplings by differential equations [45]. These differential equations are in general coupled. They are then linearised and decoupled leading to the definition of new eigencouplings, one *irrelevant* coupling u and one *relevant* coupling r, in terms of the distance of the bare couplings $\delta u_0 = u_0 - u_0^*$ and $\delta r_0 = r_0 - r_0^*$ to the physical fixed point (r_0^*, u_0^*). The *relevant* eigencoupling r is identified with the deviation from the critical point in terms of the tuning parameter $\frac{g-g_c}{g_c}$ [45]. For the Gaussian fixed point the eigencouplings r and u coincide with the bare couplings r_0 and u_0 up to corrections[1] that are not relevant to us (see [60], Chap. 7 for details) and the scaling powers coincide, i. e. $[r] = [r_0]$ and $[u] = [u_0]$. For further insights on RG in field theory we refer to Sachdev's book on quantum phase transitions [45] or the review by Shankar [62] and recommend a review by Fisher [49] for a more general (beyond field theory) and picturesque view on RG.

The reason we took the time to discuss this very basic form of scaling transformation is that the critical exponents are related to the scaling dimensions of the eigencouplings. As the *relevant* eigencoupling corresponds to $r \sim \frac{g-g_c}{g_c} \sim \xi^{-1/\nu}$ [45] and lengths have

[1] Those corrections lead to a shift of the pseudo-critical temperature in finite systems with respect to the bulk critical temperature [61].

the scaling dimension $[\boldsymbol{x}] = -1$, the scaling dimension $[r]$ relates to the critical exponent ν by [45]

$$\nu = \frac{1}{[r]}\,. \tag{3.23}$$

Further critical exponents will be related in the discussion on scaling in Sec. 4.1.2. For that, we will also need the scaling dimension of the conjugate field H that couples to the order parameter via an additional term $H\sum_i \sigma_i^z$ in the original Hamiltonian $\mathcal{H}$. Its scaling dimension will turn out to be connected to the critical exponents β, γ, δ and η. In the field theory this adds a corresponding additional term

$$\int \mathrm{d}^d\boldsymbol{x} \int_0^\beta \mathrm{d}\tau\, H\phi(\boldsymbol{x},\tau) \tag{3.24}$$

to the short-range action S_{SR}. Under the previous scaling transformation this yields an additional relation

$$-d - z + [H] + [\phi] = 0 \tag{3.25}$$

which fixes the scaling dimension of H to

$$[H] = \frac{1}{2}(d+3)\,. \tag{3.26}$$

3.2.2 The long-range Ising ϕ^4-theory

In contrast to the previous subsection, this field theory only applies to the ferromagnetic case as the Ising couplings no longer correspond to a bipartite graph. Adding long-range couplings among the spins in the microscopic Hamiltonian results in a long-range coupling of the field $\phi(\boldsymbol{x},\tau)$ in the continuum limit [33]. The only *relevant* long-range term for $\alpha > d$ which at the same time is odd with respect to $\phi(\boldsymbol{x},\tau) \to -\phi(\boldsymbol{x},\tau)$ is given by [33]

$$S_{\mathrm{LR}} = b_\sigma \int \mathrm{d}^d\boldsymbol{x} \int_0^\beta \mathrm{d}\tau \int \mathrm{d}^d\boldsymbol{y}\, \frac{\phi(x,\tau)\phi(y,\tau)}{|\boldsymbol{x}-\boldsymbol{y}|^\alpha} \tag{3.27}$$

and we augment the short-range action S_{SR} in Eq. (3.13) with the long-range term to $S = S_{\mathrm{SR}} + S_{\mathrm{LR}}$. For the following discussion, it is beneficial to cast the quadratic part of the action into its Fourier representation [32, 33, 59]

$$S = \int \mathrm{d}^d\boldsymbol{q} \int \mathrm{d}\omega \left(\tilde{g}\omega^2 + r_0 + bq^2 + b_\sigma q^\sigma\right) \left|\tilde{\phi}(\boldsymbol{q},\omega)\right|^2 + u_0 \int \mathrm{d}^d\boldsymbol{x} \int_0^\beta \mathrm{d}\tau\, \phi^4(\boldsymbol{x},\tau) \tag{3.28}$$

and at the same time introduce $\sigma = \alpha - d$ for characterising the algebraic decay of the long-range interaction. We are interested in the long-wavelength behaviour[1] of

[1] Long wavelengths correspond to the large-distance behaviour which is the important scale at continuous phase transitions.

the theory which corresponds to small q. In the Fourier representation one readily identifies two different regimes in terms of the decay exponent σ. For $\sigma \geq 2$ the leading term for long wavelengths is given by q^2 coming from the spatial derivative of the short-range model. One therefore expects the critical behaviour to reduce to the criticality of the short-range model for $\sigma \geq 2$ [32, 33]. On the other hand, for $\sigma < 2$, the dominant contribution comes from the long-range interaction which led to the term $\sim q^\sigma$ in the action and alters the critical behaviour. Following the same line of arguments as before and performing the naive scaling transformation on mean-field level for the action in real space, yields[1]

$$-d - z + 2z + 2\,[\phi] = 0\,, \tag{3.29}$$
$$-2d - z + d + \sigma + 2\,[\phi] = 0\,, \tag{3.30}$$
$$-d - z + [r] + 2\,[\phi] = 0\,, \tag{3.31}$$
$$-d - z + [u] + 4\,[\phi] = 0\,, \tag{3.32}$$
$$-d - z + [H] + [\phi] = 0\,. \tag{3.33}$$

Only the second equation - corresponding to the long-range interaction - differs from the equations for the short-range model and we already included the scaling transformation for an additional conjugate-field term. This yields the scaling dimensions

$$[\phi] = \frac{1}{2}\,(d - z) = \frac{1}{2}\left(d - \frac{\sigma}{2}\right) \tag{3.34}$$
$$[r] = \sigma \tag{3.35}$$
$$[u] = d + z - 2(d - z) = -d + \frac{3\sigma}{2} \tag{3.36}$$
$$[H] = \frac{1}{2}\,(d + 3z) = \frac{1}{2}\left(d + \frac{3\sigma}{2}\right) \tag{3.37}$$

alongside the mean-field critical exponents

$$z = \frac{\sigma}{2} \qquad \text{and} \qquad \nu = \frac{1}{[r]} = \frac{1}{\sigma}\,. \tag{3.38}$$

From Eq. (3.36) one identifies the upper critical dimension, where $[u]$ vanishes, as

$$d_{\mathrm{uc}} = \frac{3\sigma}{2} \tag{3.39}$$

or, alternatively, for fixed dimension d we expect mean-field behaviour for a decay exponent

$$\sigma < \frac{2d}{3}\,. \tag{3.40}$$

[1] We already set $[r_0] = [r]$ as well as $[u_0] = [u]$ as we are considering the Gaussian fixed point.

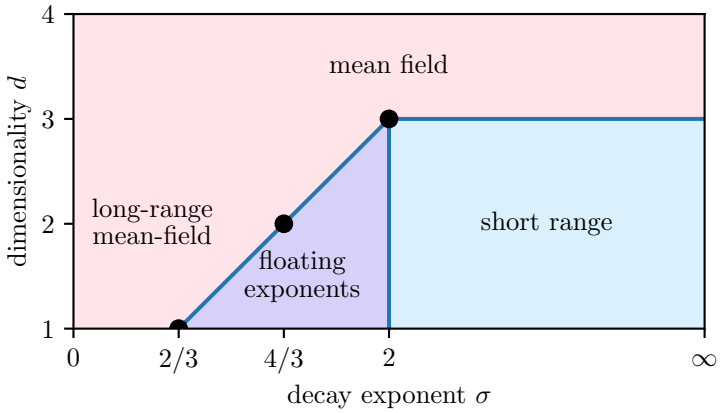

Figure 3.1: *Illustration of criticality regimes. The mean-field regime can be reached by either increasing the dimension d above $d_{\mathrm{uc}} = 3$ or tuning the long-range coupling $\sigma = \alpha - 1$ to $\sigma < \frac{2d}{3}$. The short-range regime is bounded from above by $d_{\mathrm{uc}} = 3$ and from the left by $\sigma = 2$. Corrections to this bound with $\sigma = 2 - \eta_{\mathrm{SR}}$ [63] are depicted by a dashed line with $\eta_{\mathrm{SR}}(\epsilon)$ from Ref. [49]. In between the long-range mean-field and short-range regime, the critical exponents vary continuously. The direction of the ϵ-expansion is visualised by coral arrows.*

The lower critical dimension $d_{\mathrm{lc}} = \sigma/2$ is readily extracted by demanding $[\phi] = 0$, meaning there is a phase transition for all $d \geq 1$ for $\sigma < 2$. For $\sigma \geq 2$ the model maps to the $(d+1)$-dimensional classical Ising model and therefore in total exhibits a phase transition for all σ and $d \geq 1$. Another approach for deriving the mean-field critical exponents was taken by Dutta et al. [32]. They read off the Gaussian propagator from the Gaussian action in Fourier space

$$\tilde{G}_0(q, \omega, r) = \frac{1}{b_\sigma q^\sigma + \tilde{g}\omega^2 + r} \tag{3.41}$$

to find the mean-field critical exponents. This readily yields the same exponents as in Eq. (3.38) and additionally gives

$$\eta = 2 - \sigma \qquad \text{and} \qquad \gamma = 1 \tag{3.42}$$

from $\tilde{G}_0(q, 0, 0) \sim q^{-(2-\eta)}$ as well as $\chi = \tilde{G}_0(0, 0, r) \sim r^{-\gamma}$. By inserting the mean-field critical exponents into the hyperscaling relation they then obtained the upper critical dimension. Dutta et al. [32] also performed a so-called ϵ-expansion [64] which is a perturbative RG calculation. In doing so, they interpret the dimension as a continuous variable and perform an expansion around the upper critical dimension in terms of $\epsilon = d_{\mathrm{uc}} - d$. As a result they found logarithmic corrections to scaling at $d = d_{\mathrm{uc}}$ and

confirmed the stability of the Gaussian fixed point for $d > d_{\mathrm{uc}}$, meaning that the above mean-field exponents hold in this regime.

In Fig. 3.1 the results from the field-theoretical description of this section are illustrated. Mean-field behaviour is expected for $d > 3$ as well as for $\sigma < \frac{2d}{3}$ while, from our considerations, the short-range criticality holds for $\sigma \geq 2$. For the intermediate regime $\frac{2d}{3} \leq \sigma \leq 2$ the critical exponents vary continuously and can be perturbatively calculated by an ϵ-expansion as it was done in Ref. [32]. However, it was argued for classical models with long-range Ising criticality [65] and recently also for the respective quantum models [63] that the boundary between the intermediate and short-range regime is shifted and the short-range universality class already holds for $\sigma \geq 2 - \eta_{\mathrm{SR}}$ with η_{SR} the anomalous dimension of the short-range model. Defenu et al. [63] argued based on RG flow equations that the coupling b_σ of the long-range interaction might be *irrelevant* and flows to zero for $\sigma \geq 2 - \eta_{\mathrm{SR}}$. This claim is supported by their functional RG calculations. At the corresponding RG fixed point, the long-range term is therefore expected to vanish and the short-range criticality is recovered.

3.3 One-dimensional linear chain

The LRTFIM for the one-dimensional linear chain is the main model studied in this thesis. We will distinguish between ferromagnetic and antiferromagnetic coupling as only in the nearest-neighbour limit $\alpha \to \infty$ those models are equivalent while for small α the expected behaviour differs. The nearest-neighbour limit is analytically solvable [7] with $h_{\mathrm{c}} = 1$ [1] and critical exponents of the classical two-dimensional Ising model solved by Onsager [58].

3.3.1 Ferromagnetic coupling

With the field-theoretical description we have so far established that the LRTFIM exhibits a zero-temperature phase transition from a quantum paramagnet to a ferromagnetically ordered state for every $\sigma > 0$ and also for every dimension $d \geq 1$. Moreover, in case of the one-dimensional chain, the long-range mean-field criticality applies for $\sigma < \frac{2}{3}$ [32] while for $\sigma \geq 2 - \eta_{\mathrm{SR}}$ the 2d-Ising criticality holds with $\eta_{\mathrm{SR}} = 0.25$ the respective anomalous dimension [63]. In between, for $\frac{2}{3} \leq \sigma \leq 2 - \eta_{\mathrm{SR}}$, the critical exponents vary continuously resulting in a continuum of universality classes. This intermediate regime yielding a continuum of universality classes is of particular interest and only arises for the one- and two-dimensional model.

[1] This follows immediately from the self-duality of the model.

The two-dimensional model was already studied by my fellow colleague Jan Alexander Koziol [44, 66] by means of the same quantum Monte Carlo (QMC) algorithm and by Fey et al. by means of a high-order series expansion [43] confirming the three regimes for the two-dimensional case. There are also some other numerical studies addressing the one-dimensional chain. The three different regimes were verified by high-order series expansion [42, 67] with which the gap exponent $z\nu$ as well as the critical points h_c were calculated. Another study combined exact diagonalisation and density-matrix renormalisation-group techniques (DMRG) with system sizes of up to $L = 240$ [68] calculating the critical exponent ν as well as the critical fields h_c for the intermediate regime. Furthermore, there is a related Monte Carlo study of a quantum spin chain coupled to a bosonic bath with varying spectral density which results in algebraically decaying interactions in imaginary-time when performing the quantum-classical mapping [69]. The critical exponents ν and z can be related by swapping spacetime directions and display the modified regime boundary $\sigma = 2 - \eta_\mathrm{SR}$ claimed by Ref. [63].

Apart from criticality, Vanderstraeten et al. [31] and Ritzau [70] have studied the quasiparticle excitations for the LRTFIM on the linear chain as a function of the decay exponent σ. While for large decay exponent, meaning relatively short-ranged interaction, the elementary excitations in the symmetry-broken state correspond to single domain walls, they found that upon lowering σ the energy cost of those domain walls rises and single spin flips become energetically favourable [31, 70].

There are also some investigations of the finite-temperature phase transitions of the one-dimensional LRTFIM. At finite temperature there is a line of continuous phase transitions for $\sigma < 1$ [32, 59] (see right diagram in Fig. 2.2) and no finite-temperature phase transition for $\sigma > 1$ (see left diagram in Fig. 2.2). For the special case of $\sigma = 1$, there is a line of Berezinski-Kosterlitz-Thouless (BKT) phase transitions [32, 59] which were already studied in depth in Refs. [59, 71, 72]. The long-range model with algebraic decay exponents $\sigma = 0.5$ and $\sigma = -0.95$, for which the Ising coupling has been normalised in order to ensure thermodynamic stability, has recently been studied by path integral Monte Carlo techniques while focusing on the finite-temperature regime [73].

Although a lot of research on the one-dimensional LRTFIM has been performed, there is to the best of our knowledge no study which derives the full set of critical exponents. Moreover, some of the studies have trouble matching the expectations in the short-range [69] or mean-field regime [42] or do not fully connect those well-understood limits [69]. We therefore aim to contribute to the understanding of the criticality of the one-dimensional LRTFIM by calculating the exponents ν, β and γ in all three regimes from which one is able to extract all other exponents via scaling relations. By explicitly studying the long-range Gaussian regime with trivial mean-field exponents,

we will contribute to the understanding of anomalous finite-size scaling behaviour above the upper critical dimension for quantum systems.

3.3.2 Antiferromagnetic coupling

The established picture for the antiferromagnetic LRTFIM on the hypercubic lattice is that it exhibits a continuous phase transition from an x-polarised phase for large fields to a symmetry-broken, antiferromagnetic state with staggered magnetisation for $\sigma > -d$ [39–42]. For $\sigma = -d$ all spins are coupled on equal footing and the ground state is infinitely degenerate for $h = 0$ with any finite h lifting this degeneracy leading to a paramagnetic ground-state [41]. The antiferromagnetic long-range model is numerically much more challenging than its ferromagnetic counterpart as the long-range coupling leads to geometric frustration for the antiferromagnetic coupling. There are less numerical studies and the existing results for the critical exponents are in disagreement for small $\sigma \leq 1.25$. For $\sigma > 1.25$ the long-range interaction is *irrelevant* [40] and the short-range criticality of the TFIM is recovered [40–42]. However, for $\sigma < 1.25$ an earlier study suggests that the long-range interaction is *relevant* and alters the criticality with continuously varying exponents [40] while a more recent study claims that the criticality remains of the short-range Ising type [41]. Although both of these studies are based on DMRG, they differ in their methods of extracting critical exponents. While Ref. [40] used the entanglement entropy, Ref. [41] employed the fidelity susceptibilty which might explain the discrepancy [41]. In any case, there is a demand for further numerical investigations of the antiferromagnetic LRTFIM in order to shed light on the question of its universality class(es).

3.4 Observables

This section introduces the observables of interest for the ferromagnetic four-dimensional TFIM as well as the ferro- and antiferromagnetic LRTFIM on the linear chain. We will use a QMC method to calculate quantum mechanical expectation values of observables O with

$$\langle O \rangle = \frac{\mathrm{tr}\left[O e^{-\beta \mathcal{H}}\right]}{\mathrm{tr}[e^{-\beta \mathcal{H}}]} \,. \tag{3.43}$$

The simulations are performed for finite lattices and at finite temperatures and therefore depend on the system size and β. We denote the linear system size with L and the respective expectation values with $\langle O \rangle_L$. The total amount of sites is given by $N = L^d$. The power-law singularities close to the critical point, as defined in Sec. 2.1, only occur in an infinite system while for a finite system one expects the singular behaviour to be rounded and shifted with respect to the critical point. A finite system appears to

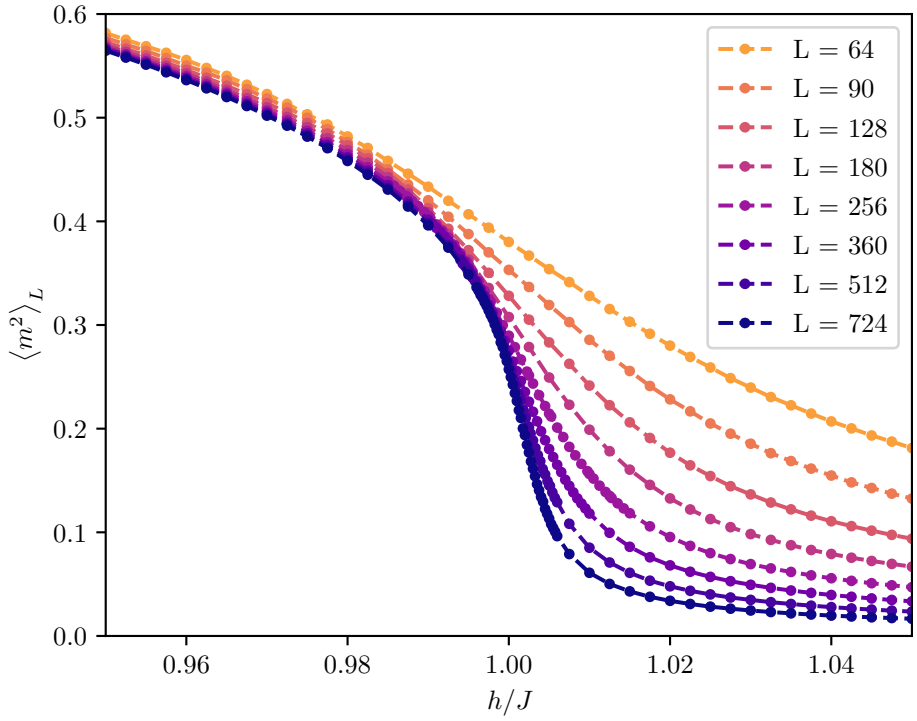

Figure 3.2: *Numerical data for the squared magnetisation for the ferromagnetic LRTFIM on the linear chain and with $\alpha = 10$ deep in the short-range regime. With increasing linear system size L the curves become gradually sharper. In the limit $L \to \infty$, the squared magnetisation $\langle m^2 \rangle_L$ vanishes for $h \geq h_c$.*

be critical when the characteristic length scale ξ becomes large enough in comparison to the system size L. Away from the critical point, where the physics is no longer dominated by fluctuations on large scales, the expectation values $\langle O \rangle_L$ for finite systems will tend to the value $\langle O \rangle_\infty$ for the infinite system.

The implementation details on how to extract the zero-temperature observables are postponed to Sec. 6.3 once we introduced the QMC method used in this thesis.

Magnetisation (order parameter): The order parameter for the LRTFIM is the magnetisation along the direction of the Ising coupling. We define the magnetisation as

$$m_{\boldsymbol{q}}^z = \frac{1}{N} \sum_{i=1}^{N} e^{-i\boldsymbol{q}\boldsymbol{r}_i} \sigma_i^z \tag{3.44}$$

with $\boldsymbol{q}$ the ordering wavevector of the respective phase. For ferromagnetic order the ordering wavevector is $\boldsymbol{q} = \boldsymbol{0}$ for arbitrary dimensions and lattices, yielding the uniform magnetisation. For the antiferromagnetic linear chain (1d) the ordering wavevector is $\boldsymbol{q} = \pi$, yielding the staggered magnetisation. We will from now on denote the magnetisation at the respective ordering wavevector with m. For an infinite system the magnetisation vanishes in the symmetric phase for $h > h_\mathrm{c}$ and monotonously increases in the ordered phase with $h < h_\mathrm{c}$ until it eventually saturates at $\langle m \rangle_\infty = 1$ for $h = 0$. For finite systems the expectation value of m will even vanish in the symmetry-broken phase as there is no real symmetry-breaking in finite systems [74]. One can instead measure the mean of its absolute value $\langle |m| \rangle_L$ or the root mean square $\sqrt{\langle m^2 \rangle_L}$ which become equivalent in the thermodynamic limit [74]

$$\lim_{L\to\infty} \langle |m| \rangle_L = \lim_{L\to\infty} \sqrt{\langle m^2 \rangle_L} = \langle m \rangle_\infty \ . \tag{3.45}$$

In Fig. 3.2, the squared magnetisation for different system sizes L is shown for the ferromagnetic LRTFIM in the short-range regime. In the disordered phase the curves converge to zero for increasing L and the soft transition for small L from non-zero magnetisation to vanishing magnetisation becomes gradually sharper for increasing L.

Binder cumulant: The Binder cumulant is a useful quantity for pinpointing the critical point. It measures the Gaussian character of the order-parameter distribution and changes at the phase transition due to the symmetry-breaking. For a scalar order parameter it is defined by

$$U_L = \frac{3}{2}\left(1 - \frac{\langle m^4 \rangle_L}{3\,\langle m^2 \rangle_L^2}\right) . \tag{3.46}$$

The Binder cumulant becomes independent of the system size L at the critical point $h = h_\mathrm{c}$ with $U_L(h = h_\mathrm{c})$ being universal [75]. For an infinite system in the disordered phase, where the order-parameter distribution $P_\infty(m)$ is Gaussian around zero, the Gaussian integrals

$$\langle m^n \rangle_\infty = \int_{-\infty}^{\infty} m^n P_\infty(m)\,\mathrm{d}m \tag{3.47}$$

yield $\langle m^4 \rangle_\infty = 3\,\langle m^2 \rangle_\infty^2$ and the cumulant vanishes for infinite systems [46, 75]. In the ordered phase the fluctuations in m disappear and the order-parameter distribution $P_\infty(m)$ tends to two δ-peaks at $\pm\langle |m| \rangle_\infty$ [46]. Therefore $\langle m^4 \rangle_\infty = \langle m^2 \rangle_\infty^2$ leading to $U_\infty = 1$ [59, 75]. For finite systems, where the order-parameter distributions $P_L(m)$ are only approximately Gaussian in the disordered phase and the δ-peaks of the infinite systems in the ordered phase are broadened and tilted, the Binder cumulant U_L tends to the respective bulk values U_∞ for increasing L [74]. This behaviour of the Binder cumulant is depicted in Fig. 3.3 for different system sizes L. All curves intersect at a common point $(h_\mathrm{c}, U(h_\mathrm{c}))$ pinpointing the phase transition.

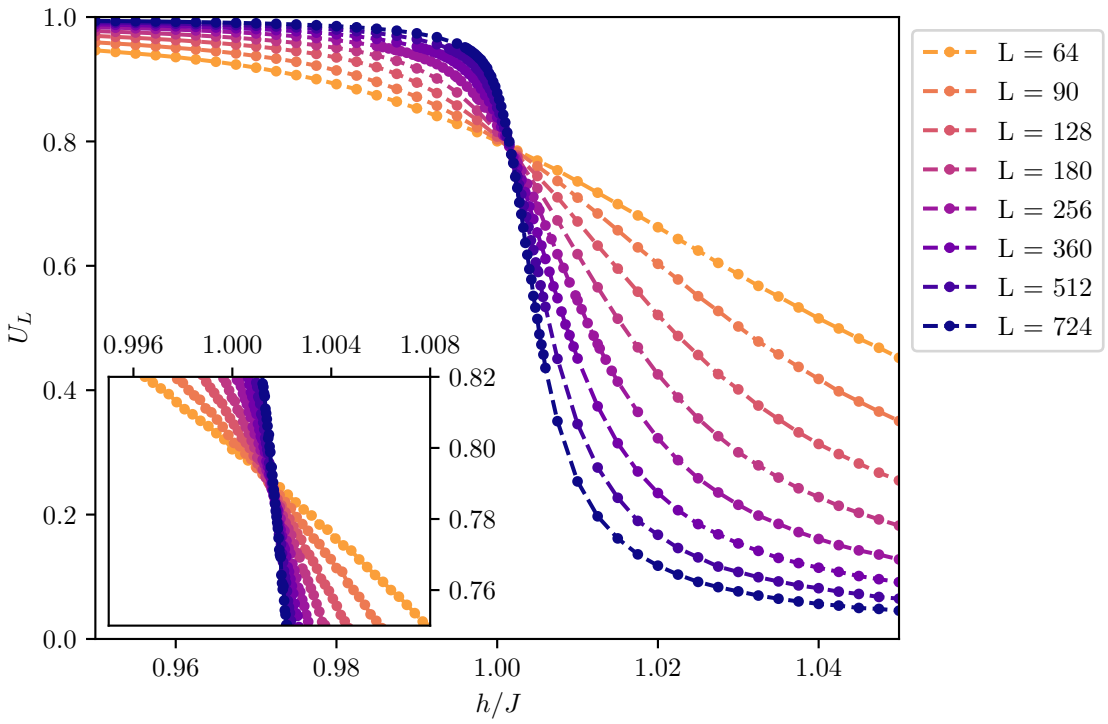

Figure 3.3: *Numerical data for the Binder cumulant for the ferromagnetic LRTFIM on the linear chain and with $\alpha = 10$ deep in the short-range regime plotted for different system sizes L. The intersection of all curves gives an estimate for the critical point h_c. In the limit $h/J \to 0$ and $h/J \to \infty$, the curves approach $U_L \to 1$ and $U_L \to 0$ respectively. With increasing linear system size L, the curves become gradually steeper around the critical point.*

Order-parameter susceptibility: The order-parameter susceptibility is given by the response of the magnetisation to a perturbation $\mathcal{H} \to \mathcal{H} - HM$ with respect to the conjugate field H coupling to the extensive magnetisation $M = L^d m$

$$\begin{aligned} \chi_L &= \left.\frac{\partial \langle m \rangle_L}{\partial H}\right|_{H=0} \\ &= L^d \int_0^\beta \langle m(\tau) m(0) \rangle_L \, \mathrm{d}\tau - L^d \beta \langle m \rangle_L^2 \end{aligned} \tag{3.48}$$

where $m(\tau) = e^{\tau H} m e^{-\tau H}$ is the magnetisation in the Heisenberg picture and τ is an imaginary-time variable. It is a main difference of quantum systems that their response functions, describing the correlations of the system, contain an imaginary-time integral like in Eq. (3.48) as quantum-mechanical operators generally do not commute. If

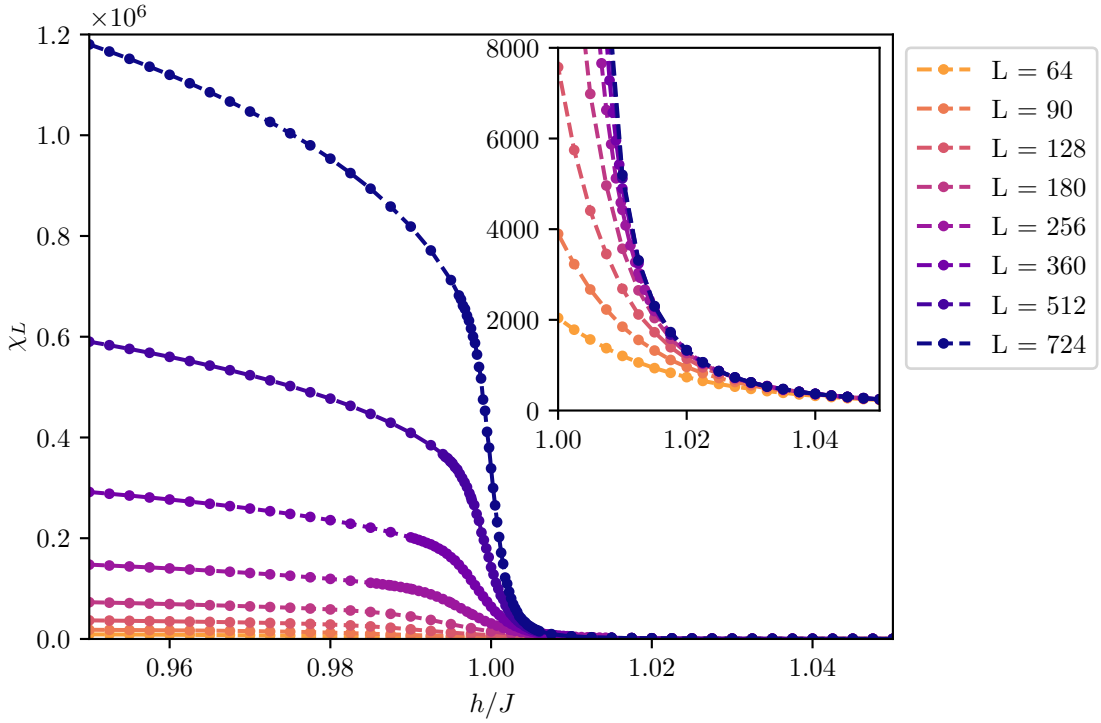

Figure 3.4: *Numerical data for the susceptibility Eq. (3.50) for the ferromagnetic LRTFIM on the linear chain and with $\alpha = 10$ deep in the short-range regime plotted for different system sizes L. The temperature was chosen to scale as $\beta \sim L^z$ due to the scaling properties of observables in the vicinity of the quantum critical point (see Sec. 4.4). In the limit $h \to 0$ and $h \to \infty$, the susceptibility approaches $\chi_L \to \beta L$ and $\chi_L \to 0$ respectively. With increasing linear system size L the curves become gradually steeper around the critical point.*

$[m, \mathcal{H}] = 0$, then Eq. (3.48) would immediately reduce to the classical susceptibility [59]

$$\chi_{\text{class},L} = L^d \beta \left\langle m^2 \right\rangle_L - L^d \beta \left\langle m \right\rangle_L^2 . \tag{3.49}$$

As $\langle m \rangle_L$ will vanish not only in the disordered phase but also in the ordered phase, Eq. (3.48) will reduce to

$$\chi_L = L^d \int_0^\beta \langle m(\tau) m(0) \rangle_L \, \mathrm{d}\tau \tag{3.50}$$

and only yields the correct susceptibility in the disordered phase. In Fig. 3.4 this susceptibility is depicted for different system sizes L. Coming from the disordered

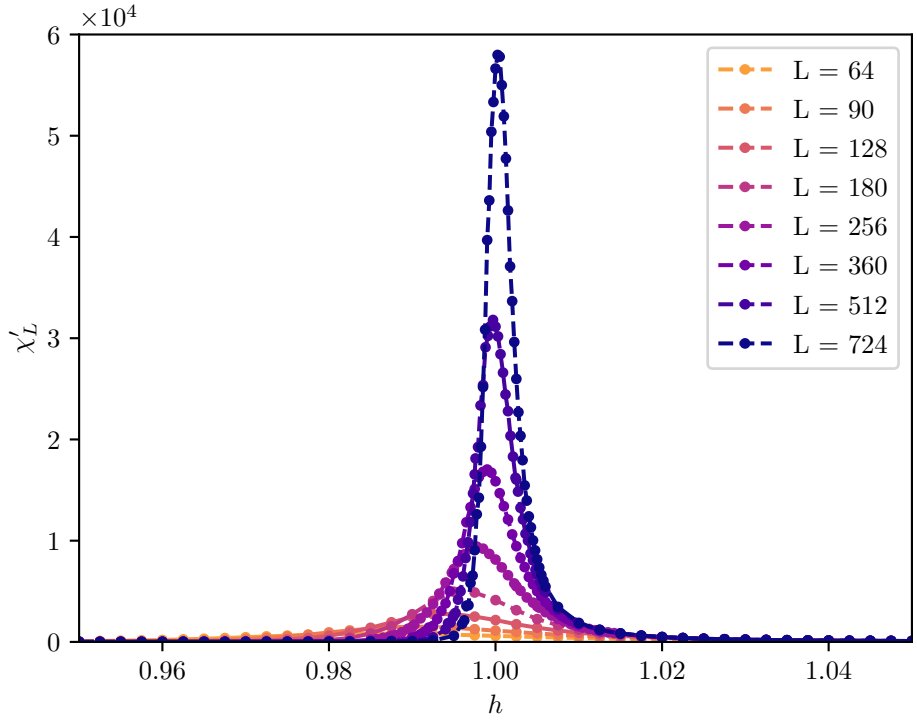

Figure 3.5: *Numerical data for the susceptibility Eq. (3.51) for the ferromagnetic LRTFIM on the linear chain and with $\alpha = 10$ deep in the short-range regime plotted for different system sizes L. The temperature was chosen to scale as $\beta \sim L^z$ due to the scaling properties of observables in the vicinity of the quantum critical point (see Sec. 4.4). In the limit $h \to 0$ and $h \to \infty$, the susceptibility χ'_L vanishes. With increasing linear system size L the peak becomes gradually sharper and its centre shifts towards the bulk critical point h_c.*

phase, it exhibits a steep increase around the critical point and eventually starts to saturate when the correlation length ξ_τ in imaginary time becomes comparable to β. For $h \to 0$ the curves converge towards βL^d.

If one is interested in a susceptibility that also vanishes in the ordered phase, one might define

$$\begin{aligned} \chi'_L &= L^d \int_0^\beta \langle m(\tau)m(0)\rangle_L \, \mathrm{d}\tau - \frac{L^d}{\beta} \left\langle \left| \int_0^\beta m(\tau)\mathrm{d}\tau \right| \right\rangle_L^2 \\ &= \frac{L^d}{\beta} \mathbf{Var} \left\{ \left| \int_0^\beta m(\tau)\mathrm{d}\tau \right| \right\}_L \end{aligned} \tag{3.51}$$

in analogy to the treatment for the classical susceptibility with $\langle m\rangle_L \to \langle|m|\rangle_L$ [74] yielding $\chi'_{\text{class},L} = L^d\beta\mathbf{Var}\left\{|m|\right\}_L$.[1] χ'_L exhibits a peak close to the phase transition which becomes gradually sharper for increasing system size L as depicted in Fig. 3.5. We want to note that the peak position depends on the temperature β and in order to compare different system sizes one needs to choose an inverse temperature $\beta \sim L^z$ [2] rendering the temperature effects comparable. Moreover, for a fixed system size L, we expect the peak to shift towards $h \to 0$ in the limit $\beta \to \infty$ as the system effectively becomes a one-dimensional classical Ising model which is only ordered at $T_{\text{class}} = 0$ ($\hat{=}\ h = 0$). It is common to use Eq. (3.48) in simulations for quantum systems [76] and we will also adopt this definition as we are not interested in the susceptibility in the ordered phase.

Correlation function and its characteristic length: The characteristic length scale embodied in the correlation function plays a pivotal role at continuous phase transitions as its divergence leads to a scale-free system at the critical point. It is a subtle quantity which is hard to extract or even define on a finite lattice. However, it will play a key role in the description of finite-size scaling above the upper critical dimension in Sec. 4.3.1. The formalism we will exploit is premised on the finite-size behaviour of the characteristic length scale in the vicinity of the critical point.

This characteristic length scale is incorporated in the order-parameter correlation function and gives the distance at which the correlations switch to their long-distance behaviour. The order-parameter correlation function is defined by the linear response of the local magnetisation σ_i^z at site i with respect to a perturbing field H_j coupling to σ_j^z in the Hamiltonian ($\mathcal{H} \to \mathcal{H} - H_j\sigma_j^z$)

$$\begin{aligned} G_L(\boldsymbol{r}_i - \boldsymbol{r}_j, \omega = 0) &= \left.\frac{\partial \langle\sigma_i^z\rangle_L}{\partial H_j}\right|_{H_j=0} \\ &= \int_0^\beta \left\langle \sigma_i^z(\tau)\sigma_j^z(0)\right\rangle_L \mathrm{d}\tau \ , \end{aligned} \tag{3.52}$$

where we already neglected the second term $\beta\langle\sigma_i^z\rangle_L\langle\sigma_j^z\rangle_L = \beta\langle\sigma_i^z\rangle_L^2$ vanishing for finite systems. The correlation function Eq. (3.52) is the zero-frequency component of the Fourier transform of the imaginary-time correlation function

$$G_L(\boldsymbol{r}_i - \boldsymbol{r}_j, \tau) = \left\langle \sigma_i^z(\tau)\sigma_j^z(0)\right\rangle_L \ , \tag{3.53}$$

[1] If one would use $\langle|m|\rangle_L^2$ instead of $\left\langle\left|\int_0^\beta m(\tau)\mathrm{d}\tau\right|\right\rangle_L^2$ in the quantum-mechanical susceptibility as suggested in Ref. [59] this would lead to negative values of the susceptibility.

[2] This will become clearer in the following chapter on finite-size scaling.

which also contains information on the dynamics of the system. In this thesis, we are not interested in any dynamical properties and will therefore only consider the zero-frequency correlation function in Eq. (3.52) as well as the equal-time correlation function

$$G_L(\boldsymbol{r}_i - \boldsymbol{r}_j, \tau = 0) = \left\langle \sigma_i^z \sigma_j^z \right\rangle_L , \tag{3.54}$$

which might be reminiscent of classical systems.

We will use the Fourier transform of both correlation functions to extract the characteristic length scale in the long-range mean-field regime, where the criticality is described by a Gaussian field theory. The long-range correlation function in Fourier space is given by the propagator of the long-range Gaussian field theory [32, 53]

$$\tilde{G}(q, \omega) \sim \frac{1}{b_\sigma q^\sigma + \tilde{g}\omega^2 + m^2} \tag{3.55}$$

with m the characteristic energy scale, which in terms of the *relevant* coupling r is given by $m^2 = r$. This yields the zero-frequency and equal-time correlation functions [59]

$$\tilde{G}(q, \omega = 0) \sim \frac{1}{b_\sigma q^\sigma + m^2} , \tag{3.56}$$

$$\tilde{G}(q, \tau = 0) \sim \frac{1}{2\sqrt{\tilde{g}}\sqrt{b_\sigma q^\sigma + m^2}} . \tag{3.57}$$

For a finite system, the definition of a characteristic length scale is not unique [77]. There are several definitions for ξ_L which will converge to ξ_∞ for $L \to \infty$ [77]. For long-range systems finding a suitable definition for the characteristic length is even more difficult, as the correlation function does not exhibit the usual exponential decay for gapped systems but decays algebraically even away from the critical point [78]. Common definitions that are tailored for correlation lengths, which specify the exponential decay of a correlation function at long distances, such as the second moment

$$\xi_\infty^{(2)} = \sqrt{\frac{1}{2d} \frac{\int |\boldsymbol{r}|^2 G(\boldsymbol{r}) \, \mathrm{d}r}{\int G(\boldsymbol{r}) \, \mathrm{d}r}} \tag{3.58}$$

therefore might yield $\xi_\infty^{(2)} = \infty$ in an infinite system not only at the critical point, but also for $h \neq h_\mathrm{c}$ [79].

We will instead consider the definition [53]

$$\xi_L^{(\mathrm{LR}\omega)} = \frac{1}{q_\mathrm{min}} \left[\frac{\tilde{G}_L(0, \omega = 0) - \tilde{G}_L(q_\mathrm{min}, \omega = 0)}{\tilde{G}_L(q_\mathrm{min}, \omega = 0)} \right]^{1/\sigma} \tag{3.59}$$

with $q_{\min} = 2\pi/L$ the smallest wavevector fitting on the finite lattice. By inserting Eq. (3.56)

$$\begin{aligned}\xi_L^{(\mathrm{LR}\omega)} &= \frac{1}{q_{\min}} \left[\frac{b_\sigma q_{\min}^\sigma + m_L^2}{m_L^2} - 1 \right]^{1/\sigma} \\ &= b_\sigma^{1/\sigma} m_L^{-2/\sigma}\end{aligned} \tag{3.60}$$

the momentum dependency cancels. In case of the equal-time correlation function, we take the square of $\tilde{G}(q, \tau = 0)$ in order to get rid of the square-root in Eq. (3.57) which yields a slightly modified formula

$$\begin{aligned}\xi_L^{(\mathrm{LR}\tau)} &= \frac{1}{q_{\min}} \left[\frac{\tilde{G}_L^2(0, \tau = 0) - \tilde{G}_L^2(q_{\min}, \tau = 0)}{\tilde{G}_L^2(q_{\min}, \tau = 0)} \right]^{1/\sigma} \\ &= b_\sigma^{1/\sigma} m_L^{-2/\sigma}\end{aligned} \tag{3.61}$$

for the same quantity. In the limit $L \to \infty$, the estimates for the characteristic length exhibit the correct singularity

$$\xi_\infty^{\mathrm{LR}} = b_\sigma^{1/\sigma} m_\infty^{-2/\sigma} \sim |r|^{-\nu} \tag{3.62}$$

with $m_\infty \sim |r|^{z\nu}$ and long-range mean-field critical exponents $z = \sigma/2$.

3.5 Boundary conditions for finite systems

For the simulation of the respective finite systems we use periodic boundary conditions in order to preserve the system's translational invariance. For the nearest-neighbour model the implementation of periodic boundary conditions is straightforward and one simply connects the outermost spins of the finite lattice with their counterparts on the opposite side of the system, thereby folding the finite system to a d-dimensional torus.

However, for the long-range interactions

$$J_{ij} = \frac{J}{2} \frac{1}{|\boldsymbol{r}_i - \boldsymbol{r}_j|^\alpha} \tag{3.63}$$

the naive approach of simply using the smallest distance between site i and j disregards interactions that would be present in an infinite system. A better approximation of the thermodynamic limit can be achieved by virtually extending the finite system with replicas of itself, thereby rendering the system virtually infinite [53, 59, 80]. All the couplings of a site i to replicas of a site j are then added to the bare coupling to site j. The couplings J_{ij} are modified according to

$$\frac{1}{|\boldsymbol{r}_i - \boldsymbol{r}_j|^\alpha} \to \sum_{n_1,\ldots,n_d=-\infty}^{\infty} \frac{1}{\left| \boldsymbol{r}_i - \boldsymbol{r}_j + L \sum_{i=1}^d n_i \boldsymbol{e}_i \right|^\alpha} \tag{3.64}$$

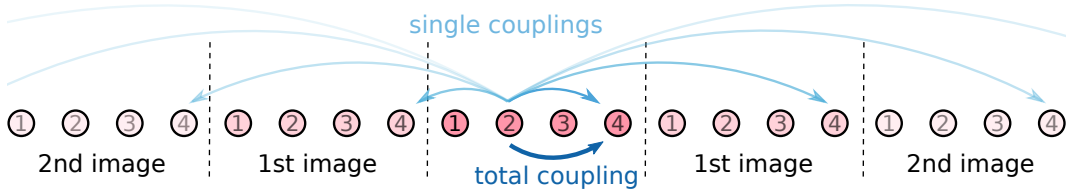

Figure 3.6: *Illustration of the corrected couplings by taking into account the couplings that are cut off in systems of finite extent. The images of the finite system build up the infinite system and the couplings of all the replicas are added to the total coupling among the respective spins in the original system. The total coupling consists of all the single couplings. Here the bare coupling J_{ij} of spin $i = 2$ to spin $j = 4$ is supplemented with the single couplings of spin 2 to all replicas of site 4.*

with $\boldsymbol{e}_i$ the lattice vectors connecting adjacent sites. This procedure is visualised in Fig. 3.6 for the linear chain. The summation over replicas Eq. (3.64) for $d = 1$ can be written in terms of the Hurwitz zeta function

$$\zeta(s, q) \coloneqq \sum_{n=0}^{\infty} \frac{1}{(q+n)^s} \tag{3.65}$$

leading to a modified coupling

$$J_{ij} = \frac{1}{L^\alpha} \left[\zeta\left(\alpha, \frac{|i-j|}{L}\right) + \zeta\left(\alpha, \frac{L-|i-j|}{L}\right) \right] \tag{3.66}$$

for the one-dimensional chain. In order to compute the corrected couplings for $d > 1$, one either needs to cut the sums in Eq. (3.64) or use the Ewald summation, which is a technique for calculating such slowly convergent sums with enhanced convergence in comparison to a direct summation (see Ref. [81] for details).

We want to note that the specific choice of boundary conditions is also important in the context of finite-size scaling [53] which we will discuss in the following chapter. Above the upper critical dimension, free boundary conditions as well as periodic boundary conditions without replicas would lead to a finite-size behaviour at the critical point from which the critical exponents are not derivable [38, 53].[1] We will implicitly focus on periodic boundary conditions when discussing finite-size scaling above the upper critical dimension.

[1] In contrast to finite-size behaviour at the bulk critical point, the finite-size behaviour at the pseudocritical points would contain information about the critical exponents [38].

4 Finite-size scaling

Even though continuous phase transitions can only occur in infinite systems, it is possible to study their criticality by investigating their finite counterparts. In finite systems the power-law singularities of the infinite system are rounded and shifted with respect to the critical point $r = 0$ [82]. For example, the susceptibility with its characteristic divergence at $r = 0$ is deformed to broadened peaks of finite height with peak positions $r_L = \frac{g_L - g_c}{g_c}$ shifted away from the critical point. This defines an L-dependent pseudo-critical point g_L with $\lim_{L\to\infty} g_L = g_c$. As the characteristic length ξ diverges at the critical point, the system will at some point "feel" its finite size and the rounding sets in [83]. As we expect the deviation to set in when the characteristic length scale reaches a certain value,[1] it is very plausible that the extent of this rounding depends on how fast this length diverges and therefore depends on the critical exponent ν. Similarly, the peak height depends on how fast the quantity diverges (i. e. α, γ) and the region in parameter space where the finite system starts to deviate from the infinite system (rounding, ν). This vague consideration shows that the critical exponents have implications on how thermodynamic quantities in finite systems behave, making it possible to derive criticality of infinite systems from knowledge about finite systems [82]. The dependency of the peak position, height and width from the linear system size is illustrated in Fig. 4.1 using the susceptibility in Eq. (3.51) as an example.

Finite-size scaling (FSS) is the formal description of this rounding in finite systems and is mainly used in terms of extracting critical properties from numerical data [83]. It is based on a hypothesis going back to Widom that thermodynamic quantities close to the critical point should be described by generalised homogeneous functions (GHF) [52, 84]. FSS extends this idea of homogeneity to finite systems. Although introduced heuristically [82], FSS was later proven based on RG in the absence of *dangerous irrelevant variables* (DIV) [85]. In the presence of DIV the situation is less understood. Albeit one can absorb the singular behaviour due to DIV in the scaling functions, the correlation sector was thought to be unaffected by DIV [34, 86]. In the

[1] It is commonly claimed that the characteristic length ξ is bounded by the system size and when $\xi \approx L$ the rounding sets in. We deliberately beat around the bush here as the finite-size formalism we use above the upper critical dimension explicitly violates this claim that L/ξ is the relevant ratio.

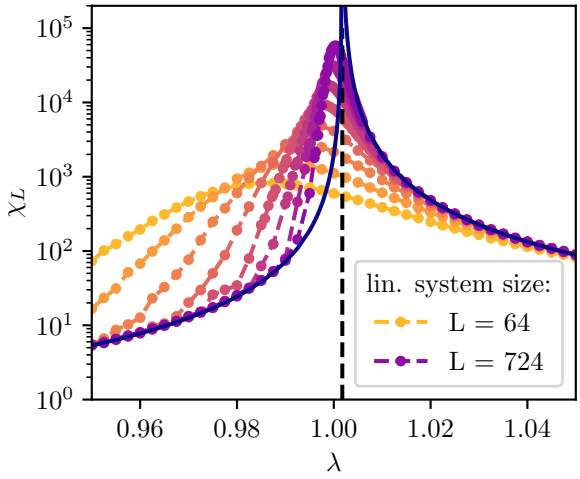

Figure 4.1: *Numerical data of the order-parameter susceptibility Eq. (3.51) for the ferromagnetic linear chain with decay exponent $\alpha = 10$ and linear system size L. The y-axis is logarithmic in order to make all peaks visible. The finite-size peaks of the susceptibility are rounded and shifted with respect to the bulk critical field (dashed black line). For increasing system size, the peaks become sharper and shift towards the bulk critical field.*

framework of FSS this gave rise to the heuristic introduction of another length scale l by Binder [35] which he termed *thermodynamic length*. A modern approach, called Q-FSS, proposed by Kenna and Berche [36] claims that the correlation sector is affected by DIV after all. It reconciles the scaling due to RG with the critical exponents predicted by mean-field theory while maintaining the exclusive role of a single characteristic length scale in FSS. However, Q-FSS was developed for classical systems and extending this idea to quantum systems is not straightforward. From numerical studies of the LRTFIM [66], an adaption to quantum systems was proposed by my colleague [44]. Apart from additional numerical data for the ferromagnetic LRTFIM in 1d and the TFIM in 4d supporting this proposal, this thesis gives a microscopic argument for this approach which we will discuss in this chapter.

This chapter is structured as follows. We start by introducing the scaling of infinite systems in Sec. 4.1 as the basis of FSS. As GHFs play a fundamental role, we introduce them in Sec. 4.1.1 while focusing on the properties that are useful in the context of the scaling hypothesis. In Sec. 4.1.2 we state the scaling hypothesis. Starting from the hypothesis for classical systems we promptly turn to the quantum case. We restrict the detailed discussion to the quantum systems as this is the case we are interested in. The literature for scaling of quantum systems is not as extensive as for the classical case and we therefore mainly use the description by Cardy [83] by extending it to the quantum

case. Albeit there are subtle differences in the resulting scaling forms, the discussion of classical and quantum systems is completely analogous. For a thorough discussion of both cases we refer to Ref. [44]. After showing the downfall of this scaling theory in the mean-field regime, we introduce the treatment of DIV in Sec. 4.1.3. We then turn our attention to finite systems and describe standard FSS which is applicable below the upper critical dimension in Sec. 4.2. The formal generalisation to FSS above the upper critical dimension is straightforward, but there are free parameters due to the DIV treatment which we will fix in Sec. 4.3. Interpreting the FSS form above the upper critical dimension is a delicate issue and we introduce two approaches in Sec. 4.3.1. We first describe the historical treatment by adding an additional characteristic length termed *thermodynamic length* and then discuss a more recent approach proposed by Kenna and Berche [36]. This modern approach is not straightforwardly applicable to quantum systems and it is a main result of this thesis to extend the approach pursued by Kenna et al. [36] to quantum systems. This chapter closes with a short summary on Q-FSS for quantum systems in Sec. 4.4.

4.1 Scaling in infinite systems

As the finite-size scaling hypothesis is based on the scaling hypothesis in infinite systems, we start by a discussion of bulk scaling. The scaling hypothesis will use the notion of GHFs and in order to appreciate the significance and consequences of the scaling hypothesis, we will start this section with a brief introduction to GHFs.

4.1.1 Generalised homogeneous functions

We follow Ref. [87] for the description and properties of GHFs. All theorems are deduced from there and the proofs thereof can be found in Ref. [87].

Definition 4.1. *A function $f(x_1, \ldots, x_n)$ is a GHF if there exist $a_1, \ldots, a_n \in \mathbb{R}$ and $a_f \in \mathbb{R}$ such that for all $\lambda > 0$*

$$f(\lambda^{a_1} x_1, \ldots, \lambda^{a_n} x_n) = \lambda^{a_f} f(x_1, \ldots, x_n). \tag{4.1}$$

The numbers a_i are the scaling powers of the variables x_i respectively and a_f denotes the scaling power of the function $f(x_1, \ldots, x_n)$. Only n of these $n+1$ scaling powers are independent as only the ratios of the scaling powers are fixed. This can be shown by setting $\lambda \to \lambda' = \lambda^p$ leading to [87]

$$f(\lambda^{pa_1} x_1, \ldots, \lambda^{pa_n} x_n) = \lambda^{pa_f} f(x_1, \ldots, x_n) \tag{4.2}$$

with a common rescaling of all scaling powers a_i and a_f. A GHF with scaling power $a_f = 0$ is called a scale-invariant function [87]. For $a_f \neq 0$ one can always rescale the scaling powers by a factor $p = 1/a_f$ such that $a'_f = pa_f = 1$ [87].

Before we start with the theorems, we note that for two GHFs $f(x_1, \ldots, x_n)$ and $g(x_1, \ldots, x_n)$ with common scaling powers $a_1, \ldots, a_n$ and scaling powers a_f and a_g respectively

- the function f^r with power $r \in \mathbb{R}$ is a GHF with scaling power $a_f \cdot r$
- the product fg is a GHF with scaling power $a_f + a_g$
- the sum $f \pm g$ is a GHF if and only if $a_f = a_g$.

Theorem 4.1. *Let $f(x_1, \ldots, x_n)$ be a GHF with scaling power a_f, then the partial derivative*

$$f'_i(x_1, \ldots, x_n) = \frac{\partial}{\partial x_i} f(x_1, \ldots, x_n) \tag{4.3}$$

is also a GHF with scaling power $a_f - a_i$.

By transitivity, Theorem 4.1 also holds for all higher-order and mixed partial derivatives.

Theorem 4.2. *Let $f(x_1, \ldots, x_n)$ be a GHF with scaling power a_f, then the Legendre transform*

$$f^*(x_1, \ldots, x_i^*, \ldots, x_n) = f(x_1, \ldots, x_i, \ldots, x_n) - x_i x_i^* \tag{4.4}$$

with the conjugate variable $x_i^* = \frac{\partial f}{\partial x_i}$ is also a GHF with scaling power $a_f^* = a_f$.

Likewise, Theorem 4.2 holds for all Legendre transforms of a GHF by transitivity. In accordance to Theorem 4.1, the scaling power of the conjugate variable x_i^* is given by $a_i^* = a_f - a_i$.

Theorem 4.3. *A function $f(x_1, \ldots, x_n)$ is a GHF if and only if there exist some functions $g_{i,\mathrm{sgn}(x_i)}(y_1, \ldots, y_{i-1}, y_{i+1}, \ldots, y_n)$ for all $i \in \{1, \ldots, n\}$ such that*

$$f(x_1, \ldots, x_n) = |x_i|^{a_f/a_i} g_{i,\mathrm{sgn}(x_i)} \left(\frac{x_1}{|x_i|^{a_1/a_i}}, \ldots, \frac{x_{i-1}}{|x_i|^{a_{i-1}/a_i}}, \frac{x_{i+1}}{|x_i|^{a_{i+1}/a_i}}, \ldots \right). \tag{4.5}$$

The functions $g_{i,\mathrm{sgn}(x_i)}$ are related with the GHF f by

$$g_{i,\mathrm{sgn}(x_i)}(y_1, \ldots, y_{i-1}, y_{i+1}, \ldots, y_n) = f(y_1, \ldots, y_{i-1}, \mathrm{sgn}(x_i), y_{i+1}, \ldots, y_n). \tag{4.6}$$

By setting all $x_{j \neq i} = 0$ in Eq. (4.5), one observes that a GHF f has a power-law singularity at the origin [87]

$$f(0, \ldots, 0, x_i, 0, \ldots, 0) \sim |x_i|^{a_f/a_i} \tag{4.7}$$

when approaching the origin along one of the principal axes. The exponent of the power law is given by the ratio of a_f/a_i.

Theorem 4.4. *Let $f(x_1, \ldots, x_n)$ be a GHF with scaling power a_f, then the Fourier transform*

$$\tilde{f}(x_1, \ldots, \tilde{x}_i, \ldots, x_n) = \int f(x_1, \ldots, x_n) e^{x_i \tilde{x}_i} \, \mathrm{d}^d x_i \tag{4.8}$$

is a GHF with scaling power $\tilde{a}_f = a_f + d a_i$ with d denoting the dimension of the variable x_i and the variable $\tilde{x}_i$ being conjugate to x_i. The scaling power of the conjugate variable $\tilde{x}_i$ is given by $\tilde{a}_i = -a_i$.

Implications on scaling: We will briefly deduce the implications on scaling of thermodynamic functions from the theorems stated above.

- All thermodynamic functions can be deduced from Legendre transformations of thermodynamic potentials and their partial derivatives. If one thermodynamic potential is a GHF, then all thermodynamic potentials and functions are GHFs by Theorem 4.1 and Theorem 4.2 [87].
- For thermodynamic functions which are GHFs, the ratio of scaling powers a_f/a_i found for the power-law singularities in Eq. (4.7) can be directly related to critical exponents [87].
- The GHF property is conserved when transforming a GHF to the Fourier space and back [87]. For instance, $G(\boldsymbol{r}, \tau)$ is a GHF if and only if $G(\boldsymbol{r}, \omega)$ is a GHF.

Note that the thermodynamic functions do not need to be and in general are no GHFs. However, close to a phase transition, their singular parts become GHFs asymptotically.

4.1.2 Scaling hypothesis

We will now state the scaling hypothesis, which describes the scaling of an infinite system. The scaling hypothesis does not differ for quantum and classical systems, although the scaling powers and variables of the respective GHF do differ.

Scaling hypothesis [87]:

> *The Gibbs free energy density can be divided into a regular part and one which is singular at the critical point. The singular part f of the Gibbs free energy density is asymptotically a GHF close to the critical point.*

When we talk of the free energy, we from now on always refer to the singular part of it. In Ref. [87] the authors also defined a separate scaling hypothesis for correlation

functions. However, the scaling hypothesis for the correlation function implies the scaling hypothesis stated above [87]. On the contrary, the correlation function is a second-order derivative with respect to local conjugate fields $H(\boldsymbol{r})$ [83] conserving the GHF property. The GHF property of the characteristic length follows from the GHF property of the correlation function and was shown to hold for a family of functions resembling correlation lengths including the second-moment definition Eq. (3.58) in Ref. [87].

Only with the groundwork of RG, the origin of the scaling hypothesis was understood [49, 83]. The scaling powers of the variables in the GHF can be related with the scaling powers from field theory [83]. We will now state the scaling hypothesis in terms of equations for a spin system with control parameter r and a field H conjugate to the order parameter and pad them with RG ideas heuristically.

Classical phase transition: The scaling hypothesis states that we can write the singular part f of the Gibbs free energy density and the characteristic length scale ξ as

$$f(r, H, u, \dots) = b^{-d} f(b^{y_r} r, b^{y_H} H, b^{y_u} u, \dots)\,, \tag{4.9}$$

$$\xi(r, H, u, \dots) = b\xi(b^{y_r} r, b^{y_H} H, b^{y_u} u, \dots)\,, \tag{4.10}$$

where we choose $\lambda^{-a_f} = b^{-d}$ and $\lambda^{-a_\xi} = b$ as, by virtue of the RG idea, we interpret the homogeneity as a spatial rescaling by a rescaling factor b [83]. As we previously claimed that the partition function and therefore the free energy should remain invariant under an RG transformation, the free energy density should rescale as an inverse volume $\sim b^d$ and the factor b^{-d} in Eq. (4.9) compensates for that. Similarly, the characteristic length scale should rescale as a length $\sim b^{-1}$ leading to a compensating factor of b in Eq. (4.10). We further identify the scaling powers of the variables with their respective scaling powers from RG, i. e. $y_a = [a]$ [83]. We recall that the control parameter r and the conjugate field H were found to be *relevant* and u was found to be *irrelevant* at the fixed point describing the criticality. In fact, from RG one finds that a full spectrum of *irrelevant* couplings emerges [49] from which u is the most *relevant*, meaning the scaling power y_u of u is smaller than zero but larger than the scaling powers of all other *irrelevant* couplings [49]. The reason we can neglect the spectrum of *irrelevant* couplings can be illustrated by using Theorem 4.3 and rewriting Eq. (4.9) to

$$f(r, H, u, \dots) = |r|^{d/y_r} \mathcal{F}_{r,\mathrm{sgn}(r)} \left(\frac{H}{|r|^{y_H/y_r}}, \frac{u}{|r|^{y_u/y_r}}, \dots \right) \tag{4.11}$$

with $y_u/y_r < 0$ since $y_r > 0$ (*relevant*) and $y_u < 0$ (*irrelevant*). The function $\mathcal{F}_{r,\mathrm{sgn}(r)}$ is a so-called scaling function. Those functions are found to be universal [49]. Upon approaching the critical point $|r| \to 0$, the second argument $u|r|^{-y_u/y_r}$, representing all

irrelevant variables for the moment, flows to zero due to its *irrelevance*. We therefore bluntly drop the dependence on all *irrelevant* couplings including u and write

$$f(r,H) = b^{-d} f(b^{y_r} r, b^{y_H} H)\,, \tag{4.12}$$
$$\xi(r,H) = b\xi(b^{y_r} r, b^{y_H} H)\,. \tag{4.13}$$

Quantum phase transition: In comparison to the classical case, the scaling forms are slightly modified

$$f(r,H,T) = b^{-(d+z)} f(b^{y_r} r, b^{y_H} H, b^z T) \tag{4.14}$$
$$\xi(r,H,T) = b\xi(b^{y_r} r, b^{y_H} H, b^z T) \tag{4.15}$$

by adding the scaling of the imaginary-time dimension to the rescaling of the volume $\lambda^{a_f} = b^{d+z}$ and supplementing f with the temperature T as an additional *relevant* variable. The temperature, being the inverse length of the imaginary time, is rescaled with a scaling power $y_T = -[\tau] = z$. Note that we already dropped the dependece on u and the other *irrelevant* variables. We recall that the control parameter r for a QPT is strictly non-thermal, contrary to thermal phase transitions.

We obtain the GHF formulation for the magnetisation as well as the order-parameter susceptibility by differentiating Eq. (4.14) with respect to the conjugate field H

$$m(r,H,T) = b^{-(d+z)+y_H} m(b^{y_r} r, b^{y_H} H, b^z T) \tag{4.16}$$
$$\chi(r,H,T) = b^{-(d+z)+2y_H} \chi(b^{y_r} r, b^{y_H} H, b^z T) \tag{4.17}$$

and the control-parameter susceptibility by differentiating twice with respect to the control parameter

$$\chi_r(r,H,T) = b^{-(d+z)+2y_r} \chi_r(b^{y_r} r, b^{y_H} H, b^z T)\,. \tag{4.18}$$

The scaling law for the correlation function is given by [83]

$$G(\boldsymbol{x},\omega=0,r,H,T) = b^{-2d-z+2y_H} G(b^{-1}\boldsymbol{x},\omega=0,b^{y_r} r, b^{y_H} H, b^z T)\,. \tag{4.19}$$

With Theorem 4.3 and Eq. (4.7) one can reproduce the singularities of thermodynamic functions in terms of critical exponents. As an example, we consider the magnetisation

$$m(r,H,T) = |r|^{(d+z-y_H)/y_r} \mathfrak{m}_{r,\mathrm{sgn}(r)}\left(\frac{H}{|r|^{y_H/y_r}}, \frac{T}{|r|^{z/y_r}}\right)\,, \tag{4.20}$$
$$m(r,H,T) = |H|^{(d+z-y_H)/y_H} \mathfrak{m}_{H,\mathrm{sgn}(H)}\left(\frac{r}{|H|^{y_r/y_H}}, \frac{T}{|H|^{z/y_H}}\right) \tag{4.21}$$

and demand that the singular behaviour of the magnetisation is given by the respective critical exponents (see Tab. 2.1)

$$m(r, H = 0, T = 0) = |r|^{\beta} m_{r,\mathrm{sgn}(r)}(0, 0) \,, \tag{4.22}$$

$$m(r = 0, H, T = 0) = |H|^{1/\delta} m_{H,\mathrm{sgn}(H)}(0, 0) \,. \tag{4.23}$$

Comparing the exponents grants us with an expression for the critical exponents β and δ in terms of the scaling powers y_a. The same can be conducted for the exponents of the order-parameter susceptibility (γ) and control-parameter susceptibility (α) as well as the characteristic length (ν) and correlation function (η). This leads to the following relations:

$$\beta = \frac{d + z - y_H}{y_r} \,, \tag{4.24}$$

$$\delta = \frac{y_H}{d + z - y_H} \,, \tag{4.25}$$

$$\gamma = -\frac{d + z - 2y_H}{y_r} \,, \tag{4.26}$$

$$\alpha = -\frac{d + z - 2y_r}{y_r} \,, \tag{4.27}$$

$$\nu = \frac{1}{y_r} \tag{4.28}$$

$$\eta = d + z - 2y_H + 2. \tag{4.29}$$

It's time to fully appreciate this result. As these six exponents solely depend on the scaling powers $(d + z)$, y_H and y_r, they cannot be independent. This results in the formulation of four scaling relations independent of y_H and y_r. These scaling relations were already stated in Sec. 2.1.2 and can be checked by simply inserting Eqs. (4.24) – (4.29) into them (see Eqs. (2.8) – (2.11)).

Long-range Gaussian exponents for the LRTFIM: In Sec. 3.2.2 we derived the scaling powers of the Gaussian fixed point from the field theory of the LRTFIM (see Eqs. (3.34) – (3.37)). This fixed point was identified to be the fixed point describing the criticality of the model in the long-range mean-field regime $\sigma < \frac{2d}{3}$ [32]. Those scaling powers can be used to derive the critical exponents by inserting them into Eqs. (4.24) – (4.29) which we just derived. The resulting predictions for the exponents are listed in Tab. 4.1 together with the predictions from mean-field theory. It turns out that some of the Gaussian exponents depend on the dimension while mean-field theory predicts the same exponents for all $d \geq d_{\mathrm{uc}}$. The predictions are inconsistent for α, β and δ; only for $d = d_{\mathrm{uc}}$ all exponents coincide. Moreover, one might notice that the concordant exponents (γ, ν, z, η) are all related to the correlation function. This was also observed in Ref. [86] for the classical Ising model and the author concluded that there is something wrong in the free energy sector, leading to a failure in the predictions of α, β and δ. This is not unique to the long-range model. In full analogy, we could derive the Gaussian predictions for the short-range TFIM and observe a dissonance for the same critical exponents.

Table 4.1: *Predictions for critical exponents from the long-range Gaussian field-theory and mean-field critical exponents. For $d = d_{\mathrm{uc}} = \frac{3\sigma}{2}$ the predictions from mean-field and Gaussian field theory coincide, but for $d > d_{\mathrm{uc}}$ the exponents β, δ and α differ. The same could be conducted for the mean-field exponents of the short-range TFIM with $d \geq d_{\mathrm{uc}} = 3$ leading to a similar result.*

Critical exponents	β	δ	γ	α	ν	z	η
Gaussian predictions	$\frac{d}{2\sigma} - \frac{1}{4}$	$\frac{2d+3\sigma}{2d-\sigma}$	1	$\frac{3}{2} - \frac{d}{\sigma}$	$\frac{1}{\sigma}$	$\frac{\sigma}{2}$	$2 - \sigma$
Mean-field predictions	$\frac{1}{2}$	3	1	0	$\frac{1}{\sigma}$	$\frac{\sigma}{2}$	$2 - \sigma$

The origin of this discrepancy lies in a subtle mistake we did when we build our scaling theory. As we identified u as an *irrelevant* variable, which will flow to zero, we set $u = 0$ right from the beginning. However, for $d > d_{\mathrm{uc}}$ this leads to wrong predictions in scaling because the free energy is singular in the limit $u \to 0$. The variable u is therefore termed *dangerous irrelevant variable* (DIV) [88]. In fact, if we would continue to construct finite-size scaling based on this scaling theory, none of the predictions would be fully met. In the following subsection we will properly take u into account.

4.1.3 Scaling in the presence of dangerous irrelevant variables

An established way to treat DIVs is to absorb their singular behaviour into the definition of the other variables [34, 88]. For the free energy being singular in the limit $u \to 0$ we

assume for small u [34]

$$f(r, H, T, u) = u^{p_{(d+z)}} \overline{f}(u^{p_r} r, u^{p_H} H, u^{p_T} T) \,, \tag{4.30}$$

meaning the dependence on u can be absorbed into the other variables up to a global power of u. This implies a modified scaling for the free energy [34, 53]

$$f(r, H, T) = b^{-(d+z)^*} f(b^{y_r^*} r, b^{y_H^*} H, b^{z^*} T) \tag{4.31}$$

with

$$(d+z)^* = (d+z) - p_{(d+z)} y_u \,, \tag{4.32}$$

$$y_r^* = y_r + p_r y_u \,, \tag{4.33}$$

$$y_H^* = y_H + p_H y_u \,, \tag{4.34}$$

$$z^* = z + p_z y_u \,. \tag{4.35}$$

Following Ref. [53], we derive relations between the modified scaling powers y_a^* and the critical exponents. The derivation is in full analogy to the derivation of Eqs. (4.24) – (4.27) in which we compared the singular behaviour of free energy derivatives with their expected singular behaviour in terms of critical exponents. This yields the relations

$$\beta = \frac{(d+z)^* - y_H^*}{y_r^*} \,, \tag{4.36}$$

$$\delta = \frac{y_H^*}{(d+z)^* - y_H^*} \,, \tag{4.37}$$

$$\gamma = -\frac{(d+z)^* - 2y_H^*}{y_r^*} \,, \tag{4.38}$$

$$\alpha = -\frac{(d+z)^* - 2y_r^*}{y_r^*} \,. \tag{4.39}$$

One can check that the Widom and Essam scaling relation are still valid as they completely canceled all scaling powers, including $(d+z)^*$. However, the hyperscaling relation includes the scaling power of the free energy density and y_r^* and is therefore modified above the upper critical dimension. The new hyperscaling relation is given by

$$2 - \alpha = \frac{(d+z)^*}{y_r^*} \,, \tag{4.40}$$

where the modified scaling powers need yet to be determined. We now claim that those modified scaling powers shall reproduce the mean-field predictions $\beta = 1/2$, $\delta = 3$, $\gamma = 1$ and $\alpha = 0$ [53]. Solving for the modified scaling powers yields

$$y_r^* = \frac{(d+z)^*}{2} \,, \tag{4.41}$$

$$y_H^* = \frac{3(d+z)^*}{4} \,. \tag{4.42}$$

Those relations are insufficient to fix all scaling powers and one needs another independent relation. This is to be expected because, as we earlier noticed, the critical exponents are only related to the *ratio* of the scaling powers and we have a freedom in the GHF structure to rescale all scaling powers by a common factor (see Eq. (4.2)). If we go to the scaling of finite systems, we will introduce an additional scaling variable, namely the system size itself. We fix its scaling power to $[L] = -1$ as we effectively want to perform a spatial coarse-graining. Fixing one scaling power corresponds to fixing all of them and one can derive an additional relation for the modified scaling powers. For classical systems, where the free energy has scaling power d, Binder [34] gave three *finite-size* arguments for $d^* = d$, meaning $p_d = 0$. However, this does not hold for the quantum case and we will see that $p_{(d+z)} \neq 0$. Before we derive this result, we need to derive the finite-size scaling form starting from FSS below the upper critical dimension.

4.2 Finite-size scaling below the upper-critical dimension

As mentioned in the beginning of this chapter, one can derive critical properties from finite systems even though they do not exhibit a phase transition in the strict meaning. Up to now, we discussed the scaling for infinite systems. Let us now turn to their finite counterparts by following Ref. [83]. In the construction of the scaling for infinite systems we interpreted the homogeneity as the spatial rescaling with factor b. We therefore extend the scaling Eq. (4.14) and Eq. (4.15) to

$$f_L(r, H, T) = b^{-(d+z)} f_{L/b}(b^{y_r} r, b^{y_H} H, b^z T)\,, \tag{4.43}$$

$$\xi_L(r, H, T) = b\xi_{L/b}(b^{y_r} r, b^{y_H} H, b^z T) \tag{4.44}$$

by treating the system lenght L as an additional scaling variable with the spatial scaling power $[\boldsymbol{x}] = -1$ [83]. For an observable $\mathcal{O}$ diverging as $\mathcal{O}(r, H = 0, T = 0) \sim |r|^\omega$ with critical exponents ω, e. g. $\omega = \beta$ for the magnetisation $\mathcal{O} = m$, we expect the scaling behaviour [48]

$$\mathcal{O}(r, H, T) = b^{-y_r\omega} \mathcal{O}(b^{y_r} r, b^{y_H} H, b^z T)\,. \tag{4.45}$$

Once again, we extend this scaling to finite systems

$$\mathcal{O}_L(r, H, T) = b^{-y_r\omega} \mathcal{O}_{L/b}(b^{y_r} r, b^{y_H} H, b^z T) \tag{4.46}$$

by introducing the linear system size L as an additional scaling variable. This relates the observables of a system with linear size L to one with linear size L/b. We can choose a reference length L_0 and rescale all systems to this length by setting $b = L/L_0$. Choosing $L_0 = 1$ yields

$$\mathcal{O}_L(r, H, T) = L^{-y_r\omega} \Omega(L^{y_r} r, L^{y_H} H, L^z T) \tag{4.47}$$

with Ω being a universal scaling function. By using $y_r = 1/\nu$ we get the finite-size scaling form

$$\mathcal{O}_L(r, H, T) = L^{-\omega/\nu}\Omega(L^{1/\nu}r, L^{y_H}H, L^z T) \tag{4.48}$$

in terms of the critical exponents ω and ν. When measuring $\mathcal{O}_L$ for several system lengths L and control parameters r, one can compare those to derive the critical exponents as well as the location of the critical point h_c from $r = (h - h_\mathrm{c})/h_\mathrm{c}$.

Finally, we want to cast Eq. (4.48) into another form in order to understand the historical approach to FSS above the upper critical dimension. Consider the behaviour along one of the principal axes, e. g. $H = T = 0$, and replace the remaining variable, here r, with the characteristic length scale $\xi_\infty \sim |r|^{-\nu}$ of the infinite system. This yields

$$\mathcal{O}_L(r) = \mathcal{O}_\infty(r)\left(\frac{L}{\xi_\infty}\right)^{-\omega/\nu}\Omega'\left(\frac{L^{1/\nu}}{\xi_\infty^{1/\nu}}\right) \tag{4.49}$$

$$= \mathcal{O}_\infty(r)F(L/\xi_\infty) \tag{4.50}$$

where we expanded the right side with the scaling of the infinite system $\mathcal{O}_\infty(r) \sim \xi_\infty^{-\omega/\nu}$, absorbed the coefficient into the definition of Ω' and introduced $F(x) = x^{-\omega/\nu}\Omega'(x^{1/\nu})$. This grants us with the FSS hypothesis phrased as [85]

$$\frac{\mathcal{O}_L(r)}{\mathcal{O}_\infty(r)} = F\left(\frac{L}{\xi_\infty}\right). \tag{4.51}$$

The finite-size behaviour is therefore said to be goverened by the ratio of the two length scales involved, namely L/ξ_∞ [83].[1] The characteristic length scale ξ_L is said to be bounded by the linear system size and the rounding sets in when $\xi_\infty \approx L$.

4.3 Finite-size scaling above the upper-critical dimension

The FSS form above the upper critical dimension for an observable $\mathcal{O}$ with divergence $\mathcal{O} \sim |r|^\omega$ is

$$\mathcal{O}_L(r, H, T) = L^{-y_r^*\omega}\Omega(L^{y_r^*}r, L^{y_H^*}H, L^{z^*}T) \tag{4.52}$$

where the deduction is completely analogous to FSS below the upper critical dimension with the only difference being that the scaling powers are modified $y_a \to y_a^*$.

[1] The lattice scale does not matter close to the critical point.

We will now take the first argument in Ref. [34] and transfer it to the quantum case. For this we consider the magnetisation and order-parameter susceptibility in a finite system

$$m_L(r,H,T) = \frac{\partial f}{\partial H} = L^{-(d+z)^*+y_H^*}\mathcal{M}(L^{y_r^*}r, L^{y_H^*}H, L^{z^*}T)\,, \tag{4.53}$$

$$\chi_L(r,H,T) = \frac{\partial^2 f}{\partial H^2} = L^{-(d+z)^*+2y_H^*}\mathcal{X}(L^{y_r^*}r, L^{y_H^*}H, L^{z^*}T) \tag{4.54}$$

with $\mathcal{M}$ and $\mathcal{X}$ being universal scaling functions. The susceptibility in a finite system at $H = T = 0$ is given by an infinite integral over imaginary time

$$\chi_L = L^d \int_0^\infty \langle m(\tau)m(0)\rangle_L \,\mathrm{d}\tau\ . \tag{4.55}$$

The correlations in imaginary time decay exponentially $\langle m(\tau)m(0)\rangle_L \sim e^{-\Delta_L\tau}\langle m\rangle_L^2$ with the finite-size energy gap $\Delta_L \sim \xi_{\tau,L}^{-1}$. Inserting this into the integral, we can perform the integration which yields

$$\chi_L \sim L^d \Delta_L^{-1}\langle m\rangle_L^2\ . \tag{4.56}$$

In the limit $L \to \infty$, the energy gap Δ_L and $\langle m\rangle_L^2$ take on their bulk values of the infinite system and the susceptibility scales as

$$\chi_L \sim L^d |r|^{-z\nu}|r|^{2\beta} \qquad \text{for} \quad L \to \infty\,. \tag{4.57}$$

We require the scaling function $\mathcal{X}$ to scale as

$$\lim_{x\to\pm\infty} \mathcal{X}(x,0,0) \sim |x|^{2\beta-z\nu} \tag{4.58}$$

in order to reproduce the correct singular behaviour in $|r|$ in the infinite system. We then insert this into Eq. (4.54)

$$\chi_L \sim L^{-(d+z)^*+2y_H^*} L^{y_r^*(2\beta-z\nu)}|r|^{2\beta-z\nu} \tag{4.59}$$

and, in order to match Eq. (4.57), compare the powers of L with L^d

$$d = -(d+z)^* + 2y_H^* + y_r^*(2\beta - z\nu)\,. \tag{4.60}$$

Finally, we insert Eq. (4.36) to eliminate β and set $\nu = 1/y_r$ leading to

$$d + \frac{y_r^*}{y_r} z = (d+z)^*\,. \tag{4.61}$$

As anticipated, the result is qualitatively different in comparison to the classical case, in which $d^* = d$ [34]. Together with the two relations Eq. (4.41) and Eq. (4.42) one can now solve for the modified scaling powers yielding

$$(d+z)^* = d + \frac{d}{d_{\mathrm{uc}}} z \qquad y_r^* = \frac{d}{d_{\mathrm{uc}}} y_r \qquad y_H^* = \frac{3}{4}(d + \frac{d}{d_{\mathrm{uc}}} z) \tag{4.62}$$

$$= \frac{4d}{3}\,, \qquad = \frac{2d}{3}\,, \qquad = d\,, \tag{4.63}$$

$$p_{(d+z)} = \frac{1}{3}\,, \qquad p_r = -\frac{2}{3}\,, \qquad p_H = -\frac{1}{2}\,, \tag{4.64}$$

where the first line only uses equations derivable from the dimensional analysis of the ϕ^4-theory and in the second line the interaction in imaginary time is implicitly assumed to be short-ranged. The equations therefore hold for the TFIM with short-range as well as long-range interactions in arbitrary dimensions and other models described by the ϕ^4-theories encountered in Sec. 3.2. We additionally added the factors p_a defined by $y_a^* = y_a + p_a y_u$ and $(d+z)^* = d + z - p_{(d+z)} y_u$ for completeness. Note that below the upper critical dimension all scaling powers retain their unmodified values $y_a^* \to y_a$ and the equations above yield $y_a^* = y_a$ for $d = d_{\mathrm{uc}}$.

4.3.1 Modified finite-size scaling hypothesis

We now want to rephrase the FSS form Eq. (4.52) similar to the FSS hypothesis below the upper critical dimension by a comparison of the length scales L and ξ_∞. By setting $H = T = 0$ in Eq. (4.52)

$$\mathcal{O}_L(r) = \mathcal{O}_\infty(r) \left(\frac{L}{|r|^{-1/y_r^*}} \right)^{-y_r^* \omega} \Omega'(L^{y_r^*} r)\,, \tag{4.65}$$

we realize that the linear system size L is not compared with the characteristic length scale diverging as $\xi_\infty \sim |r|^{-1/y_r}$ close to the critical point but with a quantity diverging as $\sim |r|^{-1/y_r^*}$. We will now describe two approaches to resolve this issue.

Thermodynamic length: The historical approach by Binder [35, 89] is to interpret Eq. (4.65) by introducing another length scale [89]

$$l_\infty \sim |r|^{-1/y_r^*} \tag{4.66}$$

with which the linear system size L scales. This length is called *thermodynamic length*. By the relation $y_r^* = \frac{d}{d_{\mathrm{uc}}} y_r$, it is related to the characteristic length ξ_∞ according to

$$l_\infty \sim \xi_\infty^{y_r/y_r^*} = \xi_\infty^{d_{\mathrm{uc}}/d}\,. \tag{4.67}$$

Above d_{uc} the thermodynamic length l_∞ has a weaker divergence than the characteristic length ξ_∞ and it seems somewhat implausible that L scales with l_∞ rather than with ξ_∞ [89]. Below d_{uc}, where $y_r^* \to y_r$, the two length scales are proportional to each other. Above the upper critical dimension the scaling hypothesis of an observable $\mathcal{O}$ is then given by

$$\frac{\mathcal{O}_L(r)}{\mathcal{O}_\infty(r)} = F\left(\frac{L}{l_\infty}\right), \tag{4.68}$$

where L is now compared with the thermodynamic length l_∞ of the infinite system. Albeit this approach works in the sense that one can extract the correct critical exponents [89], including ν via $\nu = d/(d_{\mathrm{uc}} y_r^*)$, it is rather phenomenological. Besides the introduction of another length scale with no physical motivation, the question remains why L should scale with l_∞ instead of ξ_∞.

Q-FSS: There is a key difference in the Q-FSS approach followed by Kenna and Berche [36] and the approach by Binder. Q-FSS is based on the claim that the correlation sector is also affected by DIV [36]

$$\xi(r, H, T) = b^{\text{ϙ}} \xi(b^{y_r^*} r, b^{y_H^*} H, b^{z^*} T), \tag{4.69}$$

which only reproduces the correct scaling behaviour with respect to r if

$$\text{ϙ} = \frac{y_r^*}{y_r} = \frac{d}{d_{\mathrm{uc}}} \tag{4.70}$$

for $d > d_{\mathrm{uc}}$. The archaic greek letter ϙ is pronounced as "koppa". For $d \to d_{\mathrm{uc}}$ the standard FSS is restored with $\text{ϙ} = 1$. One main reason why the correlation sector was thought to be unaffected for a long time might be that the Gaussian predictions for the critical exponents connected to the correlation sector coincide with the mean-field predictions (see Tab. 4.1 and Ref. [86]). Another reason hampering this approach was the belief that the characteristic length ξ_L in a finite system should be bounded by the linear system size L [34]. However, when extending Eq. (4.69) to finite systems analogous to Eq. (4.52), this yields

$$\xi_L(r, H, T) = L^{\text{ϙ}} \Xi(L^{y_r^*} r, L^{y_H^*} H, L^{z^*} T) \tag{4.71}$$

explicitly violating the bound by L. This violation of an upper bound $\sim L$ is supported by numerical studies above the upper critical dimension for classical systems with short-range [36, 90] as well as long-range interaction [53, 91]. The finite-size hypothesis can then be reformulated as [53]

$$\frac{\mathcal{O}_L(r)}{\mathcal{O}_\infty(r)} = F\left(\frac{L^{\text{ϙ}}}{\xi_\infty}\right) \tag{4.72}$$

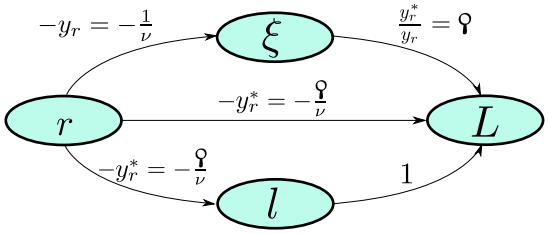

Figure 4.2: *Illustration of both approaches for FSS above the upper critical dimension. The rounding of observables in the scaling function Ω' in Eq. (4.65) is governed by the parameter $\tilde{r} = L^{y_r^*} r$ such that for constant argument $\tilde{r}$, the control parameter scales as $r \sim L^{-y_r^*}$ (middle path). This can be achieved by introducing the thermodynamic length $l_\infty \sim |r|^{-1/y_r^*}$ scaling as $l_L \sim L$ and controlling FSS with the ratio $l_L/l_\infty \sim L/l_\infty$ (lower path). In contrast, the modern approach termed Q-FSS claims that ξ_L is not bounded by L, but $\xi_L \sim L^\wp$, such that FSS is controlled by the ratio $\xi_L/\xi_\infty \sim L^\wp/\xi_\infty$, thereby avoiding the introduction of an additional length scale.*

with the finite-size characteristic length ξ_L scaling as $L^\wp$ instead of L. In contrast to the approach with the thermodynamic length, this approach does not require an additional length scale and maintains the importance and uniqueness of the characteristic length ξ in FSS.

In Fig. 4.2 we illustrate the difference in the two approaches. By that, we want to stress that the thermodynamic length l is not just the characteristic length, but a different length scale. Their divergence differs above the upper critical dimension. Both approaches lead to a correct FSS description of thermodynamic quantities except for the FSS of the characteristic length scale. The finite-size behaviour of ξ_L is only properly addressed by the Q-FSS approach.

Wittmann et al. [92] and Flores-Sola et al. [38] further investigated the role of Fourier modes and boundary conditions by means of FSS above the upper critical dimension and found that for periodic boundary conditions[1] only the zero mode of the field $\tilde{\phi}(\boldsymbol{k} = 0)$ is affected by the DIV [92]. Zero-momentum quantities, such as the uniform magnetisation, susceptibility and also the finite-size characteristic length that we consider,[2] therefore exhibit Q-FSS. In contrast, non-zero modes yield standard FSS with Gaussian fixed-point exponents [38] (see Tab. 4.1).

[1] For free boundary conditions the situation is more complicated and we refer to Refs. [38, 92] for details.

[2] As mentioned previously, there is no unique definition for finite-size characteristic lengths and some definitions are no zero-momentum quantities. For details, see Ref. [77].

This distinction of zero and non-zero modes is important in the context of the exponent η as it is usually defined by non-zero modes in contrast to the other critical exponents. Former measurements of η for classical systems yielded negative η-like exponents [93–95] and Kenna and Berche addressed this issue by introducing another anomalous dimension $\eta_\wp$ [**?**]. The anomalous dimension is often defined by the k-dependence of $\tilde{G}(\boldsymbol{k}, \omega = 0, r = 0) \sim k^{-(2-\eta_\wp)}$ or the spatial decay of $G(\boldsymbol{x}, \omega = 0, r = 0) \sim \boldsymbol{x}^{-(d-2+\eta_\wp)}$ at the critical point $r = 0$. However, both definitions are governed by non-zero modes. The Fisher scaling relation therefore connects the exponent of a zero-momentum quantity affected by DIV, namely

$$\chi_L(r) = L^{\wp\gamma/\nu} \mathcal{X}(L^{\wp/\nu} r)\,, \tag{4.73}$$

with quantities that are not affected by DIV and scale as

$$G_L(\boldsymbol{x}, \omega = 0, r) = L^{-(d-2+\eta_\wp)} \mathcal{G}(L^{-1}\boldsymbol{x}, \omega = 0, L^{1/\nu} r)\,. \tag{4.74}$$

Using the fluctuation-dissipation theorem at the critical point $r = 0$

$$\begin{aligned}
\chi_L(r = 0) &= \int_0^L G_L(\boldsymbol{x}, \omega = 0)\, \mathrm{d}^d\boldsymbol{x} && (4.75)\\
&= \int_0^L L^{-(d-2+\eta_\wp)} \mathcal{G}(\boldsymbol{x}/L, \omega = 0)\, \mathrm{d}^d\boldsymbol{x} && (4.76)\\
&= L^{2-\eta_\wp} \int_0^1 \mathcal{G}(\boldsymbol{u}, \omega = 0)\, \mathrm{d}^d\boldsymbol{u} && (4.77)\\
&= L^{2-\eta_\wp} \mathcal{X}(r = 0), && (4.78)
\end{aligned}$$

this, by comparison with Eq. (4.73), resulted in a modified Fisher scaling relation [**?**]

$$2 - \eta_\wp = \frac{\wp\gamma}{\nu}\,. \tag{4.79}$$

Above the upper critical dimension, where γ and ν attain their mean-field values and $\wp = \frac{d}{d_{\mathrm{uc}}} > 1$, this η-like exponent $\eta_\wp$ depends on the dimension and can also become negative, e. g. for the short-range TFIM and classical Ising model [93–95]. We want to note that integrating the spatial correlation function in Eq. (4.75) yields the zero mode of its Fourier transform which should be affected by DIV. As we already took the limit $u \to 0$ for the correlation function in real space Eq. (4.74), we probably lost information about the singular behaviour of the zero-mode in u.

4.4 Summary: Q-FSS for quantum systems

We follow the Q-FSS description by Kenna et al. [**?**, 36–38, 91] and within this chapter we extended its mechanism to quantum models. In order to unify the FSS form of observables below and above the upper critical dimension, we rephrase it as

$$\mathcal{O}_L(r, H = 0, T = 0) = L^{-\wp\omega/\nu}\Omega(L^{\wp/\nu}r, H = 0, T = 0) \tag{4.80}$$

by extending the definition of $\wp$ to [**?**, 53]

$$\wp = \max\left(1, \frac{d}{d_{\mathrm{uc}}}\right) \tag{4.81}$$

such that $\wp = d/d_{\mathrm{uc}}$ above and $\wp = 1$ below the upper critical dimension.

Furthermore, we earlier found a hyperscaling relation for $d > d_{\mathrm{uc}}$ (see Eq. (4.40)) which we can by now cast into the form

$$2 - \alpha = (d + \wp z)\,\frac{\nu}{\wp} \tag{4.82}$$

unifying the hyperscaling relation and therefore rendering it valid below and above the upper critical dimension. This hyperscaling relation was already proposed in Ref. [44] based on a numerical study [66]. Within this chapter it was derived analytically based on microscopic arguments.

We will use this approach to FSS in order to extract critical exponents from finite-size quantities. By Eq. (4.80) one can extract the critical exponents $\nu/\wp$ and $\wp\omega/\nu$ of an observable $\mathcal{O}$ by comparing $\mathcal{O}_L$ for different linear system sizes L and control parameters r. We defer a detailed description of two explicit methods to Sec. 6.5. The generalised hyperscaling relation Eq. (4.82) together with the Rushbrooke relation will come in handy for calculating z from γ/ν and β/ν. Those exponents are extracted from FSS of the squared magnetisation $\langle m^2\rangle_L$ and the order-parameter susceptibility χ_L calculated by means of QMC simulations. We hereby close the theoretical part of this thesis and move on to the numerical investigation of the LRTFIM and Q-FSS starting with an introduction to Monte Carlo.

5 Monte Carlo integration

In this thesis we utilise Monte Carlo (MC) integration in order to calculate ground-state expectation values of the LRTFIM. Those expectation values can be written as high-dimensional integrals (or discrete sums) over a configuration space C that in general can not be evaluated analytically. In contrast to deterministic numerical integration techniques which use discrete sampling points, Monte Carlo integration is based on randomised samples $x_i \in C$. The effort of the discretised approach scales exponentially with the dimension [96]. In contrast, the Monte Carlo integration breaks with this "curse of dimensionality" [96]. This randomised approach is therefore especially advantageous for high-dimensional integrals as those encountered in statistical physics.

The problem of interest is the calculation of an integral. In particular, we are interested in expectation values with an underlying probability distribution $P(x)$

$$\langle \mathcal{O} \rangle_P = \int_C \mathrm{d}x \, \mathcal{O}(x) P(x) \, . \tag{5.1}$$

This integral can be approximated by drawing M random configurations $x_i \in C$ uniformly and averaging over these [74]

$$\overline{\mathcal{O}} = \frac{\sum_{i=1}^{M} P(x_i)\mathcal{O}(x_i)}{\sum_{i=1}^{M} P(x_i)} \, . \tag{5.2}$$

This naive approach is called *simple sampling* [74]. However, a uniform sampling scheme is not advisable in our case as the integrand, namely $P(x)\mathcal{O}(x)$, varies strongly due to $P(x)$. If we were to draw the configurations x_i uniformly, we would often draw configurations which contribute only little to the physics as their weight $P(x_i)$ is exponentially small or even vanishes [74]. Every now and then, we would draw a configuration with moderate weight, but most of the time, we would waste samples for dispensable configurations which contribute very little to $\langle \mathcal{O} \rangle_P$ or not at all. Instead of sampling x_i uniformly, one can perform *importance sampling* and draw x_i according to a distribution $Q(x)$. The estimates for the average are then given by [74]

$$\overline{\mathcal{O}} = \frac{\sum_{i=1}^{M} P(x_i)\mathcal{O}(x_i)/Q(x_i)}{\sum_{i=1}^{M} P(x_i)/Q(x_i)} \, , \tag{5.3}$$

where a factor $Q(x_i)$ is introduced to compensate for the non-uniform sampling. A natural and fruitful choice is $Q(x) = P(x)$ [74] for generating the samples according to

their physical relevance. Eq. (5.3) then reduces to a simple arithmetic mean [74]

$$\overline{\mathcal{O}} = \frac{1}{M} \sum_{i=1}^{M} \mathcal{O}(x_i) \,. \tag{5.4}$$

All of these estimates for $\mathcal{O}$ will eventually converge to the actual average $\langle \mathcal{O} \rangle_P$ for $M \to \infty$. However, for any finite M, the estimates $\overline{\mathcal{O}}$ are random variables themselves [97]. According to the central limit theorem, they tend to a Gaussian distribution with $\mathbf{Var}(\overline{\mathcal{O}}) \sim M^{-1}$ for $M \to \infty$ [97]. The prefactor of this variance depends on the distribution $Q(x)$ and is in general smaller the more similar $Q(x)$ is to the integrand [97]. It therefore pays of to draw the random sampling points x_i according to $P(x)$. However, *direct sampling* of this distribution is intractable and one usually makes use of Markov chains to generate x_i according to $P(x)$. In comparison to *direct sampling*, this approach has the downside of generating correlated samples. We now introduce some general properties of Markov chains as they form the basis of our algorithm.

5.1 Markov chains

We give a small introduction to Markov processes following the book "Markov Chains and Mixing Times" by Levin and Peres [98]. Proofs of theorems, corollaries and the like as well as instructive examples can be found therein. A Markov chain is a stochastic process that generates a sequence of random variables $(x_0, x_1, \dots)$ of a set Ω [98]. The random variables are chosen based on fixed probabilities T which fulfil the so-called Markov property; that is, the next state $x_{t+1} = y$ of a chain only depends on the current state x_t, but not on the previous states x_i with $i \in \{0, \dots, t-1\}$ [98]. For a finite set Ω, the transition probability T can be written as a matrix with entries $T(x, y) \geq 0$ denoting the probability to proceed from state x to state y [98]. The rows $T(x, \cdot)$ of this matrix are normalised probability distributions [98]

$$\sum_{y \in C} T(x, y) = 1 \,. \tag{5.5}$$

At step t, the current distribution is described by a row vector μ_t with entries $\mu_t(x)$ denoting the probability to be at state $x \in \Omega$ after t steps. The evolution of this distribution can be written with the help of the transition matrix T

$$\mu_{t+1}(y) = \sum_{x \in \Omega} \mu_t(x) T(x, y) \quad \forall y \in \Omega \,. \tag{5.6}$$

In matrix notation this can be written as [98]

$$\mu_t = \mu_{t-1} T = \mu_0 T^t \tag{5.7}$$

with μ_0 denoting the initial distribution. Multiplying the current distribution μ_t at step t from the right with the transition matrix T therefore gives the distribution μ_{t+1} at time step $t+1$. The matrix T^t with the (x, y)-th entry denoted by $T^t(x, y)$ describes the probability to arrive at state y after going t steps starting from state x. One commonly starts with a distribution given by a single definite state x such that

$$\mu_0(y) = \begin{cases} 1 & \text{if } y = x\,, \\ 0 & \text{else.} \end{cases} \tag{5.8}$$

A Markov chain might have special distributions π that are invariant over time, leading to the following definition [98]:

Definition 5.1. *Let T be the transition matrix of a Markov chain. A distribution π satisfying*

$$\pi = \pi T \tag{5.9}$$

*is called **stationary distribution** of the Markov chain.*

We are particularly interested in such stationary distributions as we want our Markov-chain Monte-Carlo algorithm to be equipped with a unique, specific stationary distribution, namely $\pi(x) = P(x)$. Before we address the question about its existence, uniqueness and also convergence, we need to introduce some properties of Markov chains.

Definition 5.2. *Let T be the transition matrix of a Markov chain on a set Ω. This Markov chain is called **irreducible** if*

$$\forall x, y \in \Omega.\ \exists r \in \mathbb{N} : T^r(x, y) > 0\,. \tag{5.10}$$

If a Markov chain is irreducible, it is possible to reach any $y \in \Omega$ independent of the starting position $x \in \Omega$ with a finite amount of steps.

Corollary 5.1. *Let T be the transition matrix of an irreducible Markov chain on a set Ω. Then there exists a unique stationary distribution π with $\pi(x) > 0\ \forall x \in \Omega$.*

The irreducibility condition is not compulsory for the existence of a stationary distribution but it is for the uniqueness and positivity of this distribution [98].

Definition 5.3. *Let T be the transition matrix of a Markov chain on a set Ω and let $\mathcal{T}(x) \coloneqq \{t \geq 1 : T^t(x, x) > 0\}$ denote the times at which the chain can return to a starting point $x \in \Omega$. The Markov chain is called **aperiodic** if the greatest common divisor* $\gcd(\mathcal{T}(x)) = 1\ \forall x \in \Omega$.

The greatest common divisor $\gcd(\mathcal{T}(x))$ is called the period of the state x [98]. If a chain is irreducible, then $\gcd(\mathcal{T}(x)) = \gcd(\mathcal{T}(y))\ \forall x, y \in \Omega$ [98]. We now give a loose version of the convergence theorem [98].

Theorem 5.1. *Let T be a transition matrix of an irreducible, aperiodic Markov chain with stationary distribution π. Then the distribution μ_t will converge to π*

$$\lim_{t\to\infty} \mu_t = \pi \tag{5.11}$$

for any initial distribution μ_0.

For large times t we expect the current distribution μ_t to be a sufficient approximation of π. For details on how to quantify convergence of a distribution we refer to [98].

5.2 Markov-chain Monte Carlo

With the aid of a Markov chain we want to draw samples x_i in a set of configurations $\Omega = C$ according to the probability $P(x)$. If we can manage to construct an irreducible and aperiodic Markov chain on C with a stationary distribution $\pi(x) = P(x)$, the Markov chain provides a sequence of configurations $(y_0, y_1, \dots)$ which are distributed according to $P(x)$.[1] This sequence will therefore serve as our sequence of samples in a Markov-chain Monte-Carlo simulation. The main open question is how one can construct a Markov chain with the desired stationary distribution. From the definition of the stationary distribution (see Definition 5.1) the transition matrix has to fulfil the condition

$$P(x) = \sum_{y\in C} P(y)T(y,x) \tag{5.12}$$

in order for P to be a stationary distribution. By supplementing the left side of Eq. (5.12) with $1 = \sum_{y\in C} T(x,y)$ this yields the *global balance condition*

$$\sum_{y\in C} P(x)T(x,y) = \sum_{y\in C} P(y)T(y,x)\,, \tag{5.13}$$

which means that the total flow into a configuration $y \in \Omega$ has to balance the total flow out of this configuration. Another, stronger condition, is the *detailed balance condition*

$$P(x)T(x,y) = P(y)T(y,x)\,, \tag{5.14}$$

[1] For simplicity, we assume that the distribution of the Markov chain is already sufficiently close to P when the first configuration y_0 is taken. In general one discards the first configurations as those configurations are usually not even close to being distributed according to P. The time a Markov chain requires to get sufficiently close to the stationary distribution is called mixing time. For details on mixing times, see Ref. [98].

which states that the flow from x to y should balance the flow from y to x. It is a microscopic version of the global balance condition and evidently implies its global counterpart. The Markov-chain Monte-Carlo algorithm that we will make use of fulfils the detailed balance condition. However, the global balance condition is a sufficient (and necessary) condition for P to be a stationary distribution. Markov chains that additionally obey the detailed balance condition are called *reversible*.[1] The challenge is to construct transition probabilities such that the Markov chain converges to the desired stationary distribution $P(x)$. We will briefly describe a quite general and established way to construct transition probabilities T from P such that detailed balance is fulfiled, namely the Metropolis-Hastings algorithm.

5.2.1 Metropolis-Hastings algorithm

The Metropolis algorithm was already proposed in 1953 [102] for a specific stationary distribution, namely the Boltzmann distribution, and was the first Markov-chain MC algorithm [74]. It was later generalised by Hastings [103] and the extended version is called Metropolis-Hastings algorithm. The algorithm is still widely used to this day due to its versatility and simplicity.

For the construction of this algorithm, the transition probability is decomposed into

$$T(x, y) = g(x, y)A(x, y) \tag{5.15}$$

with $g(x, y)$ the probability to propose a move from x to y and $A(x, y)$ the acceptance probability of this proposed move. Rejecting moves can tune the transition probabilities such that the desired stationary distribution is obtained. However, this comes at the cost of slowing down the chain and might reduce the statistical efficiency of the algorithm to generate independent samples [96, 98]. When inserting Eq. (5.15) into Eq. (5.14), this yields for the acceptance probabilities

$$\frac{A(x, y)}{A(y, x)} = \frac{P(y)g(y, x)}{P(x)g(x, y)} =: R(x, y) \tag{5.16}$$

with $R(x, y) = R(y, x)^{-1}$. This is for instance solved by

$$A(x, y) = c \min \{1, R(x, y)\} \tag{5.17}$$

with $0 < c \leq 1$. As we want to minimise the rejections of proposed moves, c is chosen to be its maximum value. The Metropolis-Hastings algorithm has acceptance probabilities

$$A_{\mathrm{MH}}(x, y) = \min \{1, R(x, y)\} \ . \tag{5.18}$$

[1] Violation of detailed balance gave rise to efficient MC algorithms [99] and so-called event-chain MC algorithms [100], which can reduce autocorrelation and mixing times by avoiding diffusive behaviour of the chain [101].

One can easily verify that this choice fulfils detailed balance Eq. (5.14). For symmetric proposal probabilities $g(x, y) = g(y, x)$, the Metropolis-Hastings algorithm accepts transitions from configuration x to a configuration y with lower weight with probability $P(y)/P(x)$ while a move to a configuration with higher or equal weight is always accepted.

This algorithm usually comes with relatively local proposed changes [96]. Often, single microscopic degrees of freedom, e. g. single spin flips, are subject to change in an update since proposing too large moves can increase the rejection rate and slow down the chain. Such local schemes suffer from critical slowing down, i. e. the divergence of autocorrelation time close to a continuous phase transtition where the system is correlated on large scales [74]. So-called cluster algorithms can reduce or even avoid this divergence [74, 96] and we will briefly describe a few cluster algorithms related to the algorithm we utilise.

5.2.2 Cluster algorithms

The development of cluster algorithms led to a remarkable breakthrough in terms of simulation of continuous phase transitions [74]. The reason for the superiority of these algorithms lies in the nature of critical phases. Their long-ranged correlations lead to a pattern of large correlated clusters which are hard to disintegrate by local moves [74]. In contrast, collectively updating large subsets of the system can break up this pattern easily [74]. However, the construction of a non-local algorithm is model dependent and for some models no cluster algorithm has been found so far [74]. We will concentrate on the discussion of a few spin-lattice algorithms that are related with the update scheme we make use of.

In 1987, the first cluster algorithm was proposed for the classical Ising model by Swendsen and Wang [104]. It builds up several disconnected clusters of aligned spins at once and every cluster is flipped with probability 1/2 [96].[1] For the construction of the clusters, the algorithm considers every bond of the lattice and activates it with a finite probability if the spins are aligned energetically favourable. Bonds that are energetically unfavourable are never activated. After every bond was inspected, the clusters are formed by the activated bonds. As the algorithm considers every bond, the Swendsen-Wang algorithm scales as $\mathcal{O}(N_b)$ with N_b the amount of bonds on the whole lattice. For the nearest-neighbour model the Swendsen-Wang algorithm is therefore highly efficient scaling as $\mathcal{O}(N)$ with N the amount of sites. However, for models with long-range interactions, where all spins are coupled to each other, the total amount of bonds scales quadratically $N_b \sim N^2$ with the system size. The algorithm

[1] A more efficient single-cluster version was later proposed by Wolff [105]. It builds up a single cluster which is always flipped.

therefore scales as $\mathcal{O}(N^2)$ making it computationally expensive. Luijten and Blöte developed a version for long-range systems scaling as $\mathcal{O}(N \log N)$ [106], which can be further reduced to $\mathcal{O}(N)$ [80]. The speed-up was achieved by the observation that only bonds of the order $\mathcal{O}(N)$ contribute to the cluster, even for long-range interaction [80]. Instead of inspecting all bonds, Luijten and Blöte used a two step procedure in which they first draw bonds according to their weight and only activate them in a second step if they are aligned energetically favourable. They used a binary search in order to draw bonds from a cumulative probability distribution of these bond weights leading to a contribution of $\mathcal{O}(\log N)$ in the algorithm's complexity [80]. By using an $\mathcal{O}(1)$ method such as the Walker's method of alias, the algorithm's complexity can be further reduced to $\mathcal{O}(N)$ [80].

Those algorithms were developed for classical systems,[1] but the QMC method we will use is very similar to the algorithm of Swendsen and Wang for short-range or Luijten and Blöte for long-range interactions [107]. We will also make use of the Walker's method of alias for drawing bonds in order to reduce the comlexity to $\mathcal{O}(N)$. Before we embark on the description of the QMC algorithm of our choice we need to make the quantum problem accessible to MC integration.

5.3 Quantum Monte Carlo

QMC methods differ from MC methods for classical systems as some preliminary work has to be done to rewrite the quantum problem such that it can be simulated with MC. Before we turn to the specific algorithm that we will make use of, it is worthwhile to address this preliminary work to better understand its formulation. In order to make the quantum problem accessible to MC, it is often reformulated as a classical problem with classical degrees of freedom [96]. While for classical systems the partition function as well as thermal averages are already in the form of weighted averages Eq. (5.1) with a known probability weight, the quantum mechanical partition function is given by the trace

$$Z = \mathrm{tr}(e^{-\beta H}) = \sum_{\{|\alpha\rangle\}} \langle\alpha| \, e^{-\beta H} \, |\alpha\rangle \,, \tag{5.19}$$

where $\{|\alpha\rangle\}$ denotes the summation over an arbitrary basis set of the Hilbert space. Knowing the eigenenergies and eigenstates of the underlying Hamiltonian would immediately reduce Eq. (5.19) to the partition function of a classical system. However, knowing the eigenenergies and eigenstates comes down to knowing the solution to a

[1] Fukui and Todo also extended their version to path-integral Monte Carlo [80] and studied the thermal BKT transition of the ferromagnetic LRTFIM in 1d.

quantum problem [96]. Finite-temperature QMC methods like the path integral MC (PIMC), auxiliary-field MC as well as the Stochastic Series expansion (SSE) aim to rewrite the partition function Eq. (5.19)[1] as a sum of probability weights $w(x)$

$$Z = \sum_{x \in C} w(x) \tag{5.20}$$

with a newly introduced configuration space C whose explicit form depends on the formalism used. In order to get a feeling of how this transformation can be conducted, we will briefly describe three common methods.

The PIMC was amongst the earliest QMC methods developed [108] and can be applied to a variety of quantum systems. In analogy to the quantum-to-classical mapping encountered in Sec. 2.2, the formalism maps the quantum system to a classical system with imaginary time using Euclidean path integrals. It was originally developed in discrete imaginary time. However, this introduces a systematic error which had to be taken into account by performing simulations with different discretisation steps and extrapolating to continuous imaginary time. Later, the limit to continuous imaginary time was taken explicitly in the formulation of the algorithm [109].

The SSE formalism is a QMC scheme developed by Sandvik in the 90s [110, 111] as an improvement to an older scheme developed by Handscomb in 1962 [112]. It is based on a Taylor expansion of the partition function in inverse temperature and also introduces an additional discrete dimension that corresponds to imaginary time. However, unlike the discrete PIMC formalism, the SSE method does not have the drawback of being approximate in imaginary time. We will discuss the SSE method in the next chapter in detail as we will use it to simulate the LRTFIM.

The auxiliary-field MC (see e. g. Refs. [113, 114] for review) is noteworthy as it differs from PIMC and SSE in the sense that the configuration space C is not related to the physical system, but sums over auxiliary-field configurations. The physical degrees of freedom are decoupled by means of a Hubbard-Stratonovich transformation whereby auxiliary fields are introduced. The physical degrees of freedom can then be formally integrated out and the configurations in C do not depend on those degrees of freedom anymore. Moreover, it can in some cases circumvent or at least milden a problem that is rather common for QMC methods, namely the occurence of the sign problem. In Sec. 2.2 we already mentioned that in a quantum-classical mapping the resulting "probability"-weights are not non-negative in general. This problem is especially severe for frustrated as well as fermionic systems and poses a great challenge. The occurrence of this problem heavily depends on the algorithm used and it should be avoided

[1] Other QMC methods like the Variational, Projector and Diffusion QMC concentrate on calculating the ground-state wave function instead of the partition function.

whenever possible. In order to demonstrate its severity, we will briefly discuss the sign problem and its consequences.

5.3.1 The sign problem

In general, there is no guarantee that the "weights" $w(x)$ in Eq. (5.20) are non-negative for all configurations $x \in C$. For fermionic models, signs easily arise from their exchange statistics, but also for frustrated models this often poses a problem [115]. Even though this occurrence of negative signs prevents us from using $w(x)$ as a target distribution for sampling the configuration space, it is still possible to perform simulations by instead using its absolute value $|w(x)| = \mathrm{sgn}[w(x)]w(x)$ as the probability distribution sampled by the Markov chain and absorbing the sign into the observables. The observables are then calculated via [115]

$$\begin{aligned} \langle A \rangle_w &= \frac{\sum_{x\in C} A(x)w(x)}{\sum_{x\in C} w(x)} \\ &= \frac{\sum_{x\in C} A(x)\mathrm{sgn}[w(x)]|w(x)|}{\sum_{x\in C} |w(x)|} \cdot \frac{\sum_{x\in C} |w(x)|}{\sum_{x\in C} w(x)} \\ &= \frac{\langle A \cdot \mathrm{sgn}(w) \rangle_{|w|}}{\langle \mathrm{sgn}(w) \rangle_{|w|}}, \end{aligned} \tag{5.21}$$

but this is where the infamous sign problem actually arises. If one uses $|w(x)|$ as probability weights, this comes at the cost of dividing the observable average $\langle A \cdot \mathrm{sgn}(w) \rangle_{|w|}$ by the average sign $\langle \mathrm{sgn}(w) \rangle_{|w|}$ which vanishes exponentially in inverse temperature β and system size N [115]

$$\langle \mathrm{sgn}(w) \rangle_{|w|} = \frac{\sum_{x\in C} w(x)}{\sum_{x\in C} |w(x)|} = \frac{Z_w}{Z_{|w|}} = \frac{e^{-\beta F_w}}{e^{-\beta F_{|w|}}} = e^{-\beta N \Delta f} \tag{5.22}$$

with $Z_{w/|w|}$ and $F_{w/|w|}$ being the partition function and free energy of the original system and an analogue system with non-negative weights respectively. $\Delta f = \frac{1}{N}(F_w - F_{|w|})$ is the difference of the free energy densities.[1] As $\langle \mathrm{sgn}(w) \rangle_{|w|} \leq 1$, it is clear that $\Delta f \geq 0$. This exponentially vanishing behaviour becomes an issue for simulations performed at low temperatures and for large system sizes as the relative error [115]

$$\frac{\delta \mathrm{sgn}}{\langle \mathrm{sgn} \rangle_{|w|}} = \frac{1}{\sqrt{M_{\mathrm{ind}}}} \sqrt{\frac{\langle \mathrm{sgn}^2 \rangle_{|w|} - \langle \mathrm{sgn} \rangle_{|w|}^2}{\langle \mathrm{sgn} \rangle_{|w|}^2}} \sim \frac{1}{\sqrt{M_{\mathrm{ind}} \langle \mathrm{sgn} \rangle_{|w|}^2}} = \frac{e^{\beta N \Delta f}}{\sqrt{M_{\mathrm{ind}}}} \tag{5.23}$$

[1] For fermionic systems where the negative signs are due to the fermionic anticommuation relation, $Z_{|w|}$ is the partition function of the respective bosonic system [115].

diverges exponentially with inverse temperature and system size as the mean sign exponentially goes to zero (Eq. (5.22)). This error propagates to *all* observables, making it necessary to take exponentially more independent samples M_{ind} for large systems and low temperature to achieve the same accuracy. Unfortunately, the regime of interest when investigating criticality of a quantum critical point is the limit $N, \beta \to \infty$.

The sign problem is proven to be **NP**-hard[1] [115] making it unlikely to be solved.[2] However, for a specific model this does not exclude the existence of a QMC formalism with non-negative weights from the beginning. The SSE algorithm we use for the LRTFIM does not suffer from the sign problem even in the presence of frustration. In this thesis this is important in view of the antiferromagnetic long-range model, but this property is also valuable for further models such as the TFIM on the triangular or Kagome lattices which are physically rich and interesting in their own way [9–12, 116]. With this note we want to close the general description of MC and QMC methods and turn to the description of SSE.

[1] Problems of the complexity class **NP**-hard are at least as hard as any problem in **NP**. Solving one **NP**-hard problem amounts to solving all **NP** problems and would imply **P** = **NP**.

[2] Solving here means that one finds an algorithm for a deterministic classical computer which scales polynomially instead of exponentially.

6 Stochastic Series Expansion

The Stochastic Series Expansion (SSE) is a QMC method developed by Anders Sandvik as a generalisation of Handscomb's method [110,111]. It is applicable to lattice systems and is highly efficient, scaling with the system size and the inverse temperature, when the sign problem is absent [59]. This is in general the case for non-frustrated spin and boson systems, but also for some fermion systems as the Hubbard model in 1d [111] and the TFIM on frustrated lattices.[2] In this thesis, the SSE formalism is used to calculate thermal averages of the LRTFIM in 1d and the TFIM in 4d. It is a finite-temperature QMC method.

Handscomb developed one of the first MC methods for quantum systems [112] and, shortly after, successfully applied it to the ferromagnetic Heisenberg model [117]. His method was based on a high-temperature expansion of the partition function Z and thermal expectation values $\langle A \rangle$

$$Z = \mathrm{Tr}\left\{e^{-\beta\mathcal{H}}\right\} = \sum_{n=0}^{\infty} \frac{(-\beta)^n}{n!} \mathrm{Tr}\{\mathcal{H}^n\}\,, \tag{6.1}$$

$$\langle A \rangle = \frac{1}{Z} \mathrm{Tr}\left\{Ae^{-\beta\mathcal{H}}\right\} = \frac{1}{Z} \sum_{n=0}^{\infty} \frac{(-\beta)^n}{n!} \mathrm{Tr}\{A\mathcal{H}^n\}\,. \tag{6.2}$$

The Hamiltonian is decomposed $\mathcal{H} = \sum_i H_i$ into the operators H_i and the product $\mathcal{H}^n$ is expanded into sequences of those operators H_i. However, Handscomb's method requires the analytical evaluation of traces and is therefore not applicable to a wide variety of models. Sandvik opened up new possibilities by further reducing the traces to products of matrix elements of single operators H_i which can be easily evaluated [111].

This section describes Sandvik's method in detail and is structured as follows. We start with the model-independent representation of the partition function in Sec. 6.1 yielding the target distribution of the Markov chain. As the configuration space and updates depend on the specific Hamiltonian considered, we restrict the further discussion on valid configurations and the update scheme in Sec. 6.2 to the LRTFIM. This update scheme is split into a local update (see Sec. 6.2.1) for inserting operators H_i which are diagonal in the computational basis that is chosen for evaluating the trace and

[2] Fermionic systems often pose a bigger challenge as their underlying statistics easily lead to the sign problem making the simulations exponentially hard.

a cluster update (see Sec. 6.2.2) in which off-diagonal operators H_i are inserted. In general, expanding the expectation values Eq. (6.2) by no means needs to generate the same target distribution as the partition function. Nevertheless, the expectation values of all observables we consider can be extracted from the Markov chain constructed by the partition function and we give explicit formulas for calculating those expectation values in Sec. 6.3 with a focus on the order-parameter susceptibility in Sec. 6.3.1 and the correlation function in Sec. 6.3.2. As we want to extract ground-state properties from SSE, which is a finite-temperature QMC method, we address how we assert the convergence to zero temperature in Sec. 6.4. The simulations will provide estimates for observables close to the quantum critical point from which we want to obtain the critical field and critical exponents. We therefore close this chapter with a description of numerical methods by describing two methods for extracting the criticality based on FSS in Sec. 6.5.

6.1 Representation of the partition function

As Handscomb's original method, the SSE method is based on a high-temperature series expansion of the partition function in Eq. (6.1). In contrast to Handscomb's method, the traces are not evaluated analytically, but one chooses a computational basis $\{|\alpha\rangle\}$ in which the trace is evaluated. At this point, the only constraint for the basis is that it has to be orthonormal, but the occurence of the sign problem depends on the basis choice. For instance, for the antiferromagnetic TFIM on non-bipartite lattices, the sign problem occurs when using the field eigenbasis but can be avoided in the eigenbasis of the Ising couplings [59]. As for the method of Handscomb, one splits the Hamiltonian into a finite amount of operators

$$\mathcal{H} = -\sum_{a,b} H_{a,b} \tag{6.3}$$

with the Hamiltonian being sufficiently decomposed in the sense that the individual constituents $H_{a,b}$ fulfil the non-branching property [118]

$$H_{a,b}\,|\beta\rangle \sim |\gamma\rangle \quad \text{with} \quad |\gamma\rangle \in \{|\alpha\rangle\} \quad \forall\,|\beta\rangle \in \{|\alpha\rangle\} \tag{6.4}$$

in the chosen computational basis. As to ensure the positiveness of the resulting probability weights, one may demand all matrix elements of the operators $H_{a,b}$ to be non-negative in the computational basis[1]

$$\langle\beta|\,H_{a,b}\,|\gamma\rangle \geq 0 \qquad \forall\,|\beta\rangle\,,|\gamma\rangle \in \{|\alpha\rangle\}\,. \tag{6.5}$$

[1] This is not a neccessary but sufficient condition for positive probability weights. Signs of negative matrix elements might cancel for every valid configuration if they need to occur an even amount of times. E.g. for the antiferromagnetic TFIM one can choose the field basis as the computational basis on bipartite lattices even though there are negative matrix elements.

Turning back to the partition function and inserting the decomposition of the Hamiltonian as well as the computational basis yields

$$
\begin{aligned}
Z &= \sum_{n=0}^{\infty} \frac{(-\beta)^n}{n!} \operatorname{Tr}\{\mathcal{H}^n\} && (6.6)\\
&= \sum_{n=0}^{\infty} \frac{(-\beta)^n}{n!} \operatorname{Tr}\left\{ \left(-\sum_{a,b} H_{a,b} \right)^n \right\} && (6.7)\\
&= \sum_{n=0}^{\infty} \frac{(-\beta)^n}{n!} \operatorname{Tr}\left\{ (-1)^n \left(\sum_{a,b} H_{a,b} \right)^n \right\} && (6.8)\\
&= \sum_{n=0}^{\infty} \frac{\beta^n}{n!} \sum_{\{|\alpha\rangle\}} \left\langle \alpha \middle| \left(\sum_{a,b} H_{a,b} \right)^n \middle| \alpha \right\rangle . && (6.9)
\end{aligned}
$$

In the next step, one futher expands the powers

$$
\left(\sum_{a,b} H_{a,b} \right)^n = \sum_{\{S_n\}} \prod_{p=0}^{n-1} H_{a_p,b_p} \tag{6.10}
$$

by introducing the ordered sequences $S_n = \{[a_0, b_0], \ldots, [a_{n-1}, b_{n-1}]\}$ with the operator indices $[a_p, b_p]$ and summing over the set $\{S_n\}$ of all sequences corresponding to the sequences of $H_{a,b}$.

Inserting this into Eq. (6.9) finally leads to [107]

$$
\begin{aligned}
Z &= \sum_{n=0}^{\infty} \sum_{\{S_n\}} \sum_{\{|\alpha\rangle\}} \frac{\beta^n}{n!} \left\langle \alpha \middle| \prod_{p=0}^{n-1} H_{a_p,b_p} \middle| \alpha \right\rangle \\
&= \sum_{n=0}^{\infty} \sum_{\{S_n\}} \sum_{\{|\alpha\rangle\}} w(\alpha, S_n) \,,
\end{aligned} \tag{6.11}
$$

arriving at a sum of weights $w(\alpha, S_n)$ over the configuration space

$$
C \coloneqq \{|\alpha\rangle\} \times \bigcup_{n=0}^{\infty} \{S_n\} \tag{6.12}
$$

as desired (see Eq. (5.20)). It is useful to define the normalised states obtained by propagating the basis states $|\alpha\rangle$

$$
|\alpha(p)\rangle \sim \prod_{i=0}^{p-1} H_{a_i,b_i} |\alpha\rangle \tag{6.13}
$$

where $|\alpha(0)\rangle = |\alpha\rangle$ is the initial state and $|\alpha(p)\rangle$ is the normalised propagated state in imaginary time. This propagation direction is referred to as imaginary time as it is closely related to the imaginary time in the PIMC. However, the propagation index p is not a fixed, discrete imaginary-time step but rather a distribution of imaginary times [46, 118]. Just as in the path-integral formalism, the trace in Eq. (6.11) leads to periodic boundary condition $|\alpha(0)\rangle = |\alpha(n)\rangle$ in imaginary time. With the propagated state Eq. (6.13) the weights in Eq. (6.11) can be rewritten

$$Z = \sum_{n=0}^{\infty} \sum_{\{S_n\}} \sum_{\{|\alpha\rangle\}} \frac{\beta^n}{n!} \prod_{p=0}^{n-1} \Big\langle \alpha(p+1) \Big| H_{a_p,b_p} \Big| \alpha(p) \Big\rangle \tag{6.14}$$

as a product of matrix elements of the operators $H_{a,b}$ which are known analytically and will be incorporated into the algorithm.

What is left to do, is to find a Markovian random walk through the configuration space converging to a stationary distribution given by $w(\alpha, S_n)$ and a recipe for actually calculating thermal expectation values given by Eq. (6.2).

6.1.1 Fixed-length scheme

Before constructing the update scheme used for the TFIM in this thesis, we want to modify the configuration space a bit in order to make programming of the Markovian random walk more convenient. Having a fluctuating sequence length n is disadvantageous as it makes the updates cumbersome [46, 118]. It is easier to have a fixed amount of operators and modify every operator of the sequence individually in the update procedure. For this, one cuts the Taylor series at a sufficient length $n = \mathcal{L}$ and extends every sequence S_n of length $n < \mathcal{L}$ with $\mathcal{L} - n$ identities $H_{0,0} = \mathbb{1}$ at random positions in the sequence. This pads all sequences to a common length $\mathcal{L}$. As there are $\binom{\mathcal{L}}{n}$ ways to insert the identities into the sequence, a compensating factor $\frac{[\mathcal{L}-n(S_\mathcal{L})]!n(S_\mathcal{L})!}{\mathcal{L}!}$ is introduced in Eq. (6.11) with $n(S_\mathcal{L})$ denoting the number of non-trivial operators, meaning $H_{a,b} \neq \mathbb{1}$, in the sequence $S_\mathcal{L}$. This results in [46]

$$\begin{aligned} Z &= \sum_{\{S_\mathcal{L}\}} \sum_{\{|\alpha\rangle\}} \frac{\beta^{n(S_\mathcal{L})}[\mathcal{L} - n(S_\mathcal{L})]!}{\mathcal{L}!} \prod_{p=0}^{\mathcal{L}-1} \Big\langle \alpha(p) \Big| H_{a_p,b_p} \Big| \alpha(p-1) \Big\rangle \\ &= \sum_{\{S_\mathcal{L}\}} \sum_{\{|\alpha\rangle\}} w(\alpha, S_\mathcal{L}) \end{aligned} \tag{6.15}$$

where the sum over n is gone and all sequences $S_\mathcal{L}$ have the same length $\mathcal{L}$. The index $[a_p, b_p] = [0, 0]$ corresponding to an identity operator is now an additionally allowed index.

The cutoff $\mathcal{L}$ is adjusted during the equilibration at the beginning of the simulation. After every sweep we check if the current amount of non-trivial operators $n(S_\mathcal{L})$ comes close to the sequence length $\mathcal{L}$. If $\mathcal{L} < 1.4 \cdot n(S_\mathcal{L})$ the sequence length is set to $\mathcal{L} = 1.4 \cdot n(S_\mathcal{L})$ by extending the sequence with trivial operators. Every time the length $\mathcal{L}$ is adapted, the equilibration-step counter is reset in order to let $\mathcal{L}$ converge and a decent amount of equilibration steps at the final length is conducted before starting the sampling. The error due to this truncation is exponentially small [46, 59].

6.2 Configurations and updates for the TFIM

The model of interest in this thesis is the LRTFIM

$$\begin{aligned} \mathcal{H} &= \sum_{i,j} J_{ij} \sigma_i^z \sigma_j^z - h \sum_i \sigma_i^x \,, \\ J_{ij} &= \frac{J}{2} \frac{1}{|\boldsymbol{r}_j - \boldsymbol{r}_i|^\alpha} \end{aligned} \tag{6.16}$$

with $i, j \in \{1, \ldots, N\}$ indexing the $N = L^d$ sites of the system. We follow the scheme proposed by Sandvik [107] for the TFIM with arbitrary Ising couplings J_{ij}. The computational basis is chosen to be $\{|\alpha\rangle\} = \{|\sigma_1^z, \cdots, \sigma_N^z\rangle\}$ as one can avoid the sign problem in this basis, even for long-range and frustrated interactions, in contrast to the field eigenbasis [59]. The Hamiltonian is written as

$$\mathcal{H} = -\sum_{i=1}^{N} \sum_{j=0}^{N} H_{i,j} + C \tag{6.17}$$

with the following operators fulfilling Eq. (6.4) and Eq. (6.5)

$$H_{0,0} = \mathbb{1} \qquad [0,0] \tag{6.18}$$

$$H_{i,0} = h\sigma_i^x = h(\sigma_i^+ + \sigma_i^-) \qquad [i,0] \tag{6.19}$$

$$H_{i,i} = h\mathbb{1} \qquad [i,i] \tag{6.20}$$

$$H_{i,j} = |J_{ij}| - J_{ij}\sigma_i^z\sigma_j^z \qquad i \neq j \qquad [i,j] \tag{6.21}$$

where $i, j \in \{1, \ldots, N\}$. The insignificant constant C compensates for the constants added to the Ising operators $H_{i,j}$ as well as the additional diagonal operators $H_{i,i}$. The latter will be used to insert the respective counterparts $H_{i,0}$ in an off-diagonal update. The Ising operators Eq. (6.21) are shifted by $|J_{ij}|$ to ensure the matrix elements $\left\langle \sigma_i^z(p+1)\sigma_j^z(p+1) \middle| H_{i,j} \middle| \sigma_i^z(p)\sigma_j^z(p) \right\rangle$ to be non-negative. If the spins at site i and j are aligned energetically favourable, this matrix element takes the value $2|J_{ij}|$ and otherwise vanishes leading to a configuration with total vanishing weight $w(\alpha, S_\mathcal{L})$.

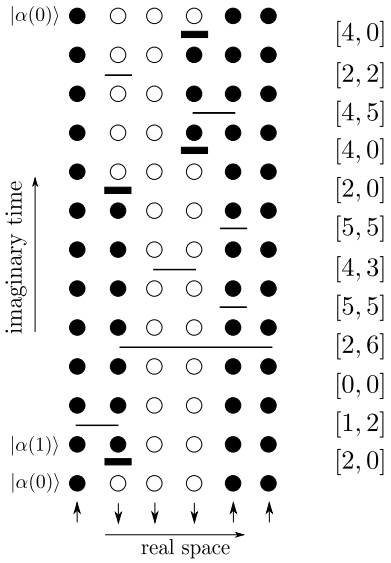

Figure 6.1: *Illustration of a valid configuration with non-vanishing weight for the ferromagnetic LRTFIM with 6 spins and in 1d. Solid circles represent spins pointing up while open circles represent spins pointing down. The thick bars denote spin-flip operators $H_{i,0} = h\sigma_i^x$ while the thin bars at single sites display the constants $H_{i,i} = h\mathbb{1}$. The Ising operators $H_{i,j}$ are illustrated by thin lines connecting two spins of the same orientation. On the right the operator sequence in imaginary time is shown with the respective operator indices.*

Ising bonds among pairs of spins that are not aligned energytically favourable are therefore forbidden. The operator $H_{0,0}$ does not appear in the Hamiltonian but was introduced to the sequence by virtue of the fixed-length scheme.

In Fig. 6.1 an SSE configuration is illustrated with solid and empty circles representing spin up and down respectively. The horizontal direction is the direction in real space while the vertical direction corresponds to the propagation or imaginary-time direction. The sequence of operators acting on the states $|\alpha(p)\rangle$ is given by the list of indices on the right. It is sufficient to store the index sequence as well as the initial state $|\alpha(0)\rangle$ in the simulation as one can propagate the states according to Eq. (6.13).

For an update of the configuration, the operator sequence as well as the initial state have to be updated. One MC step consists of two updates; First a diagonal update is performed which replaces the identities Eq. (6.18) with Ising bonds Eq. (6.21) and constant field operators Eq. (6.20) and vice versa

$$[0,0] \longleftrightarrow [i,j] \qquad i,j \neq 0\,. \tag{6.22}$$

As only diagonal operators are exchanged, this update is termed diagonal update. In a second step, one replaces the constant field operators Eq. (6.20) with the spin-flip operators Eq. (6.19) and the other way around

$$[i,i] \longleftrightarrow [i,0] \qquad i \neq 0\,, \tag{6.23}$$

thereby flipping intermediate spins in the states $|\alpha(p)\rangle$, including the initial state $|\alpha(0)\rangle$. There are two schemes for this off-diagonal update described in Ref. [107], one local and one cluster update. As the cluster update performs better than the local update close to the critical point [59, 107], we will restrict our discussion on the cluster update. The local update procedure was implemented but not used in the final simulations.

6.2.1 Diagonal update

We start with the diagonal update in which the number of non-trivial operators n is altered. In this update, the non-trivial diagonal operators are replaced with identity operators and the other way around. This is conducted at every propagation step $p \in \{0, \ldots, \mathcal{L}-1\}$. Starting at the initial state $|\alpha(0)\rangle$ and propagation step $p = 0$, one runs over the whole imaginary-time sequence step-by-step. As one needs to know the instantaneous state $|\alpha(p)\rangle$ for possibly inserting a bond operator at propagation step p, the state is propagated in imaginary time along the way. Assume we are currently at step p and have propagated the initial state up to $|\alpha(p)\rangle$ during the diagonal update of the preceeding imaginary-time steps. If the operator H_{a_p,b_p} at step p is off-diagonal, one calculates $|\alpha(p+1)\rangle = H_{a_p,b_p}\,|\alpha(p)\rangle$ and proceeds with step $p+1$. However, if the operator H_{a_p,b_p} is diagonal (meaning $\mathbb{1}$, an Ising bond or a constant field operator), one attempts to update it. If $H_{a_p,b_p} = \mathbb{1}$, one can try to insert a non-trivial diagonal operator $[i,j]$ with $i,j \in \{1,\ldots,N\}$. In Fig. 6.2 possible scenarios for such an update at step p are depicted. Instead of drawing a candidate operator uniformly and rejecting it according to its weight, it is beneficial to sample the operator probability distribution *directly* and draw the bonds according to their weight.

An operator $[i,j]_p$ with $i,j \neq 0$ gets proposed with the probability

$$g([0,0]_p \to [i,j]_p) = \frac{M_{ij}}{\mathcal{C}} \tag{6.24}$$

with the matrix element M_{ij} and the normalising constant C

$$M_{ij} = \begin{cases} 2|J_{ij}| & \text{for } i \neq j\,, \\ h & \text{for } i = j\,, \end{cases} \tag{6.25}$$

$$\mathcal{C} = Nh + 2\sum_{j\neq i} |J_{ij}|\,. \tag{6.26}$$

On the contrary, if H_{a_p,b_p} is a non-trivial diagonal operator we always propose the move to replace this operator $[i,j]_p$ with $[0,0]_p$

$$g([i,j]_p \to [0,0]_p) = 1\,. \tag{6.27}$$

The acceptance ratio is chosen according to Metropolis-Hastings (see Eq. (5.18)). For the constant field operator $[i,i]$ as a candidate, this yields the acceptance probability

$$\begin{aligned} A([0,0]_p \to [i,i]_p) &= \min\left(1, \frac{\beta M_{ii}}{\mathcal{L}-n}\frac{\mathcal{C}}{M_{ii}}\right) \\ &= \min\left(1, \frac{\beta(Nh + 2\sum_{j\neq i}|J_{ij}|)}{\mathcal{L}-n}\right) \end{aligned} \tag{6.28}$$

with the factor

$$\frac{\beta M_{ii}}{\mathcal{L}-n} = \frac{\beta^{n+1}[\mathcal{L}-(n+1)]!}{\beta^n[\mathcal{L}-n]!}M_{ii} \tag{6.29}$$

coming from the change in weight of the configuration. Analogously, for the acceptance probability of a candidate bond $[i,j]$ with $j \neq i$, this yields the same acceptance probability

$$\begin{aligned} A([0,0]_p \to [i,j\neq i]_p) &= \delta_{\pm\sigma_i^z,\sigma_j^z} A([0,0]_p \to [i,i]_p) \\ &= \delta_{\pm\sigma_i^z,\sigma_j^z} \min\left(1, \frac{\beta(Nh + 2\sum_{j\neq i}|J_{ij}|)}{\mathcal{L}-n}\right) \end{aligned} \tag{6.30}$$

up to a factor $\delta_{\pm\sigma_i^z,\sigma_j^z}$ with " $+$ " for ferromagnetic and " $-$ " for antiferromagnetic coupling. This factor ensures that when attempting to insert a bond, the move is always rejected if σ_i^z and σ_j^z are not aligned in an energetically favourable way as the resulting matrix element and configuration weight would vanish. For the reversed acceptance ratio one finds

$$A([i,j]_p \to [0,0]_p) = \min\left(1, \frac{\mathcal{L}-(n-1)}{\beta(Nh + 2\sum_{j\neq i}|J_{ij}|)}\right)\,. \tag{6.31}$$

After possibly accepting or rejecting the proposed move, one proceeds with step $p+1$.

What we have not yet addressed is how to perform *direct sampling* of the proposal probabilities Eq. (6.24). Due to the translational invariance of M_{ij}, it is sufficient to draw the first index i uniformly distributed and only draw the second index j according to the relative weights M_{ij} for fixed i. In Ref. [107] a binary search of the cumulative probability distribution was used which can be conducted in $\mathcal{O}(\log N)$ operations. We instead follow Refs. [59, 80] and make use of Walker's method of alias which is able to draw integer random numbers from a discrete probability distribution in constant time.

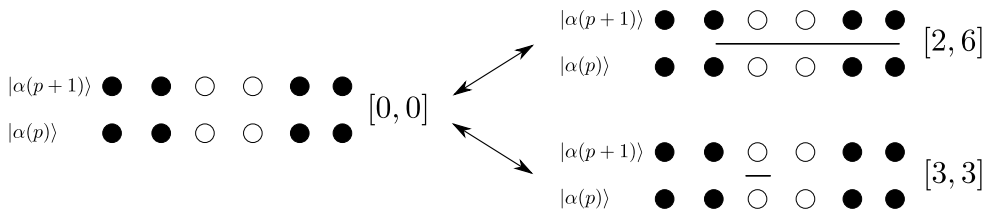

Figure 6.2: *Examples of diagonal updates at propagation step p. Top: Identity gets replaced by an Ising bond between site 2 and site 6 or vice versa. Bottom: Identity gets replaced by a constant field operator at site 3 or vice versa. For a full diagonal update such replacements are proposed for every propagation step and are accepted according to their respective weight.*

Walker's method of alias: Let q_j be a discrete probability distribution.[1] The key idea of Walker's method is to redistribute the unbalanced part of the probability distribution (glimpse Fig. 6.3 for a vague idea). The naive approach would be to draw an integer j uniformly and accept it with probability $\frac{q_j}{\max_j(q_j)}$ [80]. However, this leads to $\mathcal{O}(N)$ steps until a proposed move eventually gets accepted [80]. In the Walker's method one draws the integer j uniformly, possibly accepts it with a probability P_j and otherwise chooses its alias A_j. One therefore succeeds after one try. The probabilities P_j and the aliases A_j need to be determined in advance such that the correct distribution q_j is sampled. In Ref. [80] an algorithm to set up the tables for P_j and A_j with complexity $\mathcal{O}(N)$ is given. Note that the construction of the tables needs to be conducted only once before the actual simulation is performed. During the simulation we only draw from q_j with the help of the precalculated P_j and A_j in $\mathcal{O}(1)$ time. The Walker's method therefore does not alter the complexity of the whole algorithm.

In Fig. 6.3 we illustrate the algorithm by Fukui and Todo [80] to set up the tables P_j and A_j for an examplary distribution. The algorithm proceeds as follows. One starts by setting P_j to a preliminary distribution $P_j = Nq_j$ and creates an empty alias table A_j. The table P_j is split into $P_j \geq 1$ and $P_j < 1$ (see Fig. 6.3b)). The elements of the partition $P_j < 1$ get filled up by the elements $P_j \geq 1$. Starting from the outermost right elements of both parts in Fig. 6.3b) one fills up the shortfall $1 - P_j$ (green blocks in Fig. 6.3) of weight P_j and sets the alias A_j to the number corresponding to the weight left from the separating line of the partitions ($j = 5$ and $A_j = 6$ in Fig. 6.3b)). This alias is later chosen with probability $1 - P_j$ if j gets drawn. In order to compensate for this, one cuts the weight P_{A_j} of the alias by $1 - P_j$ (red blocks in Fig. 6.3). If the new weight P_{A_j} falls below 1, it is transferred to the partition with $P_j < 1$ (see e. g. $j = 6$

[1] In our case $q_j = g([0,0]_p \to [i,j]_p) = \frac{M_{ij}}{\mathcal{C}}$ for a fixed i.

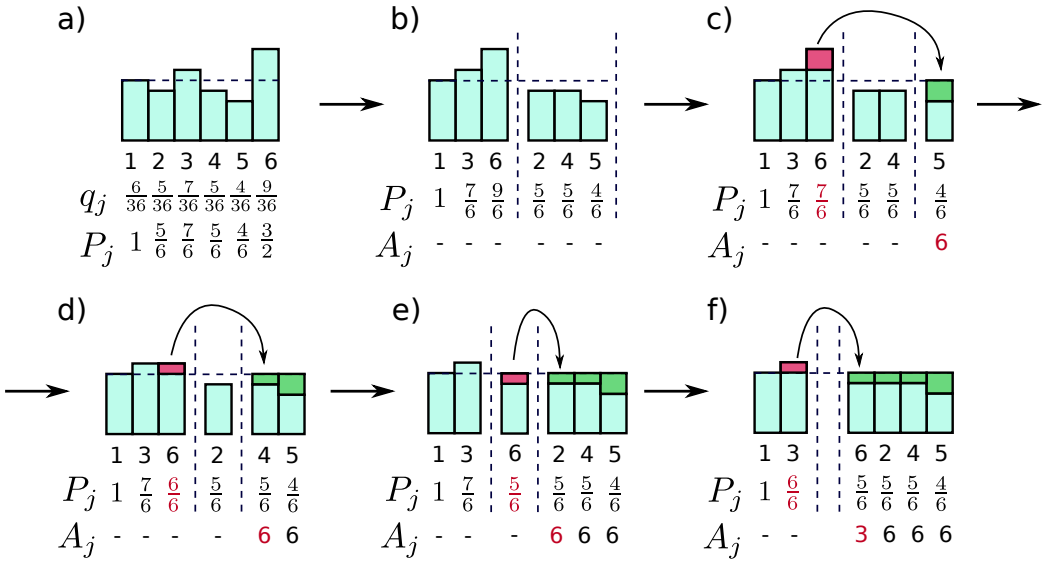

Figure 6.3: *Illustration of Walker's method. The horizontal dashed line corresponds to the mean of the probability distribution q_j with $j \in \{1, \ldots, N\}$. In the first step one defines a tentative probability $P_j = Nq_j$ which compares the probabilities q_j with their mean $\overline{q} = 1/N$. In the second step one discards q_j, creates a table A_j for the aliases and splits the distribution into $P_j \geq 1$ and $P_j < 1$. One then gradually redistributes the weights of P_j by creating aliases until the distribution is flattened. The weights that are taken away are depicted with red bars and the added weights with green bars. The values of P_j and A_j that get modified during a step are written in red. At the right part of the distributions, the weights which are already filled up are gathered. In the middle part of the distribution there are the weights which still need to be filled and the left part contains all weights that are at least full from the beginning. If the middle part is empty, we are done with the redistribution.*

in Fig. 6.3e)-d)). This filling up of the shortfalls is performed as long as the partition $P_j < 1$ is not empty. Fig. 6.3f) therefore shows the last step.

For drawing j corresponding to its original weight q_j, one draws a candidate k for j uniformly in $\{1, \ldots, N\}$ and a uniform number $u \in [0, 1]$. If $u < P_k$ then $j = k$ and otherwise $j = A_k$. The original distribution is recovered by this procedure because [80]

$$q_j = \frac{1}{N}\left[P_j + \sum_i \delta_{jA_i}(1 - P_i)\right], \tag{6.32}$$

where the sum adds up all the contributions coming from weights that got filled up by j and for which the alias were therefore set to $A_i = j$.

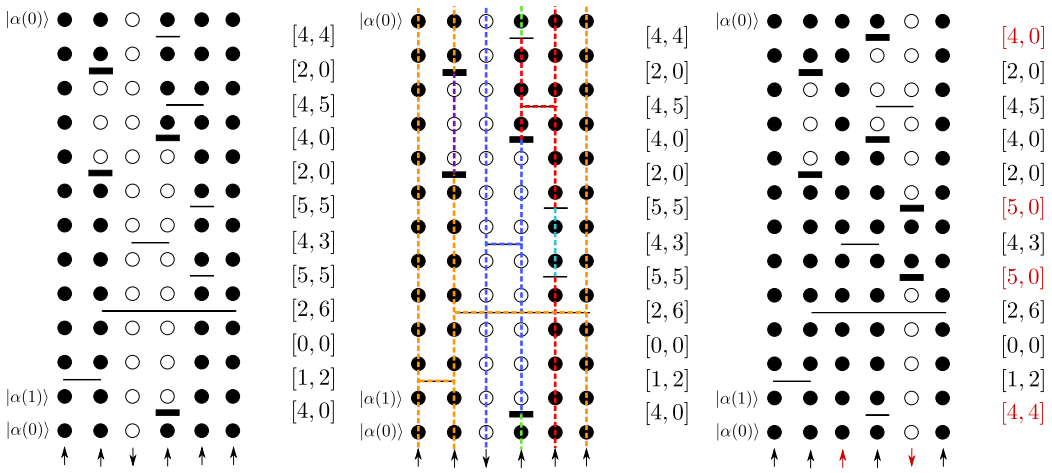

Figure 6.4: *Off-diagonal multicluster update. The left hand side shows the configuration before the clusters are build up. In the middle the disjoint clusters are illustrated with different colours and on the right hand side two random clusters (red and blue) are flipped. The operators as well as the spins in $|\alpha(0)\rangle$ which were altered by the inversion of the clusters are drawn in red.*

6.2.2 Off-diagonal update

For the off-diagonal update we use the cluster version of Ref. [107]. This update substitutes the artificially introduced constant field operators with spin-flip operators and vice versa. The constant field operators were solely introduced for conveniently inserting spin-flip operators. This cluster algorithm does not affect the weight as the constant field and spin-flip operators contribute equally to the weight of a configuration as the respective matrix elements both yield a factor of h. In Fig. 6.4 one can get a first impression of a possible cluster update.

The clusters should be irregularly shaped in space and imaginary time as we want to flip only a limited amount of spins at different sites i and propagation steps p [107]. The spin states at each site are constant between two non-trivial operators in imaginary time acting on this site. A branch of a cluster therefore spreads freely in imaginary time until it encounters a non-trivial operator at the site of this branch. The non-trivial operators in the sequence therefore constitute the vertices of the clusters. The spins attached to the vertices are called legs such that the Ising bonds are 4-leg vertices while the constant field and spin-flip operator are 2-leg vertices. In Fig. 6.5 all the vertices are shown together with the cluster's branching behaviour specifying the spins that will get inverted. An ingoing red arrow denotes the entrance leg where a cluster branch enters the vertex. The outgoing arrows depict new cluster branches. If the cluster branch encounters an Ising vertex, it needs to branch out to the other legs of the vertex (see

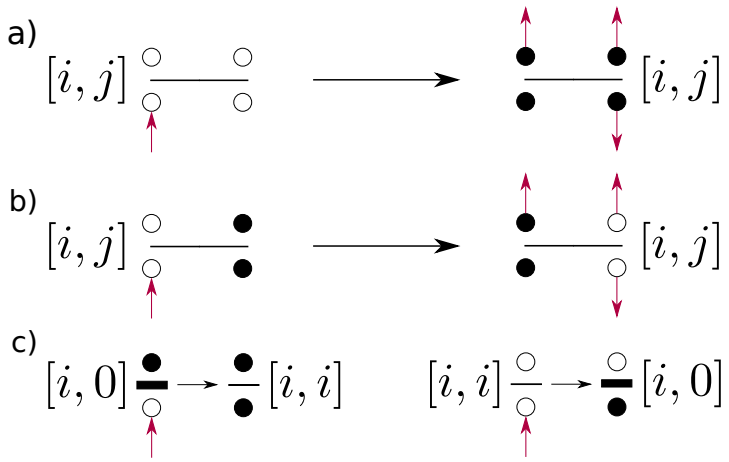

Figure 6.5: *Branching at vertices constituted by the non-trivial operators appearing in a valid configuration. The entrance legs are illustrated by an ingoing red arrow while the exiting legs have an outgoing red arrow. a) Ising vertices for ferromagnetic interactions. b) Ising vertices for antiferromagnetic interactions. The cluster branches out along all legs of the Ising vertices while flipping all its spins. c) Constant-field operator or spin-flip operator limit the cluster in imaginary-time direction. The spin of the entrance leg is flipped and the operator is replaced with its respective counterpart.*

Fig. 6.5a-b)) as the matrix element of an Ising operator is only non-zero if the relative orientation of the legs is conserved; meaning, all legs aligned in the ferromagnetic case and anti-aligned legs at different sites in the antiferromagnetic case. If the branch of a cluster encounters a constant field or spin-flip operator, one can cut the branch there by replacing this operator with its respective counterpart ($[i,i] \leftrightarrow [i,0]$, see Fig. 6.5c)). Note that this branching behaviour leads to a deterministic construction of the clusters for a given operator sequence $S_{\mathcal{L}}$ [107].

This update can either be performed as a single-cluster update (Wolff-type) or a multi-cluster update (Swendsen-Wang-type). Both schemes become equivalent to their classical analogon for $h = 0$ [107]. As the cluster construction is deterministic, it is unprofitable to perform several single-cluster updates as it is very likely to flip the same clusters several times [107]. We will therefore use the multi-cluster update in which one can construct all clusters and flip them with probability 1/2. This update scheme is also the one depicted in Fig. 6.4.

The cluster construction proceeds as follows. Before building a cluster, one randomly decides with probability 1/2 if the cluster should be flipped or not in order to possibly flip the cluster already during the process of its construction. Even if the cluster is not to be flipped, one needs to construct the whole cluster either way and mark all legs as visited in order to not use them as a starting point of another cluster. One then chooses

a leg of a non-trivial operator as a starting leg and puts it onto a stack of unprocessed legs. Depending on the vertex type of the corresponding non-trivial operator one either adds all the other legs onto the stack of unprocessed legs (Ising vertex) or one cuts the branch (constant field or spin-flip vertex). In the latter case one needs to replace the operator with its respective counterpart (see Fig. 6.5c)) if the cluster was decided to be flipped. Taking a leg from the stack, one follows the leg in imaginary time until the next non-trivial operator is encountered and processed by possibly adding other legs to the stack according to the branching rules in Fig. 6.5. If one traverses the boundary in imaginary time, one needs to update the state $|\alpha(0)\rangle$ accordingly if the cluster is to be flipped. One then proceeds with the stack of unprocessed legs as long as it is not empty.

To efficiently construct the cluster in the off-diagonal update, some preliminary work has to be done. Searching for the next non-trivial operator for a certain cluster branch during the construction of the cluster is inefficient. It is beneficial to store the information of the imaginary-time links between different legs of non-trivial operators in a doubly-linked list.

Doubly-linked vertex list and ghost legs: The doubly-linked vertex list comes in handy for advancing to the next non-trivial operator along the imaginary-time direction at the site of the current cluster branch [119]. This list links the legs of the non-trivial operators to the corresponding legs of the previous and following non-trivial operator at the specific site of the leg. For this, the legs are enumerated along the imaginary time. Every leg is connected to a certain vertex at a specific propagation index. This information which maps a leg to its associated vertex is required for the branching when entering a vertex and in principal needs to be stored in another data structure [59]. However, this additional data structure can be avoided if all the vertices have the same amount of legs [59]. In our case, this can be achieved by introducing two additional legs to the constant field and spin-flip operators such that every non-trivial operator has 4 legs. These additional legs are termed *ghost legs* [59]. They are not connected to any other leg and do not take part in the cluster construction. The non-trivial propagation steps $p_{\mathrm{nt}} \in \{0, \ldots, n-1\}$ (i. e. the propagation index only numbering the non-trivial operators without the filling identities) then corresponds to the vertex with legs $l_i = 4p_{\mathrm{nt}} + i$ with $i \in \{0, 1, 2, 3\}$. Vice versa, one can calculate the corresponding non-trivial propagation step by $p_{\mathrm{nt}} = \lfloor l_i/4 \rfloor$ [59].

The doubly-linked vertex list as well as a list mapping the non-trivial operator position p_{nt} to the respective propagation index p has to be calculated after every diagonal update before the off-diagonal update is performed. An example of the enumeration of vertex legs and the links among them is illustrated in Fig. 6.6 with the resulting doubly-linked vertex list in Tab. 6.1 and the list mapping the non-trivial propagation index to the regular propagation index in Tab. 6.2. During the update, processed legs

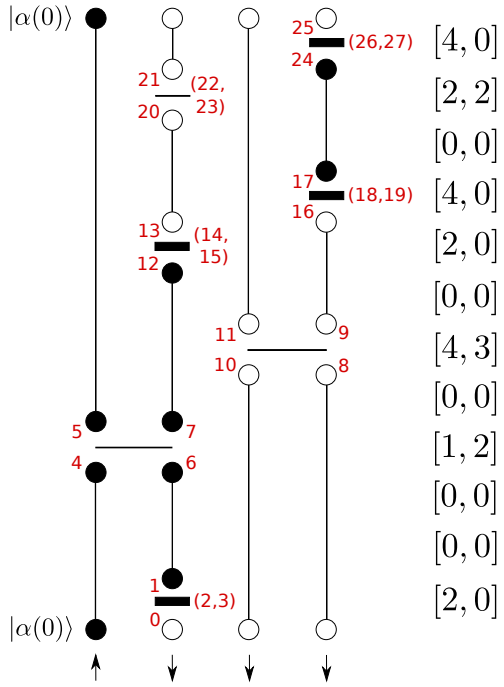

Figure 6.6: *Illustration of the vertex links via legs. The legs are enumerated along imaginary time with their number written in red next to the respective leg. Every vertex is padded to have 4 legs and the arising ghost legs are written in braces (m, n) at their corresponding vertex.*

Table 6.1: *Doubly linked vertex list for the examplary configuration shown in Fig. 6.6. Dead links of ghost legs are set to -1.*

leg	0	1	2	3	4	5	6	7	8	9	10	11	12	13
link	21	6	-1	-1	5	4	1	12	25	16	11	10	7	20
leg	14	15	16	17	18	19	20	21	22	23	24	25	26	27
link	-1	-1	9	24	-1	-1	13	0	-1	-1	17	8	-1	-1

Table 6.2: *Mapping of the non-trivial propagation index p_{nt} to the regular propagation index p of the sequence corresponding to the configuration depicted in Fig. 6.6. The configuration has a sequence length of $\mathcal{L} = 12$ and amount of non-trivial operators $n = 7$.*

p_{nt}	0	1	2	3	4	5	6
p	0	3	5	7	8	10	11

are marked by setting the link to -1 in order to avoid an endless cycle during the cluster construction. After a full multi-cluster update, all links are deleted and the doubly-linked vertex list is recycled for the next update. The links can already be set during the diagonal update by memorising the last encountered non-trivial operator at every site while propagating through imaginary time. After every local diagonal update at propagation step p resulting in a non-trivial operator, one links its lower legs to the legs of the last encountered non-trivial operator at the respective site. A detailed implementation can be found in Ref. [119].

Note that the leg numbers also convey information on when a cluster branch winds around the imaginary-time boundary. If the current leg has an uneven number, its cluster branch flows in positive imaginary-time direction. If the link of this leg has a lower number than the current leg, the branch winds around the imaginary-time boundary. Analogously, for an even leg number with a link having a greater number, the cluster winds in the other direction around the boundary.

6.3 Implementation of observables

We are actually not interested in calculating the partition function itself but expectation values of observables. Thermal expectation values can be expanded into a high-temperature series

$$\langle A \rangle = \frac{1}{Z} \sum_{\{|\alpha\rangle\}} \sum_{n=0} \sum_{S_n} \frac{(-\beta)^n}{n!} \langle \alpha | A \prod_{i=1}^{n} H_{l_i} | \alpha \rangle \tag{6.33}$$

just as the partition function was expanded for the SSE formalism. Note that configurations with a non-vanishing weight $w(\alpha, S_n)$ constituting the partition function do not necessarily contribute to the expectation value $\langle A \rangle$ with the same weight or a non-vanishing weight at all [46]. Only for operators A diagonal in the computational basis $\{|\alpha\rangle\}$, the expectation value can be written as

$$\langle A \rangle = \frac{1}{Z} \sum_{\{|\alpha\rangle\}} \sum_{n=0} \sum_{S_n} A(\alpha) w(\alpha, S_n) \tag{6.34}$$

with $A(\alpha) = \langle \alpha | A | \alpha \rangle$. For instance, the magnetisation or squared magnetisation are such diagonal operators. One can further improve the statistics of the MC estimates by realising that [111]

$$w(\alpha, S_n) = w(\alpha(p), S_n(p)) \tag{6.35}$$

with $S_n(p)$ being the sequence obtained from cyclically permuting S_n for p times [111]. This means that the expectation value Eq. (6.34) can be expressed as

$$\langle A \rangle = \frac{1}{Z} \sum_{\{|\alpha\rangle\}} \sum_{n=0} \sum_{S_n} \frac{1}{n} \sum_{p=0}^{n-1} A(\alpha(p)) w(\alpha, S_n) \tag{6.36}$$

where $A(\alpha)$ is additionally averaged over imaginary time with $A(\alpha(p)) = \langle \alpha(p)|A|\alpha(p)\rangle$.

For off-diagonal operators one needs to find customised formulas for the expectation values. Some of those expectation values are accessible in a quite general way. For instance, one can show that the mean energy has a rather simple formula [110, 111, 118]

$$\langle \mathcal{H} \rangle = -\frac{\langle n \rangle}{\beta} \,. \tag{6.37}$$

Moreover, for the operators $H_{a,b}$ in which the Hamiltonian was decomposed (see Eq. (6.3)) one finds [110, 111, 118]

$$\langle H_{a,b} \rangle = -\frac{\langle n_{a,b} \rangle}{\beta} \tag{6.38}$$

where $n_{a,b}$ is the amount of operators $H_{a,b}$ occuring in the operator sequence. Similarly, one can derive a formula for the heat capacity [110, 111, 118]

$$C = \langle n(n-1) \rangle - \langle n \rangle^2 \tag{6.39}$$

$$= \left\langle n^2 \right\rangle - \langle n \rangle^2 - \langle n \rangle \,. \tag{6.40}$$

However, for small temperatures the heat capacity is calculated as the small difference of large numbers and becomes numerically imprecise.

6.3.1 Susceptibility

We also measure the order-parameter susceptibility for calculating the exponent γ. This susceptibility was already encountered in Sec. 3.4 in the form of an imaginary-time integral

$$\chi = L \int_0^\beta \langle m(\tau) m(0) \rangle \, \mathrm{d}\tau \,. \tag{6.41}$$

The imaginary-time correlation function can also be expanded analogous to the partition function

$$\langle m(\tau)m(0)\rangle = \frac{1}{Z}\,\mathrm{Tr}\Big(e^{-\beta\mathcal{H}}e^{\tau\mathcal{H}}me^{-\tau\mathcal{H}}m\Big) \tag{6.42}$$

$$= \frac{1}{Z}\sum_{\{|\alpha\rangle\}}\left\langle\alpha\middle|\sum_{k=0}^{\infty}\left(\frac{(\beta-\tau)^k}{k!}(-\mathcal{H})^k\right)m\sum_{l=0}^{\infty}\left(\frac{\tau^l}{l!}(-\mathcal{H})^l\right)m\middle|\alpha\right\rangle \tag{6.43}$$

$$= \frac{1}{Z}\sum_{\{|\alpha\rangle\}}\sum_{l,k=0}^{\infty}\frac{(\beta-\tau)^k}{k!}\frac{\tau^l}{l!}\left\langle\alpha\middle|(-\mathcal{H})^k m(-\mathcal{H})^l m\middle|\alpha\right\rangle . \tag{6.44}$$

As the magnetisation is diagonal in the computational basis $\{|\alpha\rangle\}$ we can just replace the operators m by their eigenvalues $m_p \coloneqq m(\alpha(p))$ at a state $|\alpha(p)\rangle$:

$$\langle m(\tau)m(0)\rangle = \frac{1}{Z}\sum_{\{|\alpha\rangle\}}\sum_{l,k=0}^{\infty}\frac{(\beta-\tau)^k}{k!}\frac{\tau^l}{l!}m_l m_0\left\langle\alpha\middle|(-\mathcal{H})^{l+k}\middle|\alpha\right\rangle . \tag{6.45}$$

By replacing the sum over k by a sum over $n \coloneqq l+k$ and inserting the chosen decomposition of the Hamiltonian this further yields

$$\langle m(\tau)m(0)\rangle = \frac{1}{Z}\sum_{\{|\alpha\rangle\}}\sum_{n=0}^{\infty}\sum_{l=0}^{n}\sum_{S_n}\frac{(\beta-\tau)^{n-l}}{(n-l)!}\frac{\tau^l}{l!}m_l m_0\left\langle\alpha\middle|\prod_{i=0}^{n-1}H_{a_i,b_i}\middle|\alpha\right\rangle \tag{6.46}$$

$$= \frac{1}{Z}\sum_{\{|\alpha\rangle\}}\sum_{n=0}^{\infty}\sum_{l=0}^{n}\sum_{S_n}\frac{(\beta-\tau)^{n-l}}{(n-l)!}\frac{\tau^l}{l!}m_l m_0\frac{n!}{\beta^n}w(\alpha,S_n) \tag{6.47}$$

$$= \frac{1}{Z}\sum_{\{|\alpha\rangle\}}\sum_{n=0}^{\infty}\sum_{l=0}^{n}\sum_{S_n}\frac{n!}{(n-l)!l!}\left(1-\frac{\tau}{\beta}\right)^{n-l}\left(\frac{\tau}{\beta}\right)^l m_l m_0 w(\alpha,S_n) \tag{6.48}$$

$$= \frac{1}{Z}\sum_{\{|\alpha\rangle\}}\sum_{n=0}^{\infty}\sum_{l=0}^{n}\sum_{S_n}\binom{n}{l}\left(1-\frac{\tau}{\beta}\right)^{n-l}\left(\frac{\tau}{\beta}\right)^l w(\alpha,S_n)\frac{1}{n}\sum_{p=0}^{n-1}m_{p+l}m_p\,, \tag{6.49}$$

where in the last step we again averaged over imaginary time steps p in order to improve the statistics. Eq. (6.49) also elucidates the connection between the discrete propagation steps of SSE and continuous imaginary time τ [118]. An imaginary time separation τ corresponds to a binomial distribution of separations l of SSE propagation steps

$$B(l|\tau,n) = \binom{n}{l}\left(1-\frac{\tau}{\beta}\right)^{n-l}\left(\frac{\tau}{\beta}\right)^l \tag{6.50}$$

which is peaked around $l = n\tau/\beta$ [118]. If one is interested in the spectral properties of the system, one can use this formula for sampling imaginary-time correlation functions

$\langle A(\tau)B(0)\rangle$ with A, B being operators diagonal in the computational basis by replacing $m_l \to A_l$ and $m_0 \to B_0$ in Eq. (6.49). However, there are more efficient ways to calculate imaginary-time correlation functions by embedding the SSE configuration into continuous imaginary time. We refer to Refs. [59,120] for details. In this thesis, we are only interested in the static properties of the LRTFIM and perform the integration over imaginary time of Eq. (6.49). The occurring integral can be analytically calculated

$$\int_0^\beta \mathrm{d}\tau \left(1-\frac{\tau}{\beta}\right)^{n-l}\left(\frac{\tau}{\beta}\right)^{l} = \beta\int_0^1 \mathrm{d}u\,(1-u)^{n-l}\,u^l \tag{6.51}$$

$$= \beta\frac{(n-l)!}{n!}l!\int_0^1 \mathrm{d}u\,(1-u)^{n} \tag{6.52}$$

$$= \beta\frac{(n-l)!}{n!}l!\frac{1}{n+1} \tag{6.53}$$

by performing l partial integrations. Inserting Eq. (6.49) into the formula of the susceptibility Eq. (6.41) and performing the imaginary time integral Eq. (6.53) this yields

$$\chi = \frac{L}{Z}\sum_{\{|\alpha\rangle\}}\sum_{n=0}^{\infty}\sum_{S_n} w(\alpha,S_n)\frac{\beta}{n(n+1)}\sum_{l=0}^{n}\sum_{p=0}^{n-1} m_{p+l}m_p\,. \tag{6.54}$$

One further separates the $l = n$ term while using the periodicity $m_{p+n} = m_p$ in imaginary time and rewrites the sums over l, p as a product of two sums. This eventually yields [110]

$$\chi = \frac{L}{Z}\sum_{\{|\alpha\rangle\}}\sum_{n=0}^{\infty}\sum_{S_n} w(\alpha,S_n)\frac{\beta}{n(n+1)}\left[\sum_{p=0}^{n-1} m_p m_p + \left\{\sum_{p=0}^{n-1} m_p\right\}\left\{\sum_{p=0}^{n-1} m_p\right\}\right] \tag{6.55}$$

$$= L\left\langle \frac{\beta}{n(n+1)}\left[\sum_{p=0}^{n-1} m_p m_p + \left\{\sum_{p=0}^{n-1} m_p\right\}\left\{\sum_{p=0}^{n-1} m_p\right\}\right]\right\rangle_{w(\alpha,S_n)}\,. \tag{6.56}$$

In the simulation the two sums in Eq. (6.56) need to be calculated by traversing the operator sequence. The effort for measuring χ therefore scales as the algorithm with complexity $\mathcal{O}(\beta N)$ when the magnetisation is not calculated from scratch at every propagation step p but gradually updated while propagating through the sequence.

6.3.2 Correlation function and its characteristic length

As a key quantity of Q-FSS, the characteristic length scale ξ will be calculated in this thesis in order to demonstrate its FSS behaviour $\xi_L \sim L^{\text{९}}$. As described in Sec. 3.4 it

is calculated via the correlation functions

$$\xi_L^{(\mathrm{LR}\omega)} = \frac{1}{q_{\min}} \left[\frac{\tilde{G}_L(0, \omega = 0) - \tilde{G}_L(q_{\min}, \omega = 0)}{\tilde{G}_L(q_{\min}, \omega = 0)} \right]^{1/\sigma}, \tag{6.57}$$

$$\xi_L^{(\mathrm{LR}\tau)} = \frac{1}{q_{\min}} \left[\frac{\tilde{G}_L^2(0, \tau = 0) - \tilde{G}_L^2(q_{\min}, \tau = 0)}{\tilde{G}_L^2(q_{\min}, \tau = 0)} \right]^{1/\sigma} \tag{6.58}$$

for $\sigma < 2 - \eta_{\mathrm{SR}}$. We will focus on calculating this quantity in the long-range mean-field regime of the one-dimensional chain.[1] During the simulation, the correlation functions

$$G(\boldsymbol{r}_i - \boldsymbol{r}_j, \omega = 0) = \int_0^\beta \left\langle \sigma_i^z(\tau) \sigma_j^z(0) \right\rangle \mathrm{d}\tau \tag{6.59}$$

$$= \left\langle \frac{\beta}{n(n+1)} \left[\sum_{p=0}^{n-1} \sigma_{i,p}^z \sigma_{j,p}^z + \left\{ \sum_{p=0}^{n-1} \sigma_{i,p}^z \right\} \left\{ \sum_{p=0}^{n-1} \sigma_{j,p}^z \right\} \right] \right\rangle_{w(\alpha, S_n)}, \tag{6.60}$$

which can be derived analogous to the susceptibility formula, and

$$G(\boldsymbol{r}_i - \boldsymbol{r}_j, \tau = 0) = \left\langle \sigma_i^z \sigma_j^z \right\rangle \tag{6.61}$$

$$= \left\langle \frac{1}{n} \sum_{p=0}^{n-1} \sigma_{i,p}^z \sigma_{j,p}^z \right\rangle_{w(\alpha, S_n)} \tag{6.62}$$

are sampled. After the simulation, the characteristic length ξ is calculated. When sampling the correlations among all sites i and j at all propagation steps p, this leads to a scaling of $\mathcal{O}(\beta N^3)$ which is way worse than the computational complexity of the updates. Even though one could eliminate the average over imaginary time in Eq. (6.62) to reduce the complexity to $\mathcal{O}(N^2)$, this is not possible for Eq. (6.60) as the sum over imaginary time is intrinsic in the definition of the zero-frequency correlation function. However, by realising that the correlations $\sigma_i^z \sigma_j^z$ among two sites i and j are not altered at the order $\mathcal{O}(\beta N)$ times in imaginary time but only $\mathcal{O}(\beta)^2$ one can measure the correlation functions Eq. (6.60) and Eq. (6.62) in $\mathcal{O}(\beta N^2)$ time. This is achieved by traversing imaginary time while memorising the non-trivial propagation step last$[i]$ of the last preceding spin-flip operator for every site separately. When a spin flip occurs at a site j at non-trivial propagation step p_{nt}, one needs to update the correlation function

$$G[i, j] \to G[i, j] + \sigma_{i,p_{\mathrm{nt}}}^z \sigma_{j,p_{\mathrm{nt}}}^z (p_{\mathrm{nt}} - \max(\mathrm{last}[i], \mathrm{last}[j])) \tag{6.63}$$

[1] We refrain from calculating the correlation function or characteristic length scale for the 4d TFIM as the longest distance between two spins $\sim \mathcal{O}(N^{1/4})$ is rather small in comparison to the 1d case $\sim \mathcal{O}(N)$ for a system of N sites.

[2] The total amount of spin-flip operators scales as $\mathcal{O}(\beta N h)$ but the amount of spin-flip operators per site scales as $\mathcal{O}(\beta h)$.

for every site i before the local magnetisation is propagated with $\sigma^z_{j,p_{\mathrm{nt}}+1} = -\sigma^z_{j,p_{\mathrm{nt}}}$. One further needs to update $\mathrm{last}[j] = p_{\mathrm{nt}}$. In order to avoid that the measurement completely dominates the simulation, we only measure the correlations between a fixed site $i = 1$ and $j \in \{1, \ldots, N\}$. This finally reduces the complexity of the measurement to $\mathcal{O}(\beta N)$.

6.4 Convergence to zero-temperature properties

The QMC formulation via SSE is a high-temperature series expansion. Performing a simulation at zero temperature is not possible with this method as the sequence length would diverge for $\beta \to \infty$. Nevertheless, by choosing a sufficiently low temperature, effects from finite temperature will become exponentially small. This is due to the avoided level crossing in systems of finite extent at continuous phase transitions. The FSS of the energy gap in a finite system with linear system size L is given by (see Sec. 4.4)

$$\Delta_L(r) = L^{-\varrho z}\mathcal{D}(L^{\varrho/\nu}r) \tag{6.64}$$

in the vicinity of the critical point h_{c} ($r = 0$). At the critical point the finite-size gap therefore scales as

$$\Delta_L(r = 0) \sim L^{-\varrho z} \tag{6.65}$$

and only vanishes in the limit $L \to \infty$.

For any finite system there will be a finite energy gap between the ground state of the system and the excited states. This gap becomes progressively sharper for increasing system size and potentially closes only for an infinite system (see Fig. 6.7). If we choose the temperature such that $T \ll \Delta_L$, thermal excitations play an exponentially small role and we will sample the ground state in the simulation for most of the time.

Since we do not know the finite-size gap, we a priori do not know which temperature will be sufficient to obtain ground-state properties. Instead we check the convergence of the observables by successively cooling down the system during the simulation until a certain temperature is reached. For this we make use of an adapted version of the β-doubling scheme introduced by Sandvik [123]. The gap between the ground state and the lowest excitation in Fig. 6.7 is monotonically increasing in h. It should therefore be sufficient to check the convergence for the smallest h simulated for every L.

Beta doubling: In the β-doubling scheme each simulation is carried out at inverse temperature $\beta_n = \beta_0 2^n$ starting from $n = 0$ ($\beta = \beta_0$) until a certain $n = n_{\max}$ has been reached. At the last temperature $\beta_{\max}$ we take M samples. For each temperature β_n we start with $N_e = \frac{1}{20}M$ equilibration steps without taking any samples. After this equilibration, we take M_n samples. While cooling down the system ($n < n_{\max}$),

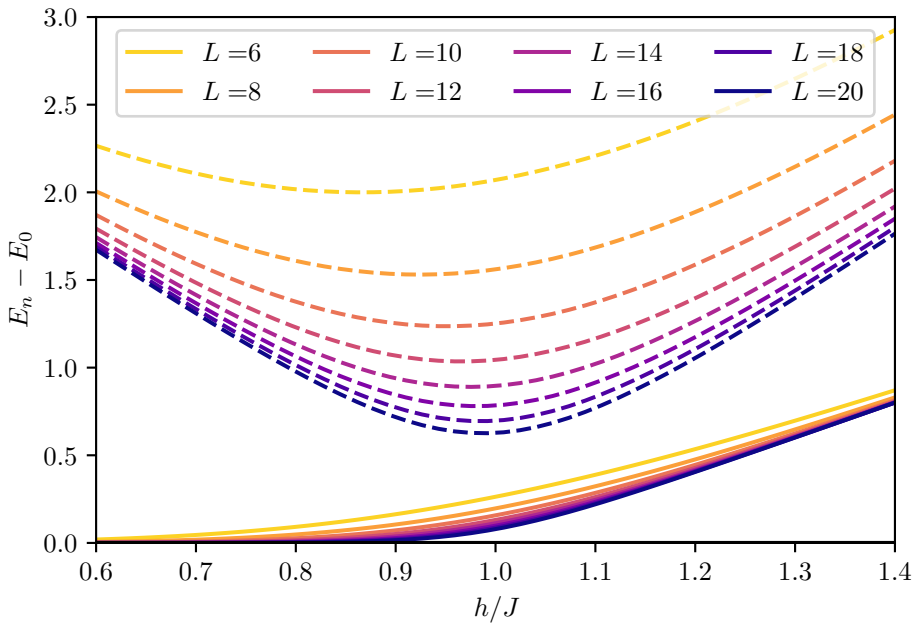

Figure 6.7: *Low-energy spectrum with respect to the ground-state energy in the $k = 0$-symmetry sector for the 1d TFIM ($h_c = 1$) obtained from exact diagonalisation performed with the package QuSpin [121,122]. The solid lines are the eigenenergies of the first excited state. For a finite system the difference to the ground-state energy remains finite up to $h = 0$ while for an infinite system the ground state is degenerate in the whole ordered phase $h < h_c$. These degenerate ground states are related by the symmetry that is broken, namely the spin-flip ($\mathbb{Z}_2$) symmetry. They differ by the Parity $\mathcal{P} = \prod_i \sigma_i^x$ with the global ground state having even parity (+1). The dashed lines are the second excited state in the $k = 0$-sector with the gap also becoming progressively sharper according to Eq.* (6.65).

only $M_n = \frac{1}{10}M$ samples are taken in order to not waste too much time at high temperatures.

Decreasing the temperature is done by doubling the inverse temperature $\beta_{n+1} = 2\beta_n$ and the length of the SSE sequence. In order to save equilibration time, the SSE sequence from the current β_n is recycled for β_{n+1} by doubling the sequence $S_\mathcal{L}$ according to

$$S_{2\mathcal{L}} = [a_1, b_1], \ldots, [a_\mathcal{L}, b_\mathcal{L}], [a_\mathcal{L}, b_\mathcal{L}], \ldots, [a_1, b_1]\,.$$

The convergence to the ground state is checked after the simulation for the observables of interest. In Fig. 6.8 this procedure is demonstrated for the squared magnetisation over decreasing temperature. Systems with smaller linear system size L converge faster in β. The curves in Fig. 6.8 appear to have converged in β for all system sizes L except

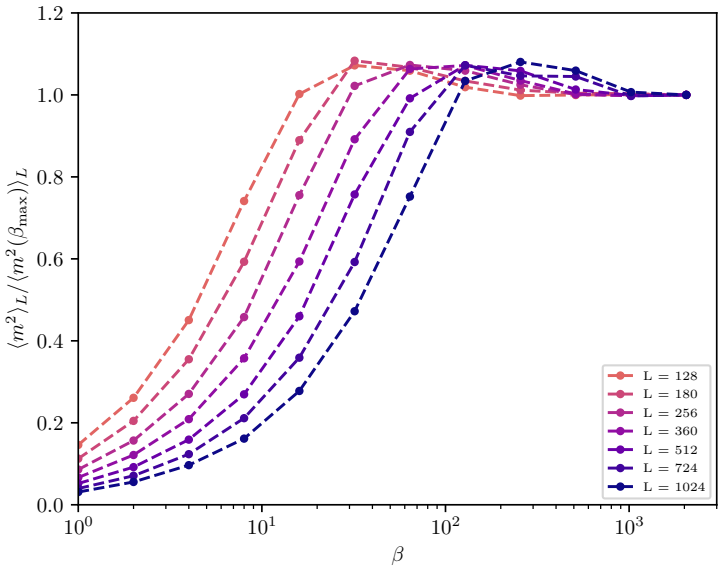

Figure 6.8: *Beta-doubling scheme illustrated for the ferromagnetic LRTFIM with $\alpha = 3.5$ and $h \approx h_c$. The starting temperature was chosen to be $\beta_0 = 1$ and $n_{\max} = 11$ such that $\beta_{\max} = 2048$. For large β the measurements for $\langle m^2 \rangle_L$ saturate and we expect the temperature effects to be negligible in comparison to the statistical error.*

for the largest $L = 1024$. For this specific example, the two largest systems were again simulated with $\beta_{\max} = 4096$ in order to avert effects due to finite temperature.

6.5 Extraction of critical fields and exponents

From the simulations we will obtain estimates O_i for observables $\mathcal{O}_{L_i}(h_i, L_i, T = 0)$ with $i \in \{0, \ldots, M-1\}$ forming a set of M data points

$$\mathcal{D} = \{((h_i, L_i), O_i)\}_{i \in \{0,\ldots,M-1\}} \,. \tag{6.66}$$

We concentrate on two methods for extracting critical exponents from this data. While the data collapse considers a whole set of curves $\mathcal{O}_L(h)$ for different h and L simultaneously, the second method only considers a pair of values $\mathcal{O}_L(h_c)$ and $\mathcal{O}_{bL}(h_c)$ of observables at the critical point h_c.

6.5.1 Data collapse

By reorganising the scaling form Eq. (4.80) one can calculate the scaling function $\Omega(\tilde{r})$ with $\tilde{r} = L^{\wp/\nu} r$ from $\mathcal{O}_L$

$$\Omega(\tilde{r}) = L^{\wp\omega/\nu} \mathcal{O}_L(L^{-\wp/\nu}\tilde{r}) \tag{6.67}$$

if one knows the critical exponents ω, ν and the critical field value h_c. The latter is needed for converting the field values h to $r = (h - h_\mathrm{c})$. As the scaling function $\Omega(\tilde{r})$ does not depend on L, all curves of $\mathcal{O}_L(L^{-\wp/\nu}\tilde{r})$ for several different L will collapse to one single curve when rescaled with the correct set of values $(\omega, \nu, h_\mathrm{c})$. This property can be utilised to find those values. For this we interpret $\mathcal{O}$ as a function of the tupel (h, L)

$$\mathcal{O} : (h, L) \to \mathbb{R}\,, \tag{6.68}$$

$$(h, L) \mapsto \mathcal{O}(h, L)\,. \tag{6.69}$$

The data set $\mathcal{D}$ is then fitted to a function

$$f((h, L); p_0, p_1, p_2, \boldsymbol{a}) = L^{-\wp p_0} P(L^{\wp p_1}(h - p_2); \boldsymbol{a}) \tag{6.70}$$

with free parameters $(p_0, p_1, p_2, \boldsymbol{a})$ and a polynom P of order n

$$P(\tilde{r}; \boldsymbol{a}) = \sum_{i=0}^{n} a_i \tilde{r}^i\,. \tag{6.71}$$

For the correct parameters $(p_0, p_1, p_2, \boldsymbol{a}) = (\omega/\nu, 1/\nu, h_\mathrm{c}, \boldsymbol{a}_\Omega)$ the function f reduces to $\mathcal{O}$ if the polynom $P(\tilde{r}, \boldsymbol{a}_\Omega)$ sufficiently parametrises the scaling function $\Omega(\tilde{r})$. The resulting fit parameters are therefore estimates for the critical exponents which we use to explore the criticality of the LRTFIM.

After the fit was conducted one can demonstrate its validity by rescaling the set $\mathcal{D}$ according to Eq. (6.67)

$$\tilde{r}_i = L_i^{\wp p_1}(h_i - p_2)\,, \tag{6.72}$$

$$\Omega_i = L_i^{\wp p_0} \mathcal{O}_i \tag{6.73}$$

and plotting the new set of data points $(\tilde{r}_i, \Omega_i)$ with Ω_i being estimates for the scaling function. Those points should collapse onto the common curve $P(\tilde{r}, \boldsymbol{a}_\Omega)$ if the fitting parameters (p_0, p_1, p_2) sufficiently approximate $(\omega/\nu, 1/\nu, h_\mathrm{c})$. This procedure is demonstrated in Fig. 6.9.

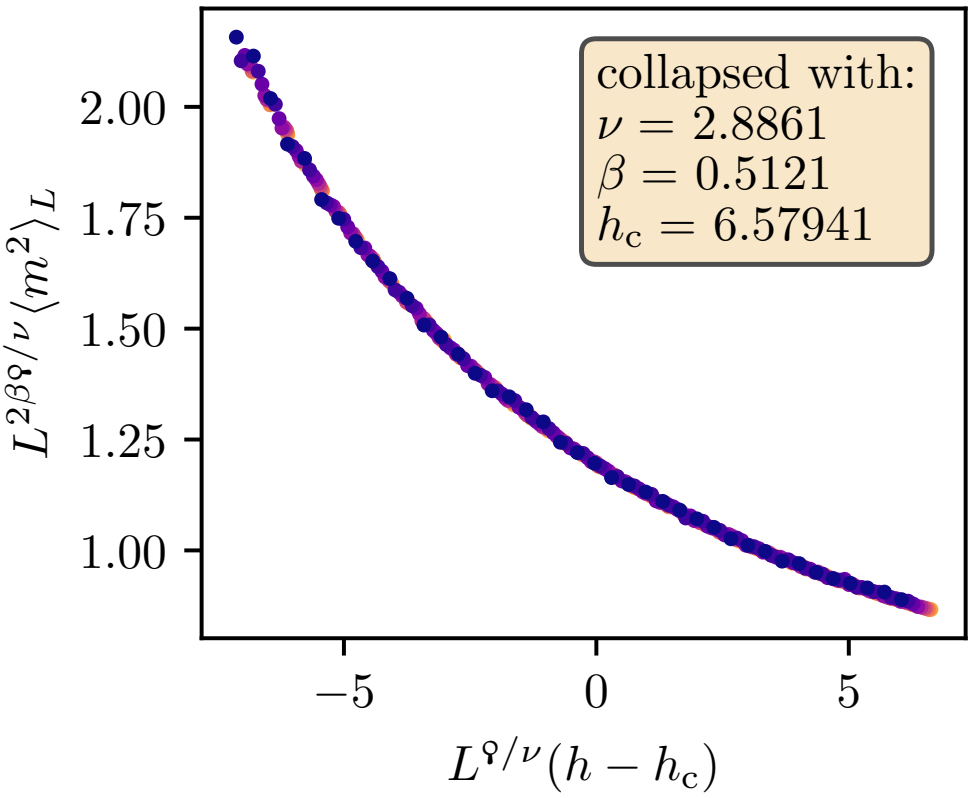

Figure 6.9: *Data collapse of the squared magnetisation for the ferromagnetic LRTFIM for decay exponents $\alpha = 1.35$. Left: Raw data points for the squared magnetisation for different system sizes L. Right: The same data points as on the left but rescaled according to FSS. The data points for all different system sizes L collapse onto one single curve. The intervals for the transverse field of the raw data are chosen such that the rescaled range is approximately the same for all L.*

6.5.2 Pairwise FSS (phenomenological renormalisation)

There is another method for estimating h_c, ν and ω, which has the additional advantage that it takes into account systematic errors due to corrections to FSS [35,75]. The basic idea is to compare observables for two system sizes L and bL and extrapolate the results to $bL \to \infty$. One might interpret this procedure as some kind of phenomenological renormalisation [35]. The two explicit methods differ for h_c, ν and ω.

We start with the Binder cumulant and recall the scaling behaviour of the $2n$-moments of the magnetisation

$$\langle m^{2n} \rangle_L(h) = L^{-2n\beta/\nu} \mathcal{M}_{2n}(L^{1/\nu}(h - h_\mathrm{c})) \qquad \text{with} \quad n \in \mathbb{N}\,. \tag{6.74}$$

By inserting this into the formula for the Binder cumulant, its scaling behaviour can be written as

$$U_L(h) = \frac{3}{2}\left[1 - \frac{\mathcal{M}_4(L^{1/\nu}(h - h_\mathrm{c}))}{3\left[\mathcal{M}_2(L^{1/\nu}(h - h_\mathrm{c}))\right]^2}\right] \tag{6.75}$$

$$= \mathcal{U}(L^{1/\nu}(h - h_\mathrm{c}))\,. \tag{6.76}$$

In particular, the Binder cumulant becomes independent of the system size at the critical point $h = h_\mathrm{c}$ due to the scaling behaviour of the magnetisation. The intersection point of the Binder cumulant for different system sizes therefore give an estimate for the critical point h_c [35]. Moreover, as the β-dependent prefactors cancel, the Binder cumulant can be used to determine ν independent from other critical exponents like β and γ. Taking the derivative of the Binder cumulant with respect to h at the critical point, yields

$$\left.\frac{\partial U_L}{\partial h}\right|_{h=0} = L^{1/\nu} \left.\frac{\partial \mathcal{U}}{\partial h}\right|_{h=0}\,, \tag{6.77}$$

where the derivative of the scaling function $\mathcal{U}$ is independent of the system size. Taking the quotient of these derivatives for different system sizes L and bL

$$\left.\frac{\partial U_{bL}}{\partial U_L}\right|_{h=0} = b^{1/\nu} \tag{6.78}$$

gives an estimate for the critical exponent ν. One can also derive an estimate for the ratio $\frac{\beta}{\nu}$ with the $2n$-moments of the magnetisation at the critical point

$$-\frac{\log\left[\langle m^{2n}\rangle_{bL}(h = h_\mathrm{c}) / \langle m^{2n}\rangle_L(h = h_\mathrm{c})\right]}{2n \log b} = \frac{\beta}{\nu} \tag{6.79}$$

by considering their scaling behaviour Eq. (6.74). Similarly, estimates for a general observable $\mathcal{O} \sim |r|^\omega$, e. g. $\mathcal{O} = \chi$ and $\omega = -\gamma$, can be calculated with

$$-\frac{\log\left[\langle \mathcal{O}\rangle_{bL}(h = h_\mathrm{c}) / \langle \mathcal{O}\rangle_L(h = h_\mathrm{c})\right]}{\log b} = \frac{\omega}{\nu}\,. \tag{6.80}$$

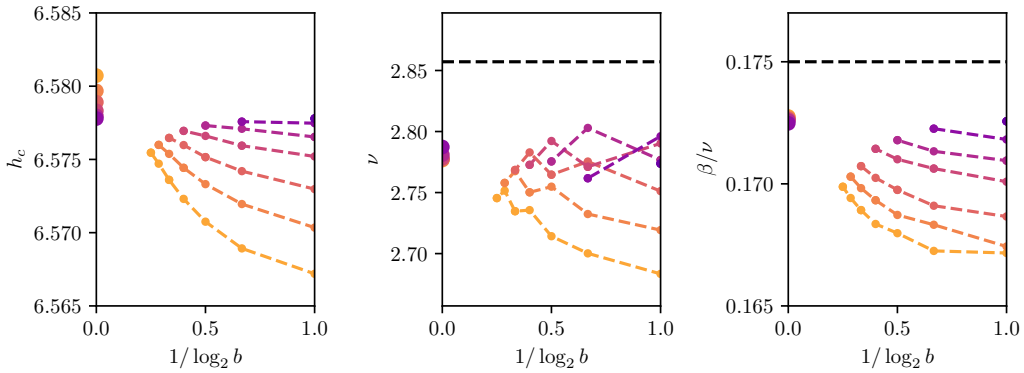

Figure 6.10: *Pairwise estimates for h_c, ν and β/ν with system sizes L and bL for the ferromagnetic LRTFIM with $\alpha = 1.35$ in the long-range mean-field regime. The stimates are extrapolated to $1/\log_2 b \to 0$ for all L and the extrapolations are denoted by dots on the y-axis. The theoretic predictions for ν and β/ν are illustrated by the dashed black lines. The extrapolations tend towards the theoretic predictions by taking into account first order corrections to FSS [35].*

These estimates for h_c, ν and ω/ν are all calculated for pairwise system sizes L and bL by interpolating the data points $O_i(h_i, L_i)$ of our data set $\mathcal{D}$ to obtain their values at $h = h_c$. For every L, the estimates are linearly extrapolated towards $\ln(b)^{-1} \to 0$ which takes into account leading corrections to FSS [35]. Our final estimates are obtained by averaging over the results of extrapolation. This procedure is illustrated in Fig. 6.10 for h_c, ν and β/ν. The extrapolation of the ν estimates is most prone to errors as one needs excellent data for calculating derivatives numerically as in Eq. (6.78). The need for data with excellent statistics is one major disadvantage of this method. Moreover, the different pairwise estimates are not independent and in principle one needs to take this into account when extrapolating to $\ln(b)^{-1} \to 0$. This correlation among the estimates is also clearly visible for the ν estimates in Fig. 6.10 as the curves for all L exhibit the same zig-zag-behaviour for large b as they are obtained from comparing the different L with a common system of size bL respectively.

In contrast to the data collapse explained before, this method has the advantage of obtaining the critical point h_c and the critical exponents ν and ω/ν independently from each other. Furthermore, one can take into account correction to FSS by extrapolating $bL \to \infty$ [35].

We will focus on extracting the critical exponent ν with the data collapse as the extrapolations for ν are not reliable. We think that the benefit from taking into account leading corrections is smaller than the disadvantage of having unreliable results. However, the estimates for β/ν and γ/ν obtained from the extrapolations are

more stable and will also be calculated for the ferromagnetic LRTFIM where we were capable of obtaining data with decent statistics.

7 Results for the ferromagnetic LRTFIM on the linear chain

In this chapter we discuss the results obtained for the ferromagnetic LRTFIM on the one-dimensional chain. Zero-temperature estimates for the magnetisation, order-parameter susceptibility and correlation functions were obtained from simulations of finite chains and at finite temperature by means of the SSE algorithm introduced in Ch. 6. The resulting data set was processed by the method of data collapse and, where feasible, with pairwise FSS techniques introduced in Sec. 6.5 for obtaining the critical fields h_c, the full set of critical exponents and the exponent $\wp$ introduced by the Q-FSS formalism. During the determination of critical fields and critical exponents, the exponent $\wp$ was fixed to its theoretical value $\wp = \max(1, d/d_\mathrm{uc})$ as its respective fit parameter would not have been linearly independent from the parameter representing ν. The simulations were performed for different decay exponents $\alpha = \sigma + 1$ in all three criticality regimes identified in Sec. 3.3.1 with a special focus on the intermediate regime of varying critical exponents.

7.1 Critical field

Starting with the critical field values, we present the results for h_c in Fig. 7.1. Those were derived by means of data collapses of the squared magnetisation $\langle m^2 \rangle_L$ and the order-parameter susceptibility χ as well as by the intersections of the Binder cumulant. In the inset of Fig. 7.1 the results $h_\mathrm{c,x}$ for the different methods are compared with $h_\mathrm{c,mag}$ obtained from the data collapse of $\langle m^2 \rangle_L$. The relative differences are calculated with

$$\Delta_{h_\mathrm{c}} = \frac{h_\mathrm{c,mag} - h_\mathrm{c,x}}{h_\mathrm{c,mag}} \,. \tag{7.1}$$

Our own results are in excellent agreement with each other with relative differences of the order $10^{-3}\% - 10^{-2}\%$ and agreeing within their error. We additionally compare our results with high-field series expansion results from Ref. [42] which differ by $\approx 0.2\%$ from our results. The highest discrepancy is located around the boundary from the short-range regime to the intermediate regime of varying critical exponents ($\sigma \approx 2$).

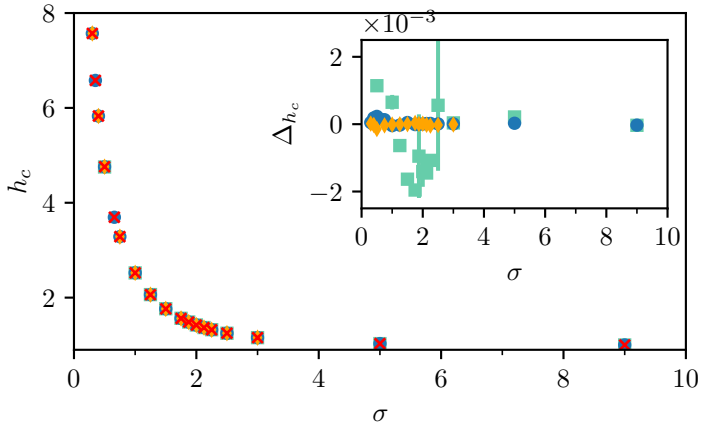

Figure 7.1: *Critical field values for the ferromagnetic LRTFIM in 1d with decay exponent $\alpha = 1 + \sigma$ obtained by the intersection method of Binder cumulants and data collapses of $\langle m^2 \rangle_L$ as well as χ_L. For comparison, we additionally included data from high-field series expansion from Ref. [42] (pCUT, green square). The inset shows the relative difference $\Delta_{h_c} = \frac{h_{c,\mathrm{mag}} - h_{c,\mathrm{x}}}{h_{c,\mathrm{mag}}}$ between the estimates $h_{c,\mathrm{mag}}$ obtained from the data collapse of $\langle m^2 \rangle_L$ and the estimates $h_{c,\mathrm{x}}$ obtained from the other methods. Our own results agree within error but may suffer from the same systematic error due to corrections to FSS. Close to the boundary to the short-range regime ($\sigma = 2$), the pCUT results are systematically above our results but the relative difference is still small with $\lessapprox 0.2\%$.*

In the limit $\sigma \to \infty$, the critical field attains its short-range value of $h_c = 1$. For decreasing decay exponent σ, the critical field h_c increases as the coupling among non-adjacent spins becomes stronger making the ground state more robust against spin flips introduced by the transverse field h. For $\sigma \to 0$, the critical field h_c diverges as the thermodynamic stability collapses and the ground-state energy becomes superextensive.

7.2 Critical exponents

The critical exponents ν, β/ν and γ/ν were extracted by data collapse of the squared magnetisation $\langle m^2 \rangle_L$ and the order-parameter susceptibility χ_L. For β/ν and γ/ν we also calculated the extrapolated estimates obtained for pairs of linear system size L and bL (pairwise FSS) as described in Sec. 6.5.2 by comparing the respective values of the squared magnetisation (β/ν) as well as of the order-parameter susceptibility (γ/ν) at the critical point $h = h_c$. We were not able to obtain reliable results from the extrapolation technique for ν because the data quality was not sufficient. This

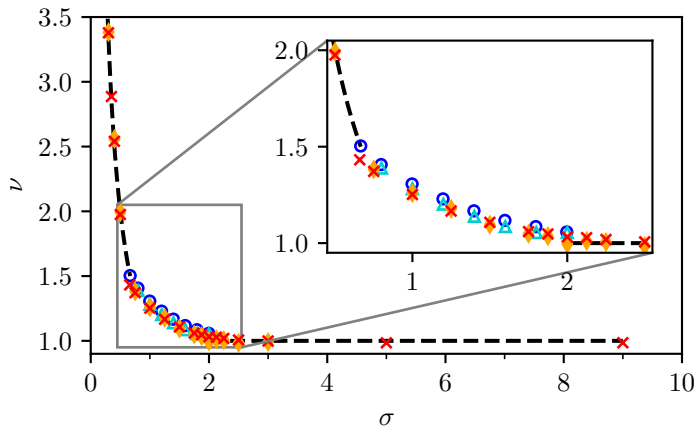

Figure 7.2: *Critical exponent ν for the ferromagnetic LRTFIM on the one-dimensional chain for different decay exponents $\alpha = \sigma + 1$ obtained from data collapse of $\langle m^2 \rangle_L$ (red crosses) and χ (orange diamonds). In the intermediate regime $2/3 < \sigma < 2$ additional results from Ref. [68] (DMRG, blue circles) and from Ref. [63] (FRG, cyan triangles). The short-range exponent $\nu = 1$ as well as the long-range mean-field exponent $\nu = 1/\sigma$ are depicted by dashed black lines in the respective regimes. At the boundary to the short-range regime the sharp transition is rounded making it hard to validate the expected regime change at $\sigma = 2 - \eta_{\mathrm{SR}}$ claimed by Ref. [63]. At the boundary to the long-range mean-field regime, where $d = d_{\mathrm{uc}}$, logarithmic corrections to FSS occur which were not taken into account [32].*

is because the technique involves the derivatives of the Binder cumulant which itself already suffers from lower statistical quality compared to the squared magnetisation. Moreover, the extrapolation formalism requires data precisely at the critical point in constrast to the data collapse. However, as we focused on the data collapse, we acquired data not only in the direct vicinity of h_{c} but also in its neighbourhood as the critical exponent ν is hidden in the finite-size rounding close to the critical point, i. e. the functional dependence of finite-size observables on the transverse field h.

The critical exponent ν was therefore only extracted from the data collapses of $\langle m^2 \rangle_L$ and χ_L and the results from these collapses are presented in Fig. 7.2. In the figure we included recent results obtained by DMRG [68] and functional RG (FRG) [63] in the intermediate regime. Even though our results are systematically below theirs in the whole regime and better meet the expected short-range behaviour for $\sigma = 2$, they do not reflect the expected regime boundary $\sigma = 2 - \eta_{\mathrm{SR}}$ claimed by Ref. [63]. This could be due to a rounding effect close to the boundary hindering us from resolving the regime change sharply. This rounding of the exponents was reduced by excluding smaller systems from the data collapse and probably originates from finite-size corrections

to scaling. At the other side of the intermediate regime, our results fail to reproduce the expected mean-field behaviour precisely at the boundary $\sigma = 2/3$, where $d = d_{\mathrm{uc}}$, in contrast to the FRG results from Ref. [63]. However, this is to be expected as logarithmic corrections occur at the upper critical dimension [32] which we did not allow for in the data collapse. This led to a systematic deviation from the expected mean-field behaviour at $\sigma = 2/3$ and probably also in the vicinity of this regime boundary. Deep in the long-range mean-field regime, our results for ν are consistent with the predictions from Gaussian field theory. The good agreement in the long-range regime with the expected behaviour $\nu = 1/\sigma$ validates the modified FSS form above the upper critical dimension which takes into account dangerous irrelevant variables (see Sec. 4.4).

For calculating the full set of exponents, we had to extract at least two more critical exponents. Those were chosen to be β and γ. In principle, we could have extracted other critical exponents like α or δ but calculating the corresponding observables is numerically more challenging. The control-parameter susceptibility with critical exponent α is easy to implement but suffers from the same numerical drawback as the heat capacity of being the small difference of large numbers at low temperature. For calculating δ one would need to introduce an additional longitudinal field into the algorithm, which would change the probability with which the cluster in the off-diagonal update are flipped [59]. We therefore concentrated on the exponents β and γ as the corresponding observables are well-behaved and easy to obtain.

The squared magnetisation and order-parameter susceptibility yield the exponents as ratios β/ν and γ/ν[1] such that one needs estimates for ν in order to calculate the pure exponents β and γ. For this we made use of the estimates for ν coming from the data collapse of the squared magnetisation as these have a higher accuracy than those from the collapse of the order-parameter susceptibility.

The resulting values for β and γ are shown in Fig. 7.3 and Fig. 7.4 respectively. All methods meet the nearest-neighbour critical exponents for $\sigma > 2$. The results for the exponent γ differ by less than 1% from the short-range value $\gamma = 1.75$ for all $\sigma \geq 2$. The estimates for β differ by less than 2% from their short-range value $\beta = 0.125$ deep in the short-range regime. However, our results for β are suffering from rounding near the upper boundary of the intermediate regime. This rounding for β is probably more pronounced compared to the rounding for γ as the rounding of its constituents β/ν and ν add up as both are overestimated in this transition region between the intermediate and short-range regime. In contrast, the rounding tends to underestimate γ/ν balancing the overestimation of ν in the calculation for $\gamma = \gamma/\nu \cdot \nu$. The rounding

[1] For the data collapse one can in principle use ν and β (γ) as free fit parameters. However, those fit parameters are more correlated than ν and β/ν (γ/ν). As ν is harder to determine with larger uncertainties, this also spoils β (γ). We therefore decided to fit the respective ratios β/ν and γ/ν and use the ν estimates with highest accuracy for the conversion of both exponents.

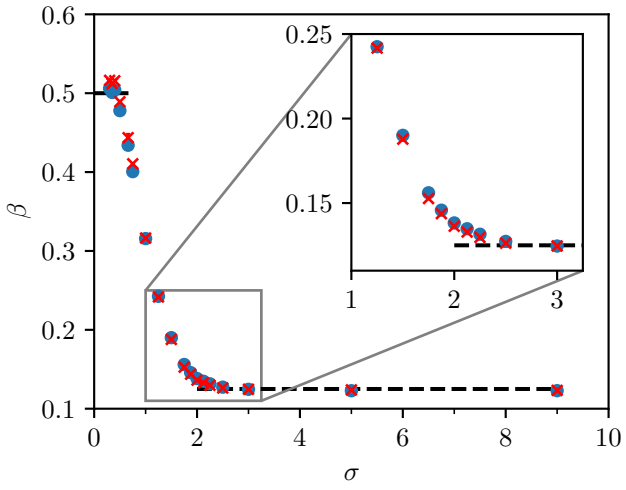

Figure 7.3: *Critical exponent β for the ferromagnetic LRTFIM on the one-dimensional chain for different decay exponents $\alpha = \sigma + 1$ obtained from data collapse of $\langle m^2 \rangle_L$ (red crosses) and from the extrapolation of pairwise FSS (blue circles). Both methods yielded the ratio β/ν which were converted to β by using the estimates for ν from the $\langle m^2 \rangle_L$-collapse.*

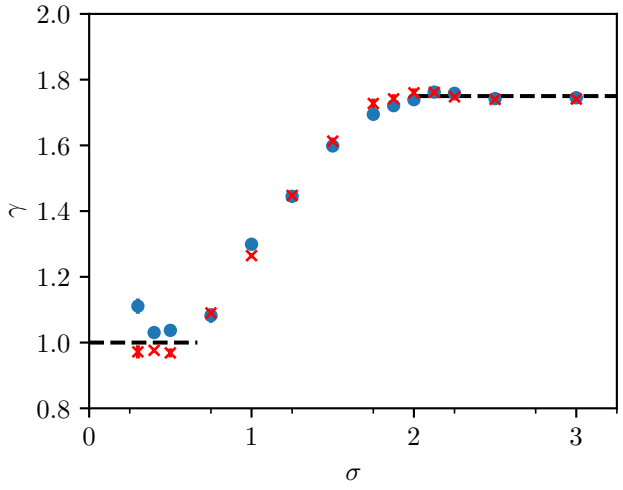

Figure 7.4: *Critical exponent γ for the ferromagnetic LRTFIM on the one-dimensional chain for different decay exponents $\alpha = \sigma + 1$ obtained from data collapse of χ_L (orange diamonds) and from the extrapolation of pairwise FSS (blue circles). Both methods yielded the ratio γ/ν which were converted to γ by using the estimates for ν from the $\langle m^2 \rangle_L$-collapse as those ν have the highest accuracy.*

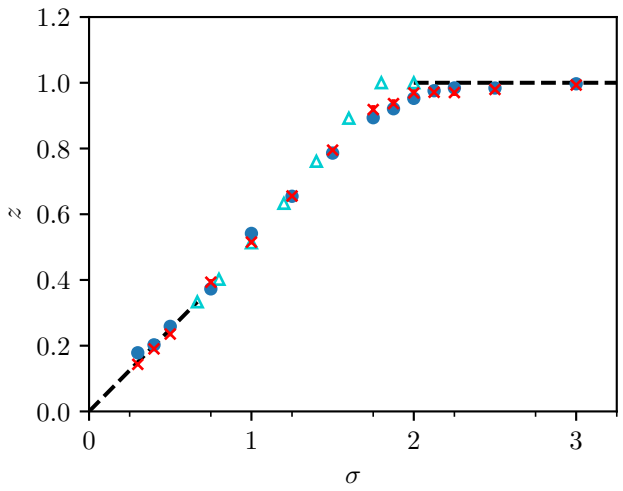

Figure 7.5: *Dynamical critical exponent z for the ferromagnetic LRTFIM on the one-dimensional chain for different decay exponents $\alpha = \sigma + 1$ calculated from β/ν and γ/ν. For the conversion the generalised hyperscaling relation is used together with the Essam-Fisher relation. In the intermediate regime results from Ref. [63] (functional RG, cyan triangles) are shown for comparison. Except for the transition from the short-range regime to the intermediate regime where the data-collapse results are not as sharp as the FRG results both are in agreement.*

for γ is therefore almost cancelled. In the long-range mean-field regime, the results of the data collapses are systematically above (below) the mean-field expectation for β (γ) by $3\% - 4\%$ and the logarithmic corrections at the edge of the mean-field regime again lead to a large systematic error.

These three exponents ν, β and γ are sufficient for calculating all other exponents from the scaling relations. In Fig. 7.5 we additionally present the dynamical critical exponent z calculated from β/ν and γ/ν with

$$z = \frac{2\beta}{\nu} + \frac{\gamma}{\nu} - \frac{d}{\mathfrak{d}} \tag{7.2}$$

by combining the generalised hyperscaling relation (Eq. (4.82)) with the Essam-Fisher relation (Eq. (2.9)). We again included results from functional RG from Ref. [63] for comparison. All estimates are consistent except for the region around the boundary to the short-range criticality where the rounding again spoils a sharp transition. In the long-range mean-field regime, our results match the expected behaviour of $z = \sigma/2$ and thus validate the generalised hyperscaling relation.

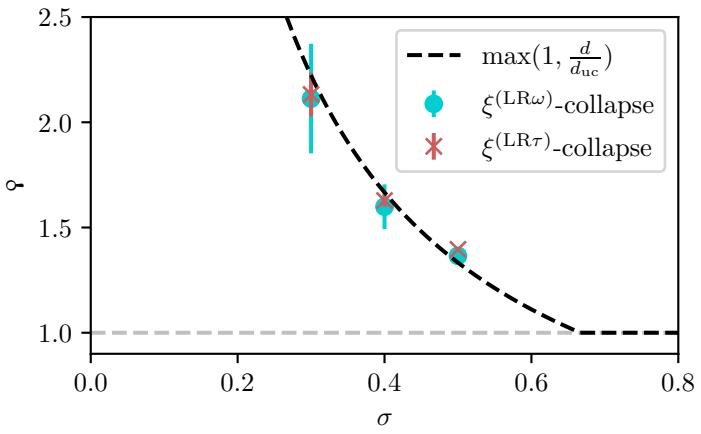

Figure 7.6: *Measurements of the exponent ϙ introduced in the context of Q-FSS as the exponent with which the finite-size characteristic length scales with the system size $\xi_L \sim L^{ϙ}$ at the critical point. The estimates were obtained from the data collapses of the finite-size characteristic lengths calculated by the zero-frequency $\tilde{G}(k, \omega = 0)$ ($\xi^{(LR\omega)}$, cyan) or equal-time correlation functions $\tilde{G}(k, \tau = 0)$ ($\xi^{(LR\tau)}$, orange) respectively. All results for ϙ are in good agreement with the expected behaviour in the long-range mean-field regime and clearly rule out a scaling of $\xi_L \sim L$.*

In this section we presented results for critical exponents in all three criticality regimes of the ferromagnetic LRTFIM and compared them with results from former studies where possible. Our results prove to be competitive and in some cases meet the expected limiting regimes better than the previous studies (see e. g. the short-range limit for ν). Furthermore, we contribute to the understanding of the criticality of the ferromagnetic LRTFIM by calculating three independent exponents, which are sufficient to calculate the full set of critical exponents, in contrast to the former studies [42, 63, 68] which only calculated up to two critical exponents. As all critical exponents matched the predictions from long-range mean-field theory considerably, this validates that Q-FSS is capable of extracting the correct criticalility from finite systems. However, this would have also been the case if we had used the approach featuring the thermodynamic length. The main difference of these approaches lies in the FSS of the characteristic length scale with the additional exponent ϙ being introduced in the Q-FSS scheme. We will therefore now turn to the correlation sector in order to offer a complete view of Q-FSS for quantum systems.

7.3 Characteristic-length exponent ϙ

A main theme of the Q-FSS scheme is the influence of DIV on the correlation sector leading to a FSS of

$$\xi_L(r) = L^{\text{ϙ}}\Xi(L^{\text{ϙ}/\nu}r) \tag{7.3}$$

in the vicinity of the critical point. In this section we present the data collapse results of the finite-size characteristic length ξ_L calculated from the zero-frequency as well as equal-time correlation function (see Eqs. (3.59) – (3.61) in Sec. 3.4 on observables) in the long-range mean-field regime, where $d \geq d_{\text{uc}}$. In the fitting procedure, we left ϙ in Eq. (7.3) as a free parameter while fixing ν to its prediction from the long-range Gaussian theory $\nu = 1/\sigma$ in order to decrease the amount of free parameters in the fit. In Fig. 7.6 the results for ϙ are compared with the predictions from Q-FSS for three different decay exponents in the long-range mean-field regime. The results clearly confirm the scaling according to Eq. (7.3) with $\text{ϙ} = d/d_{\text{uc}}$ for $d > d_{\text{uc}}$ and rule out a naive scaling of $\xi_L \sim L$ above the upper critical dimension. This result favours Q-FSS over the approach featuring the thermodynamic length analogous to the classical case [53, 90].

One might argue that, by virtue of the quantum-classical mapping, the quantum systems correspond to classical systems with an additional dimension and the Q-FSS scheme is straightforwardly generalisable. However, when we generalised the argument for the modified scaling power of the free energy density in the presence of DIV (see Sec. 4.3), we already encountered the peculiar role of the imaginary-time direction, which builds up the additional dimension of the classical system in a quantum-classical mapping. While, for classical systems, the modified scaling power $d^* = d$ is not altered by the DIV [34], we found $(d + z)^* = d + \text{ϙ}z$ for quantum systems. Moreover, the imaginary-time dimension does not contribute to the exponent $\text{ϙ} = \max(1, d/d_{\text{uc}})$ in the quantum case while in the classical case the imaginary-time dimension corresponds to a spatial dimension of the system and therefore does contribute to ϙ. In order to ensure that this behaviour is not an artefact of the anisotropy ($z \neq 1$) of imaginary time for the long-range system, we additionally studied the four-dimensional TFIM as it is the quantum analogue to the well-studied five-dimensional classical Ising model.

8 Results for the 4d TFIM: Link between quantum and classical Q-FSS

The TFIM for dimensionality $d = 4$ can be mapped to the classical Ising model for dimensionality $D = d + 1 = 5$ and is therefore the paradigmatic quantum analogue for studying physics above the upper critical dimension. Furthermore, studying the 4d TFIM provides a direct link of the quantum version of Q-FSS to the original Q-FSS developed for classical systems. In this chapter we present the results for ϙ obtained from finite-temperature SSE simulations of the four-dimensional TFIM on finite hypercubic lattices. For this, we performed data collapses of $\langle m^2 \rangle_L$ and χ_L while fixing the mutual mean-field critical exponents

$$\nu = \frac{1}{2} \qquad \beta = \frac{1}{2} \qquad \gamma = 1 \tag{8.1}$$

shared by the classical and quantum Ising model above the upper critical dimension. The remaining free parameters in the fits, except for the ones parametrising the scaling functions, were ϙ and h_c. The collapse of the data is shown for $\langle m^2 \rangle_L$ and χ_L in Fig. 8.1 together with the respective exponents and critical field values. Both fits yield an exponent ϙ

$$\begin{aligned} ϙ_{m^2} &= 1.3310(9) \\ ϙ_{\chi} &= 1.324(9) \end{aligned} \tag{8.2}$$

very close to the prediction for the 4d TFIM with $d_\mathrm{uc} = 3$ of

$$ϙ_\mathrm{qu,4d} = \frac{d}{d_\mathrm{uc}} = \frac{4}{3}\,. \tag{8.3}$$

In contrast, for the 5d Ising model with $D_\mathrm{uc} = 4$ it was predicted by classical Q-FSS [36] and also numerically validated that [53, 90]

$$ϙ_\mathrm{cl,5d} = \frac{D}{D_\mathrm{uc}} = \frac{5}{4}\,, \tag{8.4}$$

which is clearly ruled out by the results of the data collapses Eq. (8.2). This is no contradiction as the respective systems studied are in fact not equivalent as they differ

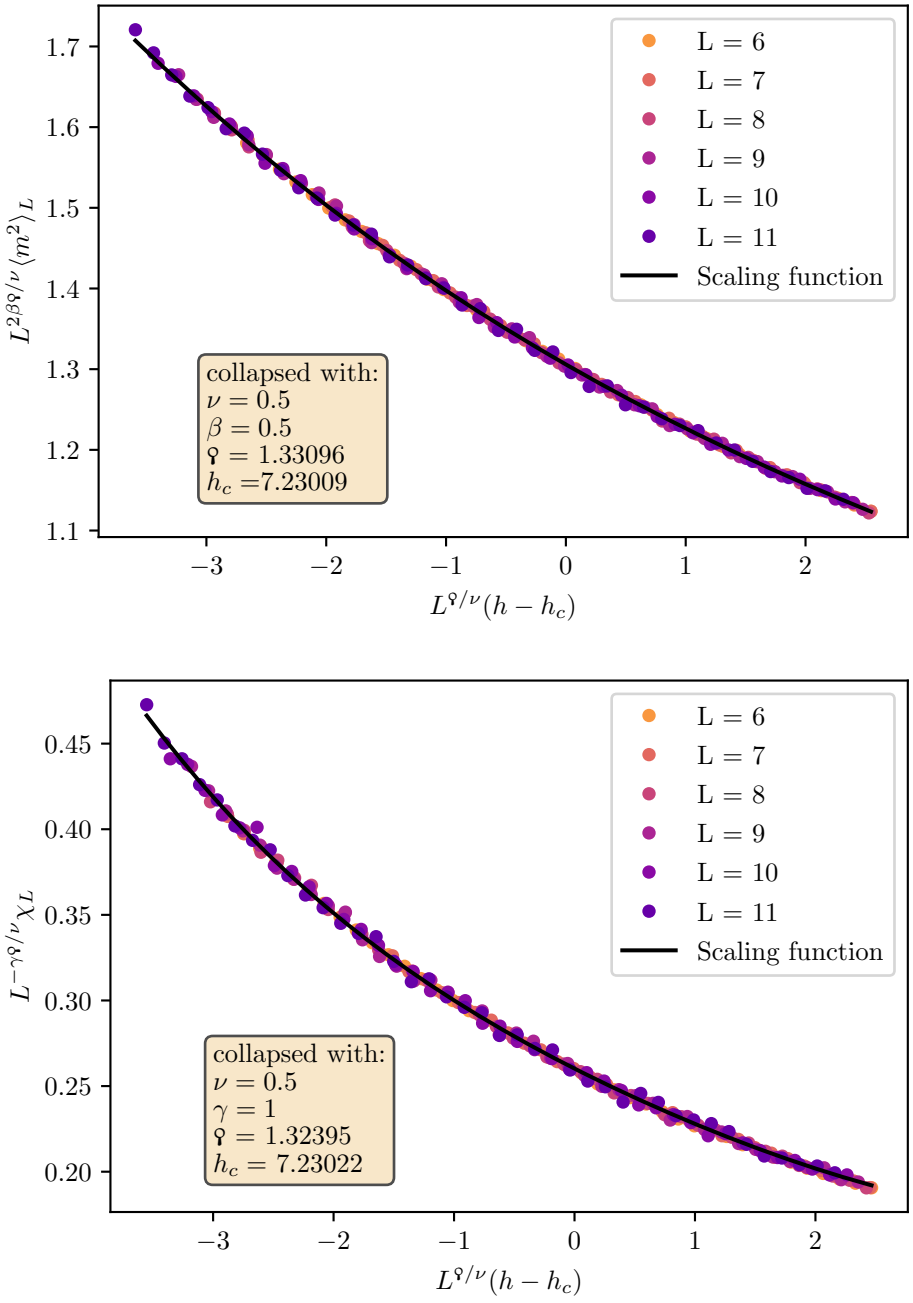

Figure 8.1: *Data collapse of the squared magnetisation (top) and order-parameter susceptibility (bottom) for the 4d TFIM. The critical exponents were fixed to their mean-field values $\nu = 0.5$, $\beta = 0.5$ and $\gamma = 1$.*

in their geometry. While the classical systems studied in Refs. [53, 90] were finite in $D = 5$ dimensions with $V = L^5$, the classical analogue of our quantum system has a rather artificial geometry of $L^4 \times \infty$ which is finite in $d = 4$ dimensions and infinite in one dimension, namely the imaginary-time dimension. The TFIM on a finite lattice with dimensionality d and at zero temperature therefore corresponds to a classical Ising model in $D = d + 1$ dimension with geometry $L^{D-1} \times \infty$. This geometry $L^{D-1} \times \infty$ was also analytically studied for the classical N-vector model[1] in the large N-limit in Ref. [85]. It was found that for $D > D_{\mathrm{uc}}$ the FSS-behaviour of the correlation length, which is the characteristic length scale of the short-range TFIM and classical Ising model close to the critical point, is $\xi_L \sim L^{(D-1)/3}$. For the five-dimensional model, this yields a scaling $\xi_L \sim L^{4/3}$ equivalent to our predictions for the 4d TFIM and in agreement with the numerical results in Eq. (8.2). Even though the calculations in Ref. [85] were performed for the spherical model ($N = \infty$), the results were argued to hold for finite N as well [85] and therefore also hold for the classical Ising model ($N = 1$).

This result provides a direct link between classical and quantum Q-FSS and further explains the distinct role of the imaginary-time dimension already encountered in the theoretical description of quantum Q-FSS.

[1] The N-vector model is a generalisation of the Ising model with spins of N components coupled to each other. The Hamiltonian is $\mathcal{H} = J \sum_{\langle i,j \rangle} \boldsymbol{s}_i \boldsymbol{s}_j$ with $\boldsymbol{s}_i$ being N-component spins. It reduces to the Ising model for $N = 1$.

9 Results for the antiferromagnetic LRTFIM on the linear chain

In this chapter we discuss the results obtained for the antiferromagnetic LRTFIM on the one-dimensional chain. Zero-temperature estimates for the magnetisation were obtained from simulations of finite chains and at finite temperature by means of the SSE algorithm introduced in Ch. 6. The resulting data set was processed using the intersection method of the Binder cumulant to pinpoint the quantum critical point and using the data collapse of the squared magnetisation to obtain estimates for the critical field h_c as well as the critical exponents β and ν. The simulations were performed for different decay exponents $\alpha = \sigma + 1$ in order to assess a potential change in universality.

9.1 Critical field

For the antiferromagnetic model the critical field values were extracted from the intersections of the Binder cumulant and from the data collapse of the squared magnetisation $\langle m^2 \rangle_L$. The resulting estimates for the critical fields are depicted in Fig. 9.1 together with the results from Ref. [42] which were calculated by a high-field series expansion and results from DMRG extracted from Ref. [41]. For large decay exponents $\sigma \to \infty$, the critical field converges towards its short-range value $h_\mathrm{c} = 1$ [7] analogous to the ferromagnetic model. For decreasing decay exponents the critical field also decreases as the competing long-range interactions reduce the stability of the symmetry-broken phase. One expects that the critical field vanishes in the limit $\sigma \to -1$ (all-to-all coupling) [41]. For $\sigma = -1$ and $h = 0$ the ground state becomes infinitely degenerate. This degeneracy is lifted for any finite transverse field $h > 0$ and there is no ordered phase [116].

In the inset of Fig. 9.1 we compare the different estimates. The pCUT results [42] yielded somewhat smaller critical fields which differ from our results by up to 1% for small decay exponents with substantial agreement of only 0.01% deviation, similar to the ferromagnetic chain, for large decay exponents. We expect our results to be of higher fidelity for small decay exponents as the DlogPadé extrapolations of the high-field series expansion tend to underestimate the critical fields for small h_c.

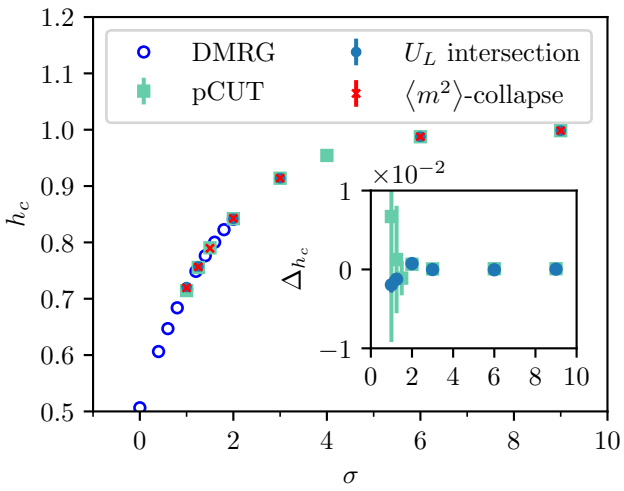

Figure 9.1: *Critical field for the antiferromagnetic LRTFIM in 1d with decay exponent $\alpha = \sigma + 1$. The estimates were obtained by the intersections of the Binder cumulant U_L which were extrapolated to infinite systems (blue circles) and by a data collapse of the squared magnetisation $\langle m^2 \rangle_L$ (red crosses). For comparison, we additionally included data from high-field series expansions from Ref. [42] (pCUT, green square). The inset shows the relative difference $\Delta_{h_c} = \frac{h_{c,\mathrm{mag}} - h_{c,\mathrm{x}}}{h_{c,\mathrm{mag}}}$ between the estimates $h_{c,\mathrm{mag}}$ obtained from the data collapse of $\langle m^2 \rangle_L$ and the estimates $h_{c,\mathrm{x}}$ obtained from the other methods. The results agree within error with the deviation and error both becoming larger for small decay exponents.*

9.2 Critical exponents

For the antiferromagnetic model the critical exponents β and ν were solely obtained from the data collapse of the squared magnetisation $\langle m^2 \rangle_L$ as the data quality was not sufficient to extract reliable results from the extrapolation of pairwise FSS. This is due to an increase of autocorrelation times of the SSE algorithm with increasingly competing long-range interactions. For small decay exponents σ, the clusters in the off-diagonal update start to percolate and a single cluster update effectively tries to flip the whole system leaving the configuration invariant ($\mathbb{Z}_2$ symmetry). For small decay exponents $\sigma < 2$, only a few small system sizes of up to $L = 64$ were accessible.

The results for the critical exponents ν and β are shown in Fig. 9.2 and Fig. 9.3 respectively. Those are contrasted with results from DMRG calculations from Refs. [40, 41]. For both exponents, the results from Ref. [40], obtained from the entanglement entropy, indicate a change in universality class for $\sigma \leq 1.25$. The more recent DMRG study in Ref. [41], where ν is extracted from the fidelity susceptibility, suggest that

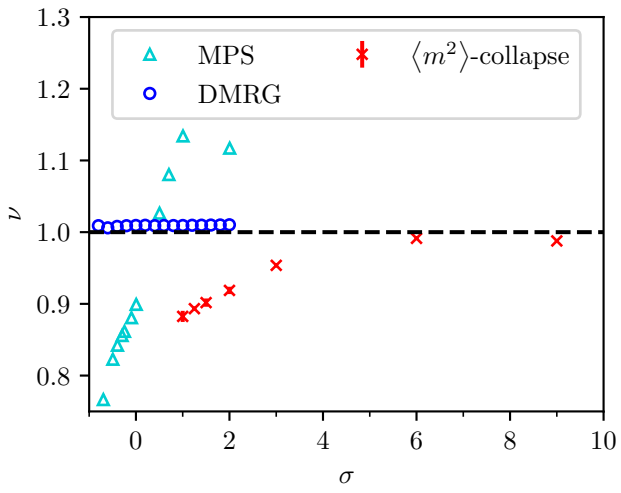

Figure 9.2: *Critical exponents ν for the antiferromagnetic LRTFIM on the one-dimensional chain for different decay exponents $\alpha = \sigma + 1$ obtained by the data collapse of the squared magnetisation $\langle m^2 \rangle_L$ (red crosses and orange diamonds). The orange diamonds depict results from data collapses with the same set of system sizes for every σ ($L \leq 64$) in order to back up our hypothesis that the drop of exponents for small σ is due to the small system sizes that are accessible for these decay exponents. While the DMRG results from Ref. [40] (cyan triangles) extracted from the entanglement entropy indicate a change of universality, recent DMRG results from Ref. [41] (blue circles) obtained by means of the fidelity susceptibility suggest that the short-range universality remains valid even for small $\sigma < 0$.*

the short-range universality remains valid for small σ. At first glance, our resuls do not favour one over the other as the critical exponents from the data collapse of the squared magnetisation decrease with decreasing σ but not in the same fashion as the results of Ref. [40]. However, we expect this drop to be caused by the selection of system sizes used for the data collapse for different decay exponents. While in the short-range limit up to $L = 1024$ spins were accessible as for the ferromagnetic counterpart, the accessible system sizes decreased for decreasing decay exponents σ. For $\sigma \in \{1, 1.25, 1.5\}$ a maximum of $L = 64$ spins were simulated and the data points were suffering from large statistical errors. This is due to an immense increase of the autocorrelation times of the algorithm for small σ such that less independent samples were generated during the simulations. In order to support our claim that the drop of the exponents is due to corrections to FSS, which become increasingly important for smaller system sizes, we performed simulations for the same set of system sizes as for the smallest three $\sigma \in \{1, 1.25, 1.5\}$ for all other investigated σ. The resulting exponents are also depicted in Fig. 9.2 and Fig. 9.3 by orange diamonds.

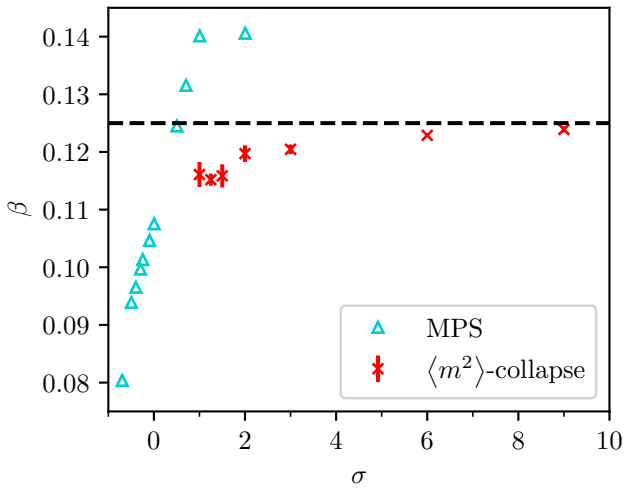

Figure 9.3: *Critical exponents β for the antiferromagnetic LRTFIM one the one-dimensional chain for different decay exponents $\alpha = \sigma + 1$ obtained by the data collapse of the squared magnetisation $\langle m^2 \rangle_L$ (red crosses and orange diamonds). The orange diamonds depict results from data collapses with the same set of system sizes for every σ ($L \leq 64$) in order to back up our hypothesis that the drop of exponents for small σ is only due to small system sizes that are accessible for these decay exponents. The DMRG results from Ref. [40] (cyan triangles) are added for comparison.*

They clearly differ from the exponents obtained from the larger system sizes and remain approximately constant over all σ in favour of our claim. We therefore propose that the universality class should remain of short-range type in the whole investigated region of decay exponents.

10 Conclusion

We studied the ferromagnetic and antiferromagnetic LRTFIM on the linear chain by means of finite-temperature SSE simulations of finite systems. The critical fields h_c and exponents ν and β were extracted from the aggregated data by exploiting the FSS of observables close to the critical point. For the ferromagnetic model we additionally extracted the critical exponent γ to render the set of critical exponents complete up to exponents that can be deduced from the extracted ones by the scaling relations. From those we further calculated the dynamical critical exponent z.

For the ferromagnetic model (see Ch. 7) the critical field values h_c were in excellent agreement with results from Ref. [42] which differed by up to 0.2% from our results. In terms of the critical exponents we were able to resolve the three expected criticality regimes $\sigma < 2/3$ with long-range mean-field critical exponents, the intermediate regime $2/3 < \sigma < 2$ with infinitely many universality classes and $\sigma > 2$ with short-range criticality. The shift of the regime boundary from the intermediate to the short-range regime from $\sigma = 2$ to $\sigma = 2 - \eta_{\mathrm{SR}}$ as argued by Refs. [63, 65] could not be resolved due to a rounding of the exponents close to the boundary. At the boundary to the mean-field regime, where $d = d_{\mathrm{uc}}$, our estimates failed to reproduce the mean-field predictions due to logarithmic corrections to FSS [32].
The limiting cases were met for all exponents up to systematical shifts of 1% to 4% depending on the specific exponents. In the intermediate regime of varying critical exponents, we compared our results for ν and z with results obtained from DMRG [68] and functional RG [63]. For ν, those results were systematically above our results while for z the results only differed close to the boundary to the short-range regime where our exponents were rounded with respect to a sharp regime change. To the best of our knowledge, the exponent β or γ have not been studied before. Our study of the LRTFIM in 1d therefore is the first to extract the complete set of critical exponents simultaneously, describing the universality class to its fullest.

For the antiferromagnetic LRTFIM (see Ch. 9) our results were still consistent with results from Ref. [42] by up to 1%. However, our results were argued to be of higher accuracy as the series expansion tends to underestimate the critical field in the regime of small h_c where this deviation became largest. Two DMRG studies [40, 41] addressing the criticality of the antiferromagnetic LRTFIM yielded exponents that behave qualitatively different with either a common universality class for all $\sigma > -1$ [41] or a change in universality with respect to the short-range universality [40]. Our results

suffered from increasing autocorrelation times for small σ but were argued to favour the results of [41] indicating that the universality remains of short-range type for all $\sigma > -1$.

Within the theoretical part of this thesis, we addressed FSS of quantum systems above the upper critical dimension. Q-FSS developed by Kenna and Berche for classical systems [36] was extended to quantum models in Sec. 4.3 with

$$\text{ϙ} = \max\left(\frac{d}{d_{\text{uc}}}, 1\right) \tag{10.1}$$

governing the finite-size behaviour of the characteristic length scale

$$\xi_L(r) = L^{\text{ϙ}}\Xi(L^{\text{ϙ}/\nu}r)\,. \tag{10.2}$$

A generalised hyperscaling relation

$$2 - \alpha = (d + \text{ϙ}z)\frac{\nu}{\text{ϙ}} \tag{10.3}$$

was analytically derived based on a microscopic argument inspired by an argument by Binder [34] for classical magnetic systems.

In the numerical part of this thesis, those findings were supported by numerical evidence for the ferromagnetic one-dimensional LRTFIM in the long-range mean-field regime ($\sigma < 2/3$) in Ch. 7. As a main theme of Q-FSS, the FSS of the characteristic length scale Eq. (10.2) was verified with ϙ matching its prediction Eq. (10.1). The successful application of the Q-FSS scheme for the squared magnetisation as well as susceptibility in the long-range mean-field regime matching the exponents predicted by mean-field theory demonstrated its utility. Moreover, the generalised hyperscaling was used for calculating z from β/ν and γ/ν matching the predictions from the long-range Gaussian field theory [32].
In order to create a link to classical Q-FSS [36], the FSS of the squared magnetisation and order-parameter susceptibility were also studied for the four-dimensional TFIM in Ch. 8 contrasting the results found in this thesis with the results for the classical five-dimensional Ising model. The difference was argued to lie in the geometry of the systems with geometry $L^4 \times \infty$ for the classical analogue of the quantum system and L^5 for the classical system respectively.

11 Outlook

The SSE algorithm we used can handle arbitrary Ising interactions while avoiding the sign problem and, in principle, can be used to study frustrated or disordered systems. For disordered systems the translational invariance is in general not conserved and we would need to slightly modify the algorithm; Walker's method, used for drawing bonds according to their matrix weight, would need to consider all sites with their respective bonds individually instead of considering the bonds of one site representatively. For frustrated systems the algorithm probably suffers from large autocorrelation times similar to the antiferromagnetic LRTFIM and one might need to modify the algorithm in order to adequately study the system of choice. In the case of the antiferromagnetic LRTFIM, we experienced an immense increase in autocorrelation time for long-range interactions with small decay exponents leading to stronger geometric frustration. The clusters in the off-diagonal update percolated as the algorithm we used did not match the underlying physics of the phase transition. This also poses a problem for other frustrated versions of the TFIM, e. g. the antiferromagnetic TFIM on the triangular [59] or pyrochlore lattice [124]. Tailored for the TFIM on the triangular lattice, Biswas et al. [76] developed a new SSE algorithm with reduced autocorrelation time. Instead of decomposing the Hamiltonian into single-bond operators, they used the triangular structure of the lattice and decomposed the lattice into triangular plaquettes made of three single-bond operators.[1] They later extended their algorithm to other frustrated lattices while stressing the properties important for reducing the autocorrelation time [125]. In the course of this thesis, we tried to apply this key idea to combine frustrated bonds into plaquettes to the antiferromagnetic LRTFIM and constructed an algorithm that is based on a combination of plaquettes and single-bond operators. However, the algorithm was not capable of capturing the correlations of the critical phase and the clusters still percolated for small σ. A tailored algorithm for the antiferromagnetic LRTFIM could further probe the claim that the criticality remains of short-range Ising type by simulating larger systems and also smaller decay exponents.

One could furter use the SSE formalism to study ferromagnetic or antiferromagnetic spin systems with continuous symmetries such as the N-vector model for $N > 1$

[1] The insertion of plaquette operators in the diagonal update is completely analogous to single-bond operators but the branching in the off-diagonal update is more complex and introduces the notion of "privileged" sites which are crucial for the speed-up [76, 125]. For details see Ref. [76].

with symmetry $O(N)$, e. g. the XY model ($N = 2$) or Heisenberg model ($N = 3$) [118, 123, 126]. However, for antiferromagnetic models on non-bipartite lattices, additional couplings in transverse directions would impose the sign problem, making the simulation of large systems and low temperature intractable.

In terms of Q-FSS, we argued that the fundamental difference of the Q-FSS study of classical systems and the Q-FSS study performed in this thesis lies in the infinite extent of the imaginary-time dimension. In order to further substantiate this link, one could perform simulations for the 4d TFIM at finite temperatures which are low enough to be within the scaling window but high enough for observables to perceptibly differ from their ground-state expectation value. This should effectively result in a quantum-classical mapping to a classical system that is noticeably finite in all dimensions and its FSS should concur with the classical Q-FSS. However, finding a temperature range where this scaling might be valid will likely be a subtle issue.

For the classical Q-FSS, Kenna et al. also addressed the multiplicative logarithmic corrections to scaling at $d = d_{\mathrm{uc}}$ and introduced a logarithmic counterpart $\hat{\wp}$ to the exponent $\wp$ governing the scaling of the characteristic length scale [37]

$$\xi_L(r = 0) \sim L \ln(L)^{\hat{\wp}} \tag{11.1}$$

at $d = d_{\mathrm{uc}}$, where $\wp = 1$. We did not account for this logarithmic correction in the same way as we neglected other multiplicative logarithmic corrections to mean-field scaling at the upper critical dimension as this special case was not the focus of this thesis but merely one point at the boundary from the intermediate to mean-field regime in the plots of critical exponents. When analysing this special case one should also consider $\hat{\wp}$ in addition to the other well-known logarithmic corrections to scaling.

In contrast to the static properties of the LRTFIM, its dynamic properties are less studied even though those are particularly interesting as they provide information on relaxation rates or cross-sections for inelastic neutron scattering. In Sec. 6.3 we already mentioned the possibility to study the dynamical correlations from the imaginary-time correlations. The latter can be obtained from mapping the SSE propagation direction to continuous imaginary time [120]. Translating these imaginary-time correlations to real-time dynamics is an ill-conditioned problem as anything short of an exact result in imaginary-time, including numerical data with finite precision, usually leads to unreliable results in real-time. There exist several methods stabilising the continuation of noisy data such as the Maximum Entropy method, stochastic analytic continuation or Padé methods [127]. However, those methods either tend to wash out the high-energy features or even yield unphysical results [127]. Lately, promising progress has been made in terms of analytical continuation by explicitly respecting the analytic Nevanlinna structure of the Green's functions [127].

Bibliography

[1] C. Monroe, W. C. Campbell, L.-M. Duan, Z.-X. Gong, A. V. Gorshkov, P. W. Hess, R. Islam, K. Kim, N. M. Linke, G. Pagano, P. Richerme, C. Senko, and N. Y. Yao, "Programmable quantum simulations of spin systems with trapped ions," *Rev. Mod. Phys.*, vol. 93, p. 025001, Apr 2021.

[2] M. Saffman, T. G. Walker, and K. Mølmer, "Quantum information with Rydberg atoms," *Rev. Mod. Phys.*, vol. 82, pp. 2313–2363, Aug 2010.

[3] W. Lenz, "Beitrag zum Verständnis der magnetischen Erscheinungen in festen Körpern," *Z. Phys.*, vol. 21, pp. 613–615, 1920.

[4] E. Ising, "Beitrag zur Theorie des Ferromagnetismus," *Z. Physik*, vol. 31, pp. 253–258, Feb 1925.

[5] R. Blinc, "On the isotopic effects in the ferroelectric behaviour of crystals with short hydrogen bonds," *Journal of Physics and Chemistry of Solids*, vol. 13, no. 3, pp. 204–211, 1960.

[6] P. de Gennes, "Collective motions of hydrogen bonds," *Solid State Communications*, vol. 1, no. 6, pp. 132–137, 1963.

[7] P. Pfeuty, "The one-dimensional Ising model with a transverse field," *Annals of Physics*, vol. 57, no. 1, pp. 79–90, 1970.

[8] S. Katsura, "Statistical Mechanics of the Anisotropic Linear Heisenberg Model," *Phys. Rev.*, vol. 127, pp. 1508–1518, Sep 1962.

[9] R. Moessner, S. L. Sondhi, and P. Chandra, "Two-Dimensional Periodic Frustrated Ising Models in a Transverse Field," *Phys. Rev. Lett.*, vol. 84, pp. 4457–4460, May 2000.

[10] R. Moessner and S. L. Sondhi, "Ising models of quantum frustration," *Phys. Rev. B*, vol. 63, p. 224401, May 2001.

[11] M. Powalski, K. Coester, R. Moessner, and K. P. Schmidt, "Disorder by disorder and flat bands in the kagome transverse field Ising model," *Phys. Rev. B*, vol. 87, p. 054404, Feb 2013.

[12] S. Humeniuk, "Quantum Monte Carlo study of long-range transverse-field Ising models on the triangular lattice," *Phys. Rev. B*, vol. 93, p. 104412, Mar 2016.

[13] D. S. Fisher, "Random transverse field Ising spin chains," *Phys. Rev. Lett.*, vol. 69, pp. 534–537, Jul 1992.

[14] D. S. Fisher, "Critical behavior of random transverse-field Ising spin chains," *Phys. Rev. B*, vol. 51, pp. 6411–6461, Mar 1995.

[15] S. Sachdev and A. P. Young, "Low Temperature Relaxational Dynamics of the Ising Chain in a Transverse Field," *Phys. Rev. Lett.*, vol. 78, pp. 2220–2223, Mar 1997.

[16] M. Heyl, A. Polkovnikov, and S. Kehrein, "Dynamical Quantum Phase Transitions in the Transverse-Field Ising Model," *Phys. Rev. Lett.*, vol. 110, p. 135704, Mar 2013.

[17] M. Heyl, "Dynamical quantum phase transitions: a review," *Reports on Progress in Physics*, vol. 81, p. 054001, Apr 2018.

[18] M. Heyl, F. Pollmann, and B. Dóra, "Detecting Equilibrium and Dynamical Quantum Phase Transitions in Ising Chains via Out-of-Time-Ordered Correlators," *Phys. Rev. Lett.*, vol. 121, p. 016801, Jul 2018.

[19] P. B. Chakraborty, P. Henelius, H. Kjønsberg, A. W. Sandvik, and S. M. Girvin, "Theory of the magnetic phase diagram of $LiHoF_4$," *Phys. Rev. B*, vol. 70, p. 144411, Oct 2004.

[20] D. Bitko, T. F. Rosenbaum, and G. Aeppli, "Quantum Critical Behavior for a Model Magnet," *Phys. Rev. Lett.*, vol. 77, pp. 940–943, Jul 1996.

[21] T. Lahaye, C. Menotti, L. Santos, M. Lewenstein, and T. Pfau, "The physics of dipolar bosonic quantum gases," *Reports on Progress in Physics*, vol. 72, p. 126401, nov 2009.

[22] S. Mahmoudian, L. Rademaker, A. Ralko, S. Fratini, and V. Dobrosavljević, "Glassy Dynamics in Geometrically Frustrated Coulomb Liquids without Disorder," *Phys. Rev. Lett.*, vol. 115, p. 025701, Jul 2015.

[23] S. T. Bramwell and M. J. Gingras, "Spin ice state in frustrated magnetic pyrochlore materials," *Science*, vol. 294, pp. 1495–1501, Nov 2001.

[24] C. Castelnovo, R. Moessner, and S. L. Sondhi, "Magnetic monopoles in spin ice," *Nature*, vol. 451, pp. 42–45, Jan 2008.

[25] J. W. Britton, B. C. Sawyer, A. C. Keith, C. C. Wang, J. K. Freericks, H. Uys, M. J. Biercuk, and J. J. Bollinger, "Engineered two-dimensional Ising interactions in a trapped-ion quantum simulator with hundreds of spins," *Nature*, vol. 484, pp. 489–492, Apr 2012.

[26] J. G. Bohnet, B. C. Sawyer, J. W. Britton, M. L. Wall, A. M. Rey, M. Foss-Feig, and J. J. Bollinger, "Quantum spin dynamics and entanglement generation with hundreds of trapped ions," *Science*, vol. 352, no. 6291, pp. 1297–1301, 2016.

[27] R. Islam, C. Senko, W. C. Campbell, S. Korenblit, J. Smith, A. Lee, E. E. Edwards, C.-C. J. Wang, J. K. Freericks, and C. Monroe, "Emergence and Frustration of Magnetism with Variable-Range Interactions in a Quantum Simulator," *Science*, vol. 340, no. 6132, pp. 583–587, 2013.

[28] F. Yang, S.-J. Jiang, and F. Zhou, "Achieving continuously tunable critical exponents for long-range spin systems simulated with trapped ions," *Phys. Rev. A*, vol. 99, p. 012119, Jan 2019.

[29] P. Jurcevic, B. P. Lanyon, P. Hauke, C. Hempel, P. Zoller, R. Blatt, and C. F. Roos, "Quasiparticle engineering and entanglement propagation in a quantum many-body system," *Nature*, vol. 511, pp. 202–205, Jul 2014.

[30] P. Richerme, Z.-X. Gong, A. Lee, C. Senko, J. Smith, M. Foss-Feig, S. Michalakis, A. V. Gorshkov, and C. Monroe, "Non-local propagation of correlations in quantum systems with long-range interactions," *Nature*, vol. 511, pp. 198–201, Jul 2014.

[31] L. Vanderstraeten, M. Van Damme, H. P. Büchler, and F. Verstraete, "Quasiparticles in Quantum Spin Chains with Long-Range Interactions," *Phys. Rev. Lett.*, vol. 121, p. 090603, Aug 2018.

[32] A. Dutta and J. K. Bhattacharjee, "Phase transitions in the quantum Ising and rotor models with a long-range interaction," *Phys. Rev. B*, vol. 64, p. 184106, Oct 2001.

[33] M. F. Maghrebi, Z.-X. Gong, M. Foss-Feig, and A. V. Gorshkov, "Causality and quantum criticality in long-range lattice models," *Phys. Rev. B*, vol. 93, p. 125128, Mar 2016.

[34] K. Binder, M. Nauenberg, V. Privman, and A. P. Young, "Finite-size tests of hyperscaling," *Phys. Rev. B*, vol. 31, pp. 1498–1502, Feb 1985.

[35] K. Binder, "Finite size effects on phase transitions," *Ferroelectrics*, vol. 73, no. 1, pp. 43–67, 1987.

[36] B. Berche, R. Kenna, and J.-C. Walter, "Hyperscaling above the upper critical dimension," *Nuclear Physics B*, vol. 865, no. 1, pp. 115–132, 2012.

[37] R. Kenna and B. Berche, "A new critical exponent ϙ and its logarithmic counterpart $\hat{ϙ}$," *Condensed Matter Physics*, vol. 16, no. 2, 2013.

[38] E. Flores-Sola, B. Berche, R. Kenna, and M. Weigel, "Role of Fourier Modes in Finite-Size Scaling above the Upper Critical Dimension," *Phys. Rev. Lett.*, vol. 116, p. 115701, Mar 2016.

[39] D. Vodola, L. Lepori, E. Ercolessi, and G. Pupillo, "Long-range Ising and Kitaev models: phases, correlations and edge modes," *New Journal of Physics*, vol. 18, p. 015001, dec 2015.

[40] T. Koffel, M. Lewenstein, and L. Tagliacozzo, "Entanglement Entropy for the Long-Range Ising Chain in a Transverse Field," *Phys. Rev. Lett.*, vol. 109, p. 267203, Dec 2012.

[41] G. Sun, "Fidelity susceptibility study of quantum long-range antiferromagnetic Ising chain," *Phys. Rev. A*, vol. 96, p. 043621, Oct 2017.

[42] S. Fey and K. P. Schmidt, "Critical behavior of quantum magnets with long-range interactions in the thermodynamic limit," *Phys. Rev. B*, vol. 94, p. 075156, Aug 2016.

[43] S. Fey, S. C. Kapfer, and K. P. Schmidt, "Quantum Criticality of Two-Dimensional Quantum Magnets with Long-Range Interactions," *Phys. Rev. Lett.*, vol. 122, p. 017203, Jan 2019.

[44] J. A. Koziol, "Quantum criticality of the long-range transverse-field Ising model on the square lattice - A quantum Monte Carlo study," 2021.

[45] S. Sachdev, *Quantum Phase Transitions*. Cambridge University Press, 2 ed., 2011.

[46] A. W. Sandvik, "Computational Studies of Quantum Spin Systems," *AIP Conf. Proc.*, vol. 1297, 2010.

[47] M. Vojta, "Quantum phase transitions," *Reports on Progress in Physics*, vol. 66, p. 2069–2110, Nov 2003.

[48] T. R. Kirkpatrick and D. Belitz, "Exponent relations at quantum phase transitions with applications to metallic quantum ferromagnets," *Phys. Rev. B*, vol. 91, p. 214407, Jun 2015.

[49] M. E. Fisher, "Renormalization group theory: Its basis and formulation in statistical physics," *Rev. Mod. Phys.*, vol. 70, pp. 653–681, Apr 1998.

[50] K. G. Wilson, "Renormalization Group and Critical Phenomena. I. Renormalization Group and the Kadanoff Scaling Picture," *Phys. Rev. B*, vol. 4, pp. 3174–3183, Nov 1971.

[51] K. G. Wilson, "Renormalization Group and Critical Phenomena. II. Phase-Space Cell Analysis of Critical Behavior," *Phys. Rev. B*, vol. 4, pp. 3184–3205, Nov 1971.

[52] B. Widom, "Surface Tension and Molecular Correlations near the Critical Point," *J. Chem. Phys.*, vol. 43, pp. 3892–3897, Dec 1965.

[53] E. J. Flores-Sola, *Finite-size scaling above the upper critical dimension.* Theses, Université de Lorraine ; Coventry University, Sep 2016.

[54] J. W. Essam and M. E. Fisher, "Padé Approximant Studies of the Lattice Gas and Ising Ferromagnet below the Critical Point," *J. Chem. Phys.*, vol. 38, pp. 802–812, Feb 1963.

[55] M. E. Fisher, "Correlation Functions and the Critical Region of Simple Fluids," *Journal of Mathematical Physics*, vol. 5, pp. 944–962, 1964.

[56] R. J. Elliott, P. Pfeuty, and C. Wood, "Ising Model with a Transverse Field," *Phys. Rev. Lett.*, vol. 25, pp. 443–446, Aug 1970.

[57] M. Suzuki, "Relationship between d-Dimensional Quantal Spin Systems and (d+1)-Dimensional Ising Systems: Equivalence, Critical Exponents and Systematic Approximants of the Partition Function and Spin Correlations," *Progress of Theoretical Physics*, vol. 56, pp. 1454–1469, 11 1976.

[58] L. Onsager, "Crystal Statistics. I. A Two-Dimensional Model with an Order-Disorder Transition," *Phys. Rev.*, vol. 65, pp. 117–149, Feb 1944.

[59] S. Humeniuk, "Quantum Monte Carlo Studies of Strongly Correlated Systems for Quantum Simulators," 2018.

[60] S.-k. Ma, *Modern Theory of Critical Phenomena.* Routledge, 2001.

[61] E. Luijten, *Interaction range, universality and the upper critical dimension.* PhD thesis, Delft University of Technology, 1997.

[62] R. Shankar, "Renormalization-group approach to interacting fermions," *Reviews of Modern Physics*, vol. 66, p. 129–192, Jan 1994.

[63] N. Defenu, A. Trombettoni, and S. Ruffo, "Criticality and phase diagram of quantum long-range O(N) models," *Phys. Rev. B*, vol. 96, p. 104432, Sep 2017.

[64] K. G. Wilson and M. E. Fisher, "Critical Exponents in 3.99 Dimensions," *Phys. Rev. Lett.*, vol. 28, pp. 240–243, Jan 1972.

[65] J. Sak, "Recursion Relations and Fixed Points for Ferromagnets with Long-Range Interactions," *Phys. Rev. B*, vol. 8, pp. 281–285, Jul 1973.

[66] J. A. Koziol, A. Langheld, S. C. Kapfer, and K. P. Schmidt, "Quantum-critical properties of the long-range transverse-field Ising model from quantum Monte Carlo simulations," *Phys. Rev. B*, vol. 103, p. 245135, Jun 2021.

[67] P. Adelhardt, J. A. Koziol, A. Schellenberger, and K. P. Schmidt, "Quantum criticality and excitations of a long-range anisotropic XY chain in a transverse field," *Phys. Rev. B*, vol. 102, p. 174424, Nov 2020.

[68] Z. Zhu, G. Sun, W.-L. You, and D.-N. Shi, "Fidelity and criticality of a quantum Ising chain with long-range interactions," *Phys. Rev. A*, vol. 98, p. 023607, Aug 2018.

[69] I. B. Sperstad, E. B. Stiansen, and A. Sudbø, "Quantum criticality in spin chains with non-Ohmic dissipation," *Phys. Rev. B*, vol. 85, p. 214302, Jun 2012.

[70] M. M. Ritzau, "Excitation energies of the ordered long-range transverse field Ising chain," 2019.

[71] E. Luijten and H. Meßingfeld, "Criticality in One Dimension with Inverse Square-Law Potentials," *Phys. Rev. Lett.*, vol. 86, pp. 5305–5308, Jun 2001.

[72] S. Humeniuk, "Thermal Kosterlitz–Thouless transitions in the 1/r 2 long-range ferromagnetic quantum Ising chain revisited," *Journal of Statistical Mechanics: Theory and Experiment*, vol. 2020, p. 063105, jun 2020.

[73] E. Gonzalez-Lazo, M. Heyl, M. Dalmonte, and A. Angelone, "Finite-temperature critical behavior of long-range quantum Ising models," 2021.

[74] K. Binder and D. W. Heermann, *Monte Carlo Simulation in Statistical Physics*. Springer, 2019.

[75] K. Binder, "Critical Properties from Monte Carlo Coarse Graining and Renormalization," *Phys. Rev. Lett.*, vol. 47, pp. 693–696, Aug 1981.

[76] S. Biswas, G. Rakala, and K. Damle, "Quantum cluster algorithm for frustrated Ising models in a transverse field," *Phys. Rev. B*, vol. 93, p. 235103, Jun 2016.

[77] S. Caracciolo, A. Gambassi, M. Gubinelli, and A. Pelissetto, "Finite-size correlation length and violations of finite-size scaling," *Eur. Phys. J. B*, vol. 20, pp. 594–598, Mar 2001.

[78] D. Sadhukhan and J. Dziarmaga, "Is there a correlation length in a model with long-range interactions?," 2021.

[79] J. Brankov and N. Tonchev, "Finite-size scaling for systems with long-range interactions," *Physica A*, vol. 189, no. 3, pp. 583–610, 1992.

[80] K. Fukui and S. Todo, "Order-N cluster Monte Carlo method for spin systems with long-range interactions," *Journal of Computational Physics*, vol. 228, pp. 2629–2642, Dec 2009.

[81] M. Mazars, "Ewald methods for inverse power-law interactions in tridimensional and quasi-two-dimensional systems," *J. Phys. A: Math. Gen.*, vol. 43, p. 425002, sep 2010.

[82] M. E. Fisher and M. N. Barber, "Scaling Theory for Finite-Size Effects in the Critical Region," *Phys. Rev. Lett.*, vol. 28, pp. 1516–1519, Jun 1972.

[83] J. Cardy, *Finite-size scaling*. Elsevier, 2012.

[84] B. Widom, "Surface Tension and Molecular Correlations near the Critical Point," *J. Chem. Phys.*, vol. 43, pp. 3898–3905, Dec 1965.

[85] E. Brézin, "An investigation of finite size scaling," *J. Phys. France*, vol. 43, pp. 15–22, Jan 1982.

[86] J. Cardy, *Scaling and Renormalization in Statistical Physics*. Cambridge University Press, 1996.

[87] A. Hankey and H. E. Stanley, "Systematic Application of Generalized Homogeneous Functions to Static Scaling, Dynamic Scaling, and Universality," *Phys. Rev. B*, vol. 6, pp. 3515–3542, Nov 1972.

[88] M. E. Fisher, *Scaling, universality and renormalization group theory*. Springer, 1983.

[89] K. Binder, "Critical properties and finite-size effects of the five-dimensional Ising model," *Z. Physik B - Condensed Matter*, vol. 61, pp. 13–23, 1985.

[90] J. L. Jones and A. P. Young, "Finite-size scaling of the correlation length above the upper critical dimension in the five-dimensional Ising model," *Phys. Rev. B*, vol. 71, p. 174438, May 2005.

[91] E. J. Flores-Sola, B. Berche, R. Kenna, and M. Weigel, "Finite-size scaling above the upper critical dimension in Ising models with long-range interactions," *Eur. Phys. J. B*, vol. 88, p. 28, Jan 2015.

[92] M. Wittmann and A. P. Young, "Finite-size scaling above the upper critical dimension," *Phys. Rev. E*, vol. 90, p. 062137, Dec 2014.

[93] G. A. Baker and G. R. Golner, "Spin-Spin Correlations in an Ising Model for Which Scaling is Exact," *Phys. Rev. Lett.*, vol. 31, pp. 22–25, Jul 1973.

[94] J. F. Nagle and J. C. Bonner, "Numerical studies of the Ising chain with long-range ferromagnetic interactions," *J. Phys. C: Solid State Phys.*, vol. 3, no. 2, pp. 352–366.

[95] E. Luijten and H. W. J. Blöte, "Classical critical behavior of spin models with long-range interactions," *Phys. Rev. B*, vol. 56, pp. 8945–8958, Oct 1997.

[96] J. Gubernatis, N. Kawashima, and P. Werner, *Quantum Monte Carlo Methods: Algorithms for Lattice Models*. Cambridge University Press, 2016.

[97] S. C. Kapfer, "Computerphysik und numerische Methoden," summer term 2017.

[98] D. A. Levin and Y. Peres, *Markov Chains and Mixing Times*. American Mathematical Society, 2 ed., 2017.

[99] H. Suwa and S. Todo, "Markov Chain Monte Carlo Method without Detailed Balance," *Phys. Rev. Lett.*, vol. 105, p. 120603, Sep 2010.

[100] E. P. Bernard, W. Krauth, and D. B. Wilson, "Event-chain Monte Carlo algorithms for hard-sphere systems," *Phys. Rev. E*, vol. 80, p. 056704, Nov 2009.

[101] P. Diaconis, S. Holmes, and R. M. Neal, "Analysis of a nonreversible Markov chain sampler," *The Annals of Applied Probability*, vol. 10, no. 3, pp. 726 – 752, 2000.

[102] N. Metropolis, A. W. Rosenbluth, M. N. Rosenbluth, and A. H. Teller, "Equation of State Calculations by Fast Computing Machines," *J. Chem. Phys.*, vol. 21, p. 1087, 1953.

[103] W. K. Hastings, "Monte Carlo sampling methods using Markov chains and their applications," *Biometrika*, vol. 57, pp. 97–109, 04 1970.

[104] R. H. Swendsen and J.-S. Wang, "Nonuniversal critical dynamics in Monte Carlo simulations," *Phys. Rev. Lett.*, vol. 58, pp. 86–88, Jan 1987.

[105] U. Wolff, "Collective Monte Carlo Updating for Spin Systems," *Phys. Rev. Lett.*, vol. 62, pp. 361–364, Jan 1989.

[106] E. Luijten and H. W. J. Blöte, "Monte Carlo method for spin models with long-range interactions," *Int. J. Mod. Phys. C*, vol. 6, pp. 359–370, 1995.

[107] A. W. Sandvik, "Stochastic series expansion method for quantum Ising models with arbitrary interactions," *Phys. Rev. E*, vol. 68, p. 056701, Nov 2003.

[108] M. Suzuki, S. Miyashita, and A. Kuroda, "Monte Carlo Simulation of Quantum Spin Systems. I," *Progress of Theoretical Physics*, vol. 58, pp. 1377–1387, 11 1977.

[109] N. V. Prokof'ev, B. V. Svistunov, and I. S. Tupitsyn, "Exact, complete, and universal continuous-time worldline Monte Carlo approach to the statistics of discrete quantum systems," *Journal of Experimental and Theoretical Physics*, vol. 87, pp. 310–321, Aug 1998.

[110] A. W. Sandvik and J. Kurkijärvi, "Quantum Monte Carlo simulation method for spin systems," *Phys. Rev. B*, vol. 43, pp. 5950–5961, Mar 1991.

[111] A. W. Sandvik, "A generalization of Handscomb's quantum Monte Carlo scheme-application to the 1D Hubbard model," *J. Phys. A: Math. Gen.*, vol. 25, pp. 3667–3682, Jul 1992.

[112] D. C. Handscomb, "The Monte Carlo method in quantum statistical mechanics," *Mathematical Proceedings of the Cambridge Philosophical Society*, vol. 58, no. 4, pp. 594–598, 1962.

[113] F. F. Assaad, "Quantum Monte Carlo Methods on Lattices: The Determinantal Approach," *NIC Series*, vol. 10, pp. 99–156, Jan 2002.

[114] R. R. dos Santos, "Introduction to Quantum Monte Carlo Simulations for Fermionic Systems," *Braz. J. Phys.*, vol. 33, Mar 2003.

[115] M. Troyer and U.-J. Wiese, "Computational Complexity and Fundamental Limitations to Fermionic Quantum Monte Carlo Simulations," *Phys. Rev. Lett.*, vol. 94, p. 170201, May 2005.

[116] J. Koziol, S. Fey, S. C. Kapfer, and K. P. Schmidt, "Quantum criticality of the transverse-field Ising model with long-range interactions on triangular-lattice cylinders," *Phys. Rev. B*, vol. 100, p. 144411, Oct 2019.

[117] D. C. Handscomb, "A Monte Carlo method applied to the Heisenberg ferromagnet," *Mathematical Proceedings of the Cambridge Philosophical Society*, vol. 60, no. 1, pp. 115–122, 1964.

[118] A. W. Sandvik, R. R. P. Singh, and D. K. Campbell, "Quantum Monte Carlo in the interaction representation: Application to a spin-Peierls model," *Phys. Rev. B*, vol. 56, pp. 14510–14528, Dec 1997.

[119] O. F. Syljuåsen and A. W. Sandvik, "Quantum Monte Carlo with directed loops," *Phys. Rev. E*, vol. 66, p. 046701, Oct 2002.

[120] F. Michel and H.-G. Evertz, "Lattice dynamics of the Heisenberg chain coupled to finite frequency bond phonons," Mar 2007.

[121] P. Weinberg and M. Bukov, "QuSpin: a Python Package for Dynamics and Exact Diagonalisation of Quantum Many Body Systems part I: spin chains," *SciPost Phys.*, vol. 2, p. 003, 2017.

[122] P. Weinberg and M. Bukov, "QuSpin: a Python Package for Dynamics and Exact Diagonalisation of Quantum Many Body Systems. Part II: bosons, fermions and higher spins," *SciPost Phys.*, vol. 7, p. 20, 2019.

[123] A. W. Sandvik, "Classical percolation transition in the diluted two-dimensional $S = \frac{1}{2}$ Heisenberg antiferromagnet," *Phys. Rev. B*, vol. 66, p. 024418, Jul 2002.

[124] P. Emonts and S. Wessel, "Monte Carlo study of the discontinuous quantum phase transition in the transverse-field Ising model on the pyrochlore lattice," *Phys. Rev. B*, vol. 98, p. 174433, Nov 2018.

[125] S. Biswas and K. Damle, "Efficient quantum cluster algorithms for frustrated transverse field Ising antiferromagnets and Ising gauge theories," 2019.

[126] A. W. Sandvik, "Finite-size scaling of the ground-state parameters of the two-dimensional Heisenberg model," *Phys. Rev. B*, vol. 56, pp. 11678–11690, Nov 1997.

[127] J. Fei, C.-N. Yeh, and E. Gull, "Nevanlinna Analytical Continuation," *Phys. Rev. Lett.*, vol. 126, p. 056402, Feb 2021.

Acknowledgments

I am grateful for the constant support and thoughtful advice of my supervisor Prof. Dr. Kai Philipp Schmidt. Throughout this project Prof. Schmidt was always in reach for my questions. He encouraged me to pursue my goals and provided significant guidance for my long-term plans. As my second supervisor, Dr. Sebastian Kapfer provided excellent guidance, in particular with his great expertise in Monte Carlo methods. I am especially grateful to him for arousing my interest in computational physics during my Bachelor studies and his immense encouragement over the past years.

My fellow colleague Jan Alexander Koziol deserves special thanks for his unlimited and continuous support. With his broad and deep knowledge he served me as a guiding light since I started this project. I am deeply grateful for his significant support and everything he teached me. His valuable comments and constructive criticism pushed the quality of this thesis.

I additionally want to thank Kai Klede for proofreading parts of this thesis and all my colleagues of the institute theory 1 for numerous enjoyable and fruitful discussions as well as their kind assistance.

I further acknowledge the well-designed LaTeX-template provided by my fellow colleague Michael Winter which I only slightly adapted to match my own preferences.

Eigenständigkeitserklärung

Hiermit versichere ich, dass ich die vorliegende Masterarbeit selbstständig verfasst habe. Ich versichere, dass ich keine anderen als die angegebenen Quellen benutzt und alle wörtlich oder sinngemäß aus anderen Werken übernommenen Aussagen als solche kenntlich gemacht habe. Des Weiteren versichere ich, dass diese Arbeit weder vollständig noch in wesentlichen Teilen Gegenstand eines anderen Prüfungsverfahren gewesen ist.

Erlangen, den 30. September 2021

Anja Langheld